Experimental Studies of the Nanomechanical Properties of Nanotubes

by

Adam Michael Fennimore

B.S. (Brigham Young University) 1998
M.A. (University of California, Berkeley) 2002

A dissertation submitted in partial satisfaction of the
requirements for the degree of
Doctor of Philosophy

in

Physics

in the

GRADUATE DIVISION
of the
UNIVERSITY OF CALIFORNIA, BERKELEY

Committee in charge:
Professor Alex Zettl, Chair
Professor Steven G. Louie
Professor Arun Majumdar

Spring 2005

The dissertation of Adam Michael Fennimore is approved:

Chair Date

Date

Date

University of California, Berkeley

Spring 2005

The dissertation of Adam Michael Fennimore is approved:

Chair 4/27/05
Date

Steven G. Louie 4/25/05
Date

May 2, 2005
Date

University of California, Berkeley

Spring 2005

Experimental Studies of the Nanomechanical Properties of Nanotubes

Adam Michael Fennimore

Abstract

Experimental Studies of the Nanomechanical Properties of Nanotubes

by

Adam Michael Fennimore

Doctor of Philosophy in Physics

University of California, Berkeley

Professor Alex Zettl, Chair

The topic of this dissertation is the study of the nanomechanical properties of nanotubes. These multi-faceted mechanical materials are able to perform many tasks at the nanoscale for which traditional nanoelectromechanical (NEMS) materials are insufficient. Their high strength-to-weight ratio and layered structure make nanotubes ideal for a number of NEMS applications. One such NEMS application is to create a nanoscale motor exploiting the interlayer sliding of a multi-walled carbon nanotube (MWCNT). A key accomplishment discussed in this dissertation is the creation of such a nanoscale synthetic motor. As an introduction to the subject of nanomotors, a review of the wide variety of nanoscale and microscale motors that either occur naturally or have been synthetically created is presented.

The motivation, creation and operation of nanotube based nanomotors are given in this dissertation. Through the fabrication of these devices a number of novel techniques for the manipulation and selective placement of nanotubes have been developed. These techniques enable the placement of nanotubes on predetermined locations, in an aligned fashion and on a variety of devices.

Through the exploration of alternate device architectures and manipulation techniques, the ability to correlate the atomic structure of individual nanostructures with their mechanical, thermal, and electrical properties has been developed. Electron transparent Si_3N_4 membranes can now be routinely fabricated for *in situ* TEM transport experiments. Nanotubes placed on STM tips through the use of *in situ* SEM nanomanipulators can also be imaged via TEM prior to transport experiments.

We have successfully created and operated MWCNT nanomotors using electron beam lithography techniques. These motors were capable of 360° of movement and could be continually driven for thousands of cycles without any evidence of wear or fatigue. These MWCNT nanomotors demonstrate the great ability of MWCNT to act as NEMS scaffolds. With nanotubes established as promising NEMS enabling elements, the ongoing experiments of our research group on hybrid nanotube-NEMS devices are also discussed. The fabrication of electron transparent devices uniquely positions our research group to be able to fully correlate the structure and behavior of individual nanostructures and hybrid NEMS.

Professor Alex Zettl
Dissertation Committee Chair

To My Dad, who always fed my curiosity with sound answers

Contents

List of Figures **iv**

I Introduction to Nanomotors **1**

1 Nanomotors and NEMS **3**
1.1 Introduction . . . 3
1.2 Biomolecular Mechanical Systems . . . 4
1.2.1 Rotary Motors . . . 5
1.2.2 Linear Motors . . . 8
1.2.3 DNA . . . 11
1.3 Chemical Mechanical Systems . . . 12
1.3.1 Mechanical Elements in Chemistry . . . 12
1.3.2 Unidirectional Chemical Motors . . . 15
1.4 From MEMS to NEMS . . . 17

II Experimental Studies of Nanotube Based Nanomotors **23**

2 Introduction to Carbon Nanotubes **25**
2.1 Structure and Properties . . . 25
2.2 Nanotubes as Bearings . . . 27
2.3 Nanotube devices . . . 30

3 Nanomotor Construction **33**
3.1 Device Architectures . . . 33
3.1.1 Introduction . . . 33
3.1.2 Solid Substrate . . . 33
3.1.3 Electron Transparent - SOI . . . 37
3.1.4 Electron Transparent - Si_3N_4 . . . 38
3.2 Orientation and controlled placement of nanotubes . . . 44
3.2.1 Introduction . . . 44
3.2.2 Alignment via Fluid Flow . . . 45
3.2.3 Surface Functionalization . . . 47
3.2.4 Fluidic Trapping . . . 51
3.2.5 Electrophoresis . . . 55

3.2.6 Nanomanipulation . . . 59
3.3 MWNT bearing creation . . . 62
3.3.1 Introduction . . . 62
3.3.2 Mechanical Stress . . . 63
3.3.3 Reactive Ion Etching . . . 64
3.3.4 Electrically Driven Vaporization . . . 67
3.3.5 Electron Beam Cutting . . . 72

4 Nanomotor Operation **82**
4.1 Experimental Setup . . . 82
4.1.1 Sample Mounting and ESD . . . 82
4.1.2 SEM Observation . . . 84
4.2 Static Deflections . . . 87
4.3 Dynamic Deflections . . . 94
4.4 Discussion . . . 95

III Other Nanotube NEMS structures **99**

5 NEMS resonators **101**
5.1 Q in NEMS . . . 101
5.2 Nanotubes as NEMS resonators . . . 103
5.2.1 Singly Clamped Beams . . . 104
5.2.2 Doubly Clamped Beams . . . 105
5.2.3 Torsional Resonators . . . 107
5.3 Other NEMS devices . . . 113

Bibliography **118**

A List of Acronyms **130**

B Microfabrication Recipes **132**
B.1 Si_3N_4 membranes . . . 132
B.1.1 Substrates . . . 132
B.1.2 Oxide/Nitride Layers . . . 133
B.1.3 Membranes . . . 133
B.1.4 Contact Pads and Alignment Marks . . . 135
B.1.5 Devices . . . 137

List of Figures

1.1 Model of the ATP Synthase. The ATP synthase consists of two rotary motors, F_1 and F_0, connected by a drive shaft γ. (figure from [8]) 5

1.2 Simplified model of the flagellar motor found in bacteria. (figure from [10]) 8

1.3 Translation method of myosin. By hydrolyzing ATP the myosin motor head rotates to a forward position as shown in (i). The motor head is then free to loosely bind with the actin filament (ii). With the release of a P_i the motor head snaps back propelling the motor protein forward (iii). The remaining ADP is then released, allowing the motor head to release from the actin filament (iv). (figure from [8]) 10

1.4 DNA based molecular tweezers. The two ends of the molecular tweezers are indicated by an orange circle and triangle. A ss-DNA (F) which is both a complement to the blue ss-DNA section next to the orange circle and the gray ss-DNA section next to the orange triangle is introduced. As F hybridizes with both of the ss-DNA it brings the two ends of the tweezer together. Through addition of the complement $\overline{F}$, the ss-DNA F can be removed, thus opening the tweezers again. (figure from [23]) 13

1.5 Graphical depiction of a (a) rotaxane and (b) [2]catenane molecule. (figure from [25]) 14

1.6 Rotation paths for unidirectional motor molecules synthesized by (a) Kelly *et al* and (b) Koumura *et al*. (figures from [27, 28]). 15

1.7 Catenane based motor molecules constructed by Leigh *et al*. These include a (a)[2]catenane molecule capable of sequential motion around a larger ring, and a (b)[3]catenane molecule capable of unidirectional rotation. (figure from [29]) 16

1.8 A MEMS micromotor fabricated at UC Berkeley by Richard Mullers research group. (figure from [32]) 19

1.9 (a) Rotary motor developed at Sandia National Laboratory. Two orthogonally opposed linear comb drive shuttles drive the rotary motion of a gear through flexible linkages to a pin joint on the gear. (b) Through multiple gear reductions this motor is able to drive a linear rack and alter the position of an optical mirror. (figure from [58]). 21

2.1 Chiral vector ($\mathbf{C}_h$) of a carbon nanotube shown on a graphene sheet of carbon atoms. The unit vectors of the lattice ($\hat{\mathbf{a}}_1$ & $\hat{\mathbf{a}}2$) are also shown. The axis of the nanotube is parallel to the vector $\mathbf{B}$ with the unit cell traced out by the square $OBB'A$. (figure from [62]) 26
2.2 (a-e) Conceptual representation of *in situ* creation of a MWCNT linear bearing. (f) TEM micrograph of MWCNT with the inner core of nanotubes fully extracted. (g) Series of sequential video images captured during the extraction of a MWCNT inner core. In the final frame the contact to the manipulator probe is severed and the inner core immediately retracts back into the MWCNT due to the van der Walls interaction. (figures from [69]) . 29
2.3 Conceptual design of MWCNT nanomotor, as drawn by Michael Fuhrer. . . 32

3.1 Geometry of a MWCNT motor on a solid substrate. A MWCNT is suspended through two anchor electrodes (A1 & A2) and is contacted by a rotor plate (R). The position of the rotor plate is controlled through two opposing metal stators (S1 & S2) and the conducting substrate acting as a third stator (S3). 34
3.2 Fabrication method for MWCNT motor devices on a solid substrate. MWCNT (a) deposited on a SiO_2 substrate are mapped and (b) coated with electron beam resist then (c) patterned. (d) Anchors, stators and a rotor are patterned through Cr/Au liftoff. (e) The MWCNT and rotor are then suspended through a wet chemical etch. 35
3.3 MWCNT motor devices on a Si substrate (a) prior and (b) subsequent to the BOE etch. Scale bars are (a) 300 nm and (b) 1 μm. 36
3.4 Fabrication method for SOI based electron transparent MWCNT motors. (a) Through optical lithography a set of anchor pads and stators are patterned. (b) The substrate is then coated with photoresist and patterned in the areas to be removed through RIE. (c) RIE is then used to etch through the substrate and (d) the resist is removed. (e) A MWCNT is deposited between the anchor electrodes through fluidic and electrophoretic techniques. A second set of anchor electrodes and a rotor paddle are defined through optical lithography. (f) The substrate is then freed from the handle wafer through an HF etch. 39
3.5 Fabrication method of Si_3N_4 membrane. A (a) DSP Si$\langle 100 \rangle$ is (b) coated with a layer of SiO_2 and Si_3N_4. These layers are (c) selectively removed through an RIE to mask an (d) anisotropic wet etch. (e) Coarse contact pads and electrical leads are then patterned through optical lithography. . . 41
3.6 Two alternate methods of completing device fabrication on Si_3N_4 membranes for nanoscale materials (a-d) incompatible with HF and (a,e-h) with high resolution requirements. 43
3.7 (a) SEM and (b) TEM images of two early Si_3N_4 membrane MWCNT motor devices. Scale bars are (a) 10 μm and (b) 1 μm. 44
3.8 Aligned nanotubes deposited on a substrate through spin coating. The spacing between the alignment marks is 8 μm. 46
3.9 Deposition of aligned MWCNT in a functionalized area. The nanotubes were deposited in higher concentrations at the top and upper right corner as these were the first areas encountered by nanotubes flowing in solution. The alignment of spin coated nanotubes is also visible in this figure. The patterned square to the right of the letters "BL" is 10 μm wide. 48

3.10 Nanotubes deposited through "snagging" on functionalized lines. In the left image SWCNT have been deposited through fluid flow parallel to functionalized lines while on the right MWCNT flowed perpendicular to the functionalized lines 50

3.11 An array of MWCNT mechanical devices created using functionalization and alignment techniques. Each of the devices contains a single MWCNT contacted by two anchors and a paddle as shown in the image at the right. . . 51

3.12 SOI structure developed by Aileen Wang for fluidic deposition of MWCNT. The entire structure is shown in (a) with the inset showing the interlocking tooth structure of the center gaps. (b) Through surface tension enhanced deposition approximately 50% of the tooth gaps are spanned by individual tubes. 52

3.13 Deposition of BNNT through fluidic trapping on thermal conductivity devices. The gap between the two electrodes is ~ 2.5 μm. 54

3.14 MWCNT deposited on an SOI motor device via fluidic trapping and AC DEP. Scale bar is 1 μm. 54

3.15 Aligned overhanging MWCNT deposited via AC DEP on the edge of a razorblade. 59

3.16 TEM image of BNNT mounted on a W tip through SEM nanomanipulation setup. (a) Overall composite image of the entire tube. (b) Enlargement of left hand section of the BNNT. The Pt used to cement the BNNT to the W tip can be seen on the left. The walls are visible and taper in the middle of the tube, making this a less than ideal nanotube for thermal conductivity measurements. Horizontal scale bar is 50 nm, while vertical scale bars are 10 nm. 61

3.17 Conceptual visualization of a variety of ways in which the outer walls of a MWCNT contacted by two anchors and a rotor may be fractured to create a free rotational bearing. 63

3.18 SEM image of MWCNT motor prior and subsequent to RIE. After RIE the torsional spring constant was reduced. Upon rotation, the nanotube fractured resulting in the image shown at the right. 66

3.19 Current cascades in MWCNT at constant voltage. (a) A typical cascade is shown with step sizes of 10-20 μA. (b) In some devices the step size was quite regular as is shown here. The constant voltages applied during these two current cascades were 3.6 V and 4.2 V respectively. 69

3.20 Ti short connecting the stators and rotor of a MWCNT NEMS device. . . . 71

3.21 Telescopic failure of a MWCNT that has undergone EDV on both sides of the rotor paddle. The images are in sequential order, showing increasing extension: (a) No voltages applied. (b) Rotor pulled down towards substrate (voltage applied to back gate). (c) Rotor pulled towards lower stator. (d) Rotor pulled towards upper stator (though hard to see, the nanotube is still continuous). 73

3.22 Suspended MWCNT device (a) prior and (b) subsequent to exposure to a prolonged line scan by a low energy electron beam. The arrow indicates the area that was exposed to and cut by the electron beam. 74

3.23 Composite TEM micrographs of (a) a nanotube in its pristine state suspended on a TEM grid and (b) the same nanotube after cutting. (c) A close-up image of the same nanotube and (d) the cut segments of the nanotube are shown. The image in (d) has been rotated and aligned to vertically correspond with the same sections in (c). The scale bars are 20 nm. 76

3.24 Cutting times for multiple cuts on a single nanotube in different atmospheres. The partial pressure of water is shown on the horizontal axis, while the majority gas is shown above the data points. The total pressure was 7.5×10^{-5} Torr during the N_2, O_2 and H_2 trials. 77

3.25 Cutting times for multiple cuts on two nanotubes in different atmospheres at different beam currents. In both cases the majority gas was water vapor. The dashed lines are guides for the eye. 79

3.26 Cutting time vs. acceleration voltage. (a) Cutting times for multiple cuts on several nanotubes at different electron beam energies. The dashed lines are guides for the eye. (b) Normalized cutting data from three nanotubes at different electron beam energies. The inverse of the total ionization cross section for water molecules as a function of electron energy is also plotted, and follows the same trend. 81

4.1 SEM images of static deflection of a MWCNT motor device through application of large electrostatic fields to the anchor electrode. 88

4.2 Plot of the absolute electric field surrounding the rotor plate in a MWCNT motor at two angular orientations as calculated through FEA. 89

4.3 Plot of the angular deflection of the rotor plate in a MWCNT device vs. voltage applied to the back gate stator. The deflections (1, 2, 3,& 4) are chronological in order, though not sequential. As these deflections were repeated the nanotube weakened, until eventually the device reached a point where it required very little voltage for movement and appeared to be rotationally free (Deflection 4). 91

4.4 SEM images of a MWCNT motor device where the rotor plate is rotationally free and able to reach any position within 360°. Below each image is a cross sectional depiction of the rotor orientation. The nanotube (barely visible) runs vertically through each image. The scale bar is 300 nm. 93

4.5 Two subsequent SEM video images of the rotor paddle taken during continuous movement. Through applying appropriately phased AC voltages to the stator electrodes the rotor paddle could be driven between the two horizontal positions shown. The time required for switching between these positions was less than the time between frames (33 msec). This movement could be sustained for thousands of cycles without any noticeable signs of wear or fatigue. The scale bar is 300 nm and the MWCNT (not visible) runs vertically through the middle of each frame. 96

5.1 (a) As the volume of experimental resonators has decreased, so has the Q. (figure from [48]) (b) The degradation of the Q was correlated directly to an increase in the surface-to-volume ratio in Si wire resonators. (figure from [141])(c) The log(vol(mm^3)) and surface-to-volume ratios are given for a 1 μm long nanotube of various diameters. 102

5.2 SEM images of rotor paddle resonating at 250 kHz imaged at two line scan rates of (a)0.42 ms/line and (b)0.21 ms/line. Each line consists of 645 pixels. The Fourier transform of the paddle area is shown at the lower left hand corner of each image along with the average line scan of the Fourier transform at the lower right hand corner. 109
5.3 TEM images of a MWCNT that has been subjected to an HF etch (a) prior and (b) subsequent to a high current anneal. (a) After the HF etch a large amount of surface damage and defects are easily visible. (b) Once annealed the nanotube can be restored to it's original graphitic state with markedly less surface defects. 112
5.4 TEM image of surface contamination of Au and electron beam resist on an as fabricated MWCNT device. The scale bar is 100 nm. 112
5.5 A conceptual model of a MWCNT GHz oscillator. The inner core of the MWCNT can be extracted by applying an attractive potential between the center nanotube section (D) and either the opposing nanotube sections (S1 or S2) or the capacitive electrodes (G1 or G2). 115

Acknowledgments

It goes without saying that this dissertation would not have been possible without the guidance and resources provided by an excellent research advisor, Alex Zettl. Alex has been a patient mentor while constantly feeding me ideas of worthwhile projects to pursue and ensuring that I had all of the necessary equipment. I am grateful for the scientist that I have become through my association with Alex.

No graduate student's career is successful without constructive interactions from his peers. I feel fortunate to have participated in a research group where all were so willing to help and where I could forge strong friendships. I have been humbled and inspired by the intelligence of those that have surrounded me. I am especially grateful for those graduate students who preceded me with their indispensable guidance and assistance. Phil Collins was instrumental in my choosing to join the Zettl research group, and a great help in getting me oriented and started within the group. Michael Fuhrer willingly stepped into a mentoring role and was instrumental in getting me started in the microlab and on the MWCNT motor project. I consider Keith Bradley a great friend who is always extremely insightful. Aileen Wang was vital in the SOI experiments. Masahiro Ishigami was an excellent source of frank advice and good ideas, and he made sure that we had plenty of stress relieving excursions from baseball games to rafting, kayaking and ski trips. I am grateful for John Cumings who was always available to talk with and always willing to take time to teach you what he had learned. I really can't say enough about Tom Yuzvinsky. Tom provided the crucial manpower to complete the motor project. He is a wonderful colleague to work and collaborate with, and he really kept the projects we were working on efficient and constantly progressing. It is my hope that I will continue to be able to work with people of his caliber in intelligence, work ethic, and personality. Xiaosheng Huang's perseverance

in the face of adversity was inspiring. I very much enjoyed hunting for single crystals of nanotubes and superconductivity in C_{60} FETs with Willi Mickelson. While success in these projects was difficult to come by I was able to learn a great deal of chemistry and synthetic techniques through my association with Willi. Through Chih Wei Chang's dilligent efforts the correlation of thermal transport with atomic structure should be possible in the near future. Gavi Begtrup has proven himself to be a true glutton for punishment taking upon himself the Si_3N_4 membrane fabrication on top of his many other projects. I am very excited at the prospects for these devices with someone as talented as Gavi at the helm and am sad that I won't be around to take part in his inevitable successes. Kenny Jensen and Çağlar Girit have truly caught the vision and potential of John Cumings' early work and are achieving wonderful results with the Nanofactory TEM nanomanipulator. Their work has great potential to extract relevant and interesting properties of nanotubes that have not yet been explored.

I am also grateful for all the positive interactions that I have had with talented post-doctoral researchers in our research group. Shaul Aloni could always be counted on for enthusiastic advice and help. Wei Qiang Han had the amazing ability of being able to grow just about anything you asked for (if he hadn't done it already). Chris Regan's patient work on a comprehensive interface for transport measurements has been quite useful for a number of experiments and has saved me innumerable hours of work. Steve Konsek's years of experience in device fabrication and measurement made him the perfect candidate for handing the membrane project over to and was able to increase the reliability and yield of these devices. I am sorry I didn't get a chance to work more closely with Andras Kis who has stepped in to a much needed leadership role on a number of projects and is already obtaining promising results.

Andrew Miner, a member of the Majumdar research group, was instrumental in the Si_3N_4 membrane fabrication. Without his help in deciding which instruments to use and qualifying on each one, the process would have been much more arduous. Through contact with Andy it was possible to begin collaborating with Deyu Li and Nihar Shah on the thermal conductivity measurements which are just now beginning to bear fruit.

During my studies I have worked with a number of talented undergraduate students. Ben Weintraub helped with MWCNT motor construction in the early stages. Nancy Ru worked on CVD growth of nanotubes. Kevin Jones whose fascination reminded us why we study science and could always be depended on for candor, worked on the C_{60} FET experiments. Melinda Han came to our research group with a great deal of experience and was able to easily lend a hand on device fabrication. Andrei Afanasiev has been the dream undergraduate student. One who joins the group and stays on as a dedicated researcher who can be trusted with complex tasks. Andrei has provided crucial help on a number of projects including nanotube synthesis, HPLC sorting of endohedral fullerenes, dielectrophoretic deposition of nanotubes, and direct placement and manipulation of nanotubes within the SEM. I hope our group continues to have undergraduates who are able to contribute as much as Andrei has.

At Brigham Young University the mentoring of David Allred and Steve Turley in the physics department helped set me on the path to Berkeley. Through them I was given my first taste of what it meant to be an experimental physicist and realized that I wanted to do nothing else. I hope that some day I can be as good a mentor to others as they were to me.

Caroline Day, Donna Sakima and Anne Takizawa have always been extremely helpful whenever I needed assistance and I appreciate all the work they do to keep the Zettl

research group, Physics Department and Graduate program running smoothly.

I am also grateful for the constant encouragement and support I have received from my immediate and extended family. My wife Jennette and my two children, Maxwell and Olivia, have made life outside of the lab a pleasureful adventure and have helped me keep my research successes and frustrations in perspective.

Part I

Introduction to Nanomotors

Chapter 1

Nanomotors and NEMS

> "I want to offer... $1,000 to the first guy who makes an operating electric motor—a rotating electric motor which can be controlled from the outside and, not counting the lead-in wires, is only 1/64 inch cube."
>
> Richard Feynman

1.1 Introduction

Richard Feynman's talk, "There's plenty of room at the bottom[1]", in 1959 is often heralded as nanotechnology's "face that launched a thousand ships." In this talk he proposed taking mechanical systems, manufacturing, information storage, and computation mechanisms to the atomic limit. At the end of this talk he offered rewards for benchmark achievements in data storage and mechanical devices. The latter, a challenge to build a microscale motor, is quoted above. His hope was that through these challenges he would be able to spur the development of alternative fabrication methods to realize his vision of miniaturization. So he was a little disappointed when Bill McLellan was able to build a working miniature motor shortly after his challenge purely by hand[2].

It was not until the early 1980's that Feynman's vision of a new method of fabri-

cating mechanical devices on a miniature scale was realized with the use of techniques from the microelectronics industry to "micromachine" mechanical structures out of silicon[3, 4]. The devices made through these techniques came to be known as microelectromechanical systems (MEMS). What might be termed the true realization of Feynman's challenge was achieved in 1989 by researchers at UC Berkeley and MIT when both groups created microscale rotational motors using silicon micromachining techniques[5, 6, 7].

While the MEMS revolution truly innovated a new method of fabricating mechanical devices that could "fit on the head of a pin", they were still many orders of magnitude larger than the atomic limits envisioned by Feynman. Currently there are a number of promising approaches to creating mechanical devices at these substantially smaller scales. These have been made possible by new tools, knowledge, and materials in a variety of disciplines. As much of this dissertation will deal with mechanical systems at the fundamental limits it is useful to briefly discuss the various approaches that are being undertaken to reach this limit. The key accomplishments, advantages and disadvantages of each approach will be discussed.

1.2 Biomolecular Mechanical Systems

In trying to create nanoscale mechanical devices, biological systems provide an excellent example. Nanoscale motors have existed for millions of years in natural systems enabling everything from the structural alteration of individual molecules on the nanoscale to the macroscopic movement of muscles. While it has been apparent for quite some time that these motors exist, the understanding of their structure and mechanisms has greatly accelerated in the last decade. As these motors are better understood there is hope that they can either be employed directly in nanomechanical systems or that their mechanisms may be

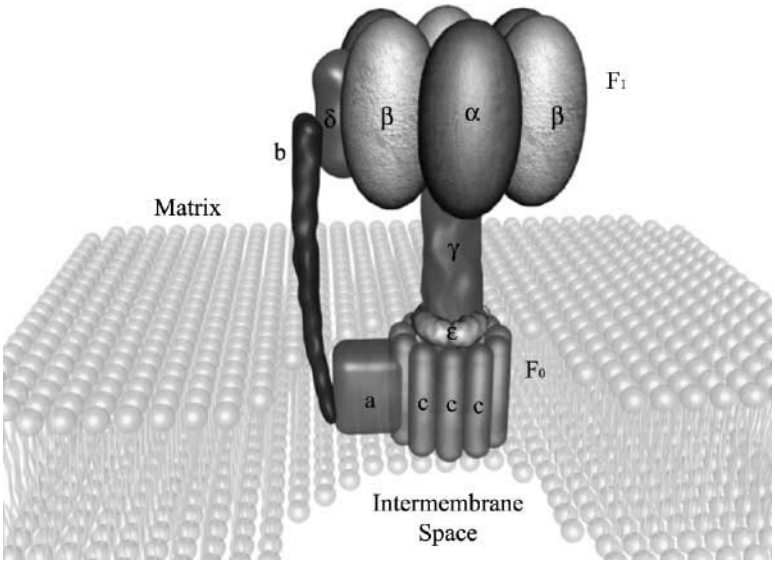

Figure 1.1: Model of the ATP Synthase. The ATP synthase consists of two rotary motors, F_1 and F_0, connected by a drive shaft γ. (figure from [8])

mimicked by biomimetic structures. Some excellent reviews of biological motors and their possible uses in nanotechnology were recently published[8, 9, 10], along with comprehensive texts detailing the entire field of molecular motors[11, 12]. The motors found in biological systems can be easily divided into two categories: rotary, and linear.

1.2.1 Rotary Motors

When you consider the complexity of a rotary motor, it is quite amazing that any of these motors actually exist at the molecular scale. A rotary motor requires a rotatable shaft and stators which can alternately attract a rotor element attached to the shaft. Energy must be effectively delivered to the motor to create the attractive forces needed. These attractive forces need to be appropriately phased so as to result in unidirectional rotation. The rotary motors found in nature have all of these qualities and are truly nanoscale motors.

ATP synthase

One of the most well understood and elegant of the biomolecular motors is the ATP synthase. The ATP synthase is an enzyme which catalyzes the synthesis of ATP in the walls of the mitochondria. It is often referred to as the energy currency of the cell because ATP is used to deliver energy to most cellular processes. By removal of a phosphate ion (P_i) ATP is converted to ADP and $\sim$ 0.6 eV of energy is released (depending upon the ambient conditions)[13]. Through the ATP synthase a P_i can be reattached to ADP to form ATP. This conversion process is enabled through the mechanical rotation of part of the ATP synthase.

It actually turns out that the ATP synthase consists of two rotary motors, both less than 10 nm in diameter. These two motors are known as the F_0-ATPase and F_1-ATPase motors and are depicted in Figure 1.1. They are linked by a common shaft $\sim$ 2 nm in diameter, known as the γ unit. These two motors perform separate tasks, the F_0 drives the rotation of the γ unit, while the F_1 uses this motion to convert ADP to ATP.

Typically the F_0 motor sits within the membrane wall of the mitochondria and its rotary motion is driven by proton flow through the membrane. This then drives the rotation of the γ unit, which acts as a drive shaft. As the γ unit rotates within the F_1 motor, ADP is converted into ATP through conformational changes in the F_1 motor head. Interestingly enough these motors can operate in reverse by supplying ATP to the F_1 motor, which will then rotate the γ unit within the F_0 motor, creating a proton gradient.

ATP synthase was first proposed to contain a rotary motor by Paul Boyer in 1982[14]. It was not until 1997 that the rotary motion of the F_1 motor was experimentally proven by Noji *et al*[15]. This was done by attaching a F_1 motor to a nickel surface. A fluorescently labelled actin filament of 1-4 μm in length was then attached to the γ unit. As

ATP was supplied to the F_1 motor the actin filament could be observed to rotate through fluorescence microscopy. The maximum rate of rotation of the actin filaments was observed to be 6-8 revolutions per second (rps). By calculating the viscous drag through the material, the torque supplied by the motor was calculated to be $\sim$ 40 pN-nm. Subsequent experiments with much smaller loads (40 nm gold beads) yielded rotation rates as high as 130 rps[16].

This understanding of the F_1 motor was exploited to create the first hybrid nanomechanical system[17]. In this experiment individual F_1 motors were mounted on Ni posts 80 nm in diameter. Ni propellers 750-1400 nm long were then attached to the γ unit. When immersed in a 2mM ATP solution the propellers were found to rotate at a rate of 0.74-8.3 rps. The calculated efficiency of energy conversion from ATP to rotational movement was $\sim$ 80%. While this may be viewed as a slight improvement on the original work by Noji *et al*, it was in fact a landmark achievement marrying biomolecular motors with traditionally fabricated inorganic materials.

The simplicity, efficiency and depth of understanding of the two motors contained in ATP synthase bode well for their use in future nanomechanical devices. This may be through either direct incorporation of the ATP motors or through molecules which mimic their function. Obstacles that will need to be surmounted to make their use more effective are the efficient delivery of ATP to the motors and a viable synthesis mechanism for ATP. The systems are of course inherently restricted to fluidic environments, unidirectional motion, imprecise position control, and speeds less than 120 rps. Because the fuel for movement is delivered in solution, these motors are not yet individually addressable.

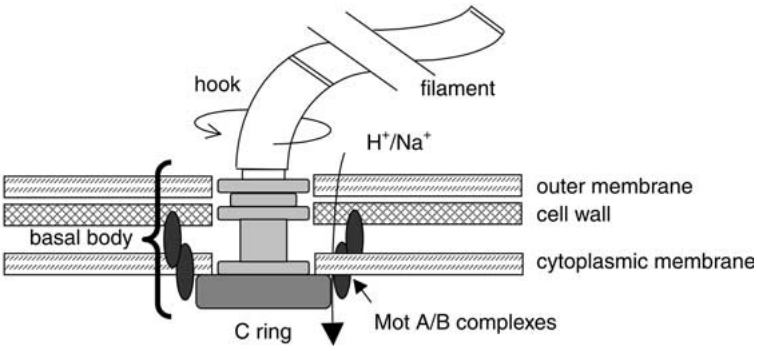

Figure 1.2: Simplified model of the flagellar motor found in bacteria. (figure from [10])

Flagella

Besides the ATP synthase, only one other rotary motor is known to exist in biological systems, the flagellar motor in bacteria. This motor drives the flagella in a rotary motion, thus making it possible for the bacteria to move about its local environment. The structure of these motors is much more complex that those of the ATP synthases and is still not fully resolved. The general structure of these motors is depicted in Figure 1.2. Like the F_0 motors, the rotation of the flagellar motors is driven by a proton (or in some cases, sodium) gradient across the membrane they are embedded in. However these motors can be driven at much higher speeds (> 1000 Hz), higher torques (> 4500 pN-nm), and in both directions. The complexity of the flagellar motors makes them less likely to be directly incorporated in devices or mimicked prior to the ATP synthase motors.

1.2.2 Linear Motors

While rotary motors are highly interesting, they are responsible for very little of the movement that we associate with biological systems. The majority of movement that we see taking place in biological systems is brought about by linear motor proteins. These motors do everything from transporting organelles within the cell, to moving cilia to drive

cell movement, to contracting muscles. All of these motors are similar in their method of movement in that they travel along track systems. These motors can be divided into three families based on their structure, preferred track system, and direction of movement. The three families are as follows:

Myosin

Myosin is the motor protein that is directly behind all muscle movement. Consequently its existence is obvious, and it has been studied the longest out of all the motor proteins. Myosin uses actin filaments as the tracks along which it moves. The actin filament is an asymmetric structure such that it has a polarity with positive and negative ends. Myosin's preferred direction of movement is from the negative to positive end. The myosin structure contains two motor heads attached to their cargo through a long filament. Although two motor heads are present, only one head is active at a time. Myosin moves up the actin filament through a ratcheting lever action activated by the hydrolysis of ATP. This ratcheting motion is shown in Figure 1.3. When acting in concert, large numbers of these motors are capable of fairly rapid movement, up to 60 μm/s in some cases[11]. The maximum force exerted by a typical myosin motor is on the order of 10 pN[9].

Kinesin

It was only recently that the motor protein kinesin was discovered (1985)[8]. Its primary function is to transport organelles within the cell. This is done by moving along a track system created by microtubules. Like actin filaments the microtubules also have a positive and negative end. The preferred direction of movement for kinesin is also toward the positive end. Like the myosin protein motor, kinesin also has two motor heads. But

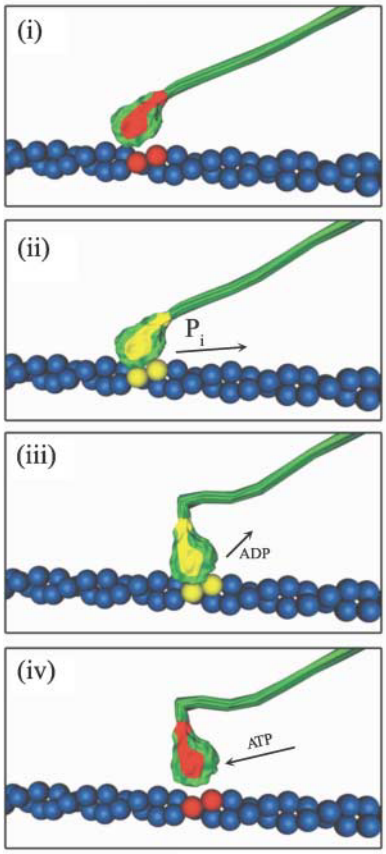

Figure 1.3: Translation method of myosin. By hydrolyzing ATP the myosin motor head rotates to a forward position as shown in (i). The motor head is then free to loosely bind with the actin filament (ii). With the release of a P_i the motor head snaps back propelling the motor protein forward (iii). The remaining ADP is then released, allowing the motor head to release from the actin filament (iv). (figure from [8])

rather than use a single motor head to successively ratchet up its track system, kinesin uses both heads in a successive walking motion up the microtubule. This movement is driven by the hydrolysis of ATP in a method similar to that of the myosin motor heads. As this motor walks up the microtubule it is capable of speeds on the order of 0.8-3 μm/s with forces of 6 pN[12].

Dynein

The chief purpose of the dynein motor is to drive the movement of cilia and flagella for cell motility. Like kinesin, this motor uses the microtubules as its track system, but it

moves in the opposite direction towards the negative end. The structure and method of movement of this motor is still not well understood, although considerable process is being made[10]. It is assumed that this motor's movement is similar to that of kinesin where multiple motor domains walk along the microtubule.

As of yet there have been no hybrid devices built similar to the ATP synthase device of Soong *et al* where an individual motor protein is used for movement. Hybrid devices however do exist, using the linear motor proteins on a large scale. In these devices large amounts of motors or tracks are attached to a substrate which is then able to transport their complement (which usually has been fluorescently tagged)[9, 10]. Recently great progress has been made in making more sophisticated devices. The microtubule tracks used by kinesin can be aligned through fluid flow in various setups[18, 19, 20]. With aligned tracks the movement along the surface is no longer randomized and small chips functionalized with kinesin motors will translate in a preferred direction along the tracks[21]. Similar unidirectional movement has also been accomplished by placing kinesin motors in a trench; translation of microtubules is then constricted along the trench. This translation is made unidirectional through the addition of arrowhead shaped openings which act as check valves, reversing the direction of microtubules flowing the non-preferred direction[22]. With the ability to control the direction of motor/microtubule movement many new devices are being developed.

1.2.3 DNA

DNA and RNA actually have their own set of unique motor proteins. These motors are responsible for splitting the double helix of DNA (helicase) and replicating DNA/RNA by stepping along a single strand and assembling its complement piece by piece

(polymerase). As these motors step along the stranded DNA they are capable of exerting forces of up to 35 pN, but move at speeds much slower than those of the other linear biological motors[9]. Because of their slower speeds and the tasks that they must perform as they move along the DNA (such as transcribing the strand), these motor proteins are not as ideal for use in future hybrid devices.

While the motor proteins of DNA are not easily used in hybrid mechanical devices, the DNA itself can be used to create mechanical devices. This is done primarily by exploiting the ability of single stranded DNA (ss-DNA) to recognize its complement and hybridize to form double stranded DNA (ds-DNA). Molecular tweezers consisting of DNA were successfully fabricated in 2000 using this technique[23]. The mechanism of actuation of these tweezers is illustrated in Figure 1.4. Using this same principle of hybridizing ss-DNA a DNA device capable of rotating 180° has been made [24]. While using DNA in this manner to create mechanical devices is complex, it is this complexity that gives it a certain advantage over other biologically based devices by making devices which are individually addressable. As this field continues to develop we are sure to see more complex mechanical structures made of DNA.

1.3 Chemical Mechanical Systems

1.3.1 Mechanical Elements in Chemistry

In much the same way that our knowledge and ability to control the structure of DNA was exploited to make mechanical devices, we can use our vast knowledge of synthetic chemistry to construct devices which are even closer to the fundamental atomic limits. These devices would have the distinct advantages of being able to operate in harsher environments

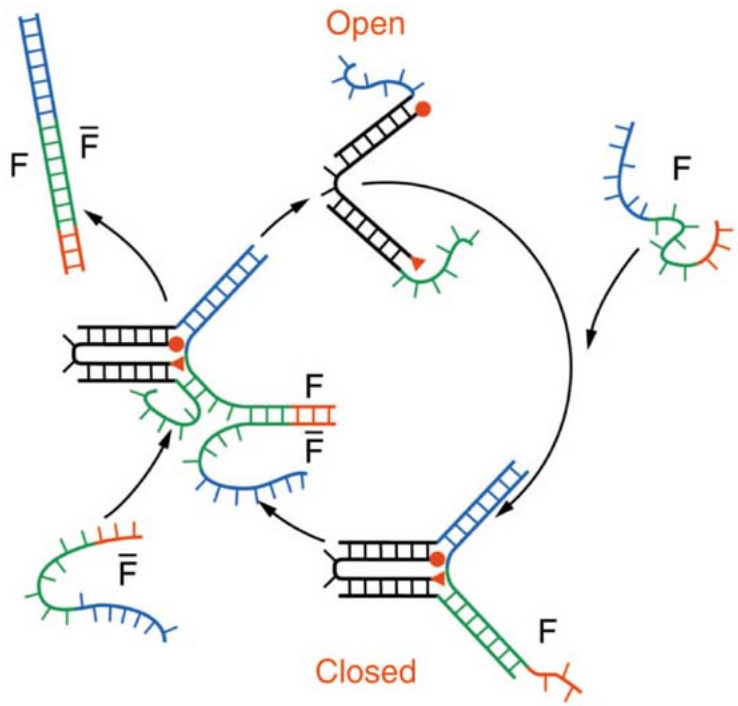

Figure 1.4: DNA based molecular tweezers. The two ends of the molecular tweezers are indicated by an orange circle and triangle. A ss-DNA (F) which is both a complement to the blue ss-DNA section next to the orange circle and the gray ss-DNA section next to the orange triangle is introduced. As F hybridizes with both of the ss-DNA it brings the two ends of the tweezer together. Through addition of the complement $\overline{F}$, the ss-DNA F can be removed, thus opening the tweezers again. (figure from [23])

(non-aqueous & larger temperature ranges), of having movement that can be driven by a variety of stimuli (chemical, electrical, and photo), and the ability to be easily functionalized and attached to a wide variety of other structures.

Chemical compounds have actually been known to behave as mechanical devices for quite some time. The earliest being in the late 1960's when chemical analogs of propellers and gears were discovered[25]. The key motion enabling element in these molecules is usually a bond or atom which acts as a hinge for the two sides of the molecule to rotate about. The motion in these systems can be driven by chemical, electrochemical, photochemical stimuli or even by Brownian motion. As is the case in all of the chemical motors, the motion of these molecules is visualized primarily through ^{1}H NMR.

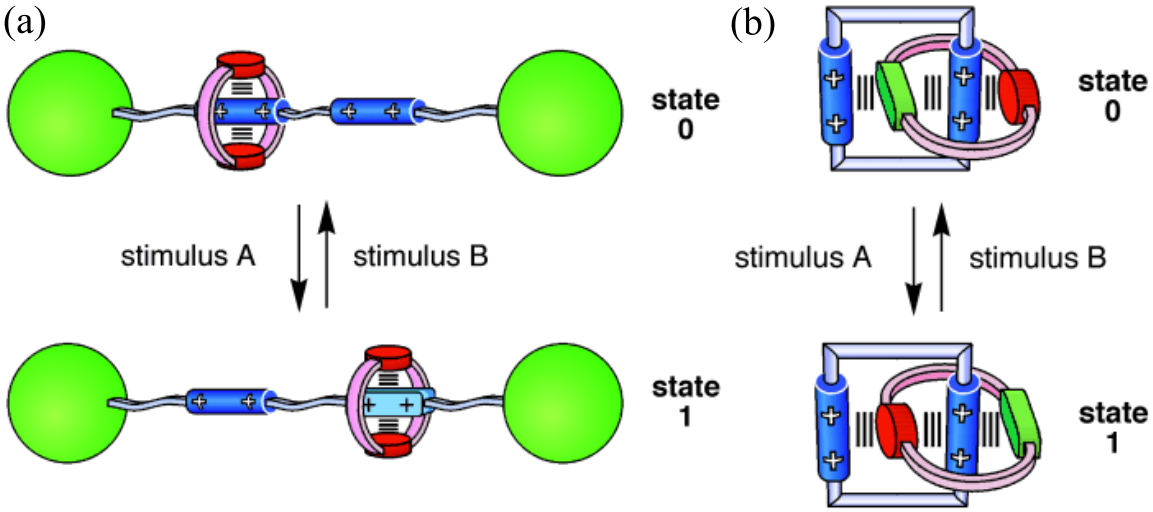

Figure 1.5: Graphical depiction of a (a) rotaxane and (b) [2]catenane molecule. (figure from [25])

Another approach to chemical mechanical systems is to use molecules which are mechanically attached rather than covalently bonded. These mechanical attachments then enable a variety of motions/mechanical devices to be formed. The most famous of these mechanically bonded systems are the rotaxanes and the catenanes. Rotaxanes consist of a molecular ring that is free to move on the shaft of a dumbbell shaped molecule while catenanes consist of interlocking molecular rings. These two types of molecules are shown in Figure 1.5. While the direct linkage of two rings can be pictured to act as a mechanical device in either a ball in socket joint or universal joint, the most commonly envisioned use of these molecules entails utilizing multiple binding sites. In the case of rotaxane two separate and stable binding sites for the ring are located on the shaft, while in catenanes a smaller ring encircles a larger ring with multiple binding sites. Then using temperature, light, or chemical stimulus the ring can be driven from site to site thus driving mechanical motion[25, 26].

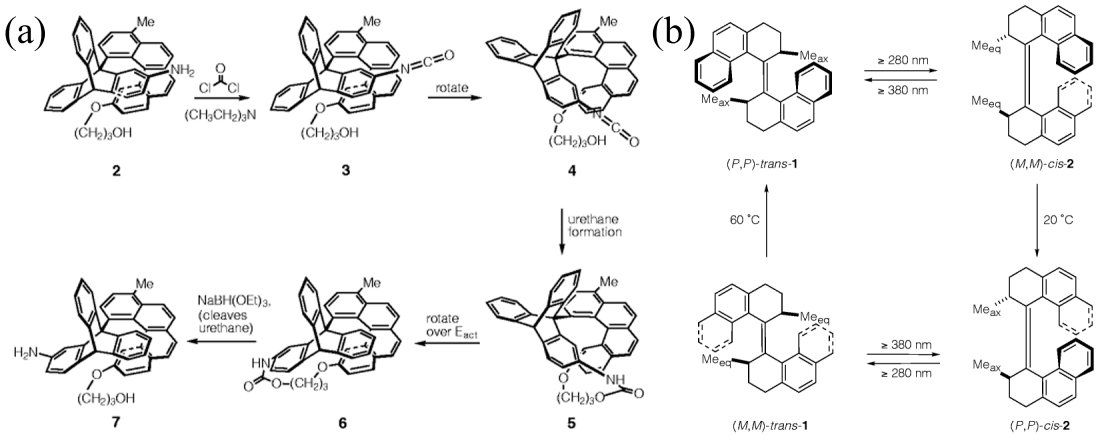

Figure 1.6: Rotation paths for unidirectional motor molecules synthesized by (a) Kelly *et al* and (b) Koumura *et al.* (figures from [27, 28]).

1.3.2 Unidirectional Chemical Motors

While all of these chemical systems have mechanical motion similar to motor systems, they were still far from being true motors due to the fact that the motion occurred in a randomized manner, rather than a unidirectional fashion. The key accomplishment in this field was the separate development of three molecular systems which are capable of unidirectional motion. The first two of these molecules were synthesized in 1999 by Kelly *et al*[27] and Koumura *et al*[28]. Both of these molecules contain two groups which are linked through a carbon-carbon bond about which the rotation occurs. The Kelly motor achieves its rotation through purely chemical steps and is limited to 120° of movement. The method of rotation is illustrated in Figure 1.6a. The Koumura motor can be continuously rotated 360° through a combination of photochemical and thermal steps. This motor molecule is depicted in Figure 1.6b.

The third set of unidirectional motor molecules were synthesized by Leigh *et al* in 2003[29]. Rather than use a single bond as the motion enabling element, these motors used a catenane architecture. The rotary motion was achieved by 1 or 2 secondary rings which could move between 3 or 4 different binding sites on a larger primary ring. Catenane

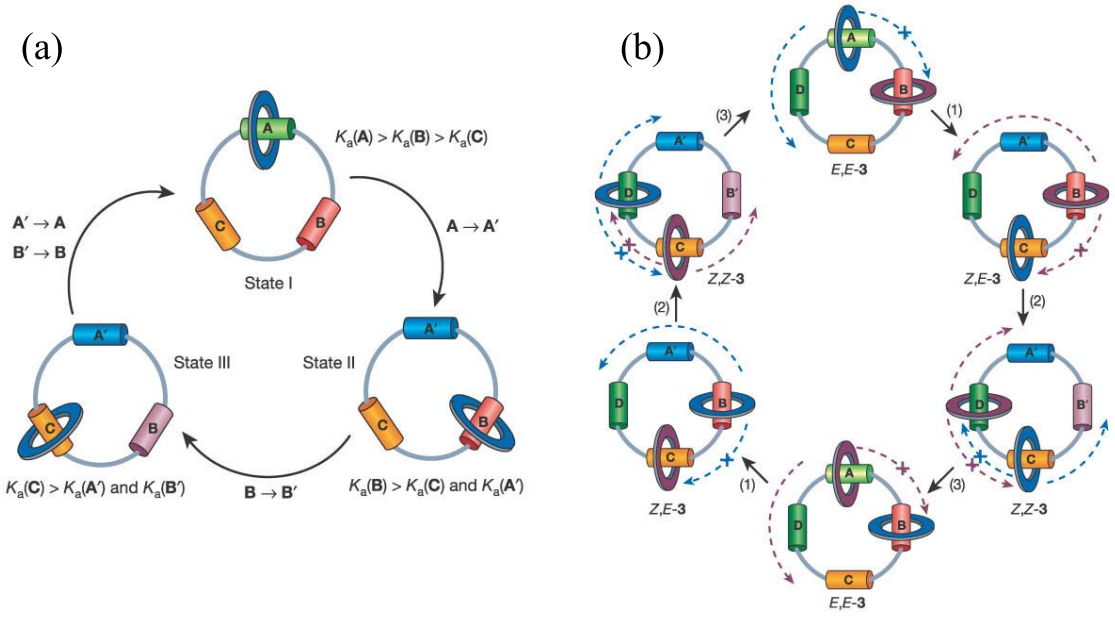

Figure 1.7: Catenane based motor molecules constructed by Leigh *et al.* These include a (a)[2]catenane molecule capable of sequential motion around a larger ring, and a (b)[3]catenane molecule capable of unidirectional rotation. (figure from [29])

molecules are named $[n]$catenane, where $[n]$ specifies how many total rings comprise a single linked molecule. For a [2]catenane molecule with 3 binding sites on the larger ring it was shown that the secondary ring could be sequentially driven around the primary ring through photochemical and thermal steps. Although this sequential motion was unidirectional, the path taken by the secondary ring was not necessarily unidirectional. In order to drive unidirectional motion, it was found that if a [3]catenane system with 4 binding sites along the primary ring was used, not only could the sequence of binding sites be controlled, but the direction that each ring went to subsequent binding sites could also be controlled due to the constriction of the extra ring along the primary ring. The motion of these two catenane systems is illustrated in Figure 1.7.

While the achievement of unidirectional motion in these three motor molecule systems is quite fantastic there are still many obstacles to the practical application of these

motors. The chief obstacles that these systems face are the time scales involved in a single rotation (typically several days) and coupling their motion to another system so that some form of work can be done. Research is currently focused on overcoming these two obstacles. Progress is being made on increasing the speed of the rotation cycle of the motor molecules, though there is still a long way to go until they are even within an order of magnitude of the capabilities of ATP synthase motors[30]. The first steps in coupling these motor molecules to other systems has been demonstrated by the same group that made the motor molecule shown in Figure 1.6b. This was done by doping a liquid crystal thin film with their light driven molecular motors[31]. If the motors were driven through their rotation, the movement coupled to the liquid crystal matrix inducing a visible color change. As more unidirectional molecular motors capable of faster rotations and coupling to other systems are developed, they will be better able to find niche applications.

1.4 From MEMS to NEMS

While it is quite amazing to begin to understand nature's nanomotors and to be able to develop our own through synthetic chemistry, the shortcomings in applying these systems to non-aqueous environments give us a great appreciation for the robust approach of MEMS. MEMS are currently used for many types of sensors (accelerometers, gyroscopes, pressure sensors, humidity sensors, and strain gauges), optical switches (DLP displays and communications), and microfluidic systems (inkjet printer heads and labs-on-a-chip)[32, 33, 34]. They have the distinct advantage that they can be mass produced reliably and can operate at much higher speeds with each device being individually addressable through applied voltages.

As the field of MEMS has matured it has become a mainstay of most engineering

departments, with courses and research programs dedicated to their design and construction. A wide variety of review articles[32, 33, 34, 35] and books[36, 37, 38, 39, 40] can be found outlining the construction techniques and applications of MEMS. Although an established field, it continues to make rapid progress through expansion and miniaturization. The tool set of MEMS is quite large and continually expanding, allowing it to address a host of new problems and applications. Currently research is being done on using MEMS for data storage, adjustable RF components, mechanical switches, mechanical combination locks, "smart dust," active feedback for turbulence on airfoils, and other exotic applications[34, 41, 42, 33]. The push towards further miniaturization of MEMS down to the nanoscale is driven by two motives. First, it is driven by a hope that in the same way that smaller size scales have allowed electronic devices to vastly improve their performance, nanoelectromechanical systems (NEMS) will have an advantage over their larger predecessors. Some key areas where the decreased size scale would give NEMS an advantage are for high frequency filters for communications and mass sensors[34]. Interest in NEMS is also driven by basic physics experiments which can be possible at this size scale. These experiments include measuring the casimir effect[43], phonon quantization[44], magnetic resonance force microscopy (MRFM)[45], and the quantum limit of oscillation of a macroscopic system ($\hbar\omega \gg kT$)[46].

The current state of the art in NEMS has been covered by a number of review articles[47, 48, 49] and a recent book by Andrew Cleland[50]. Most of the NEMS that have been made have involved traditional top-down approaches similar to those used for MEMS. Materials used to fabricate these devices have ranged from typical MEMS materials such as Si and SOI to more novel materials such as SiC and GaAs. Motion detection has been accomplished using traditional methods such as optical interference or reflected RF power and more exotic methods such as magnetomotive current detection and superconducting

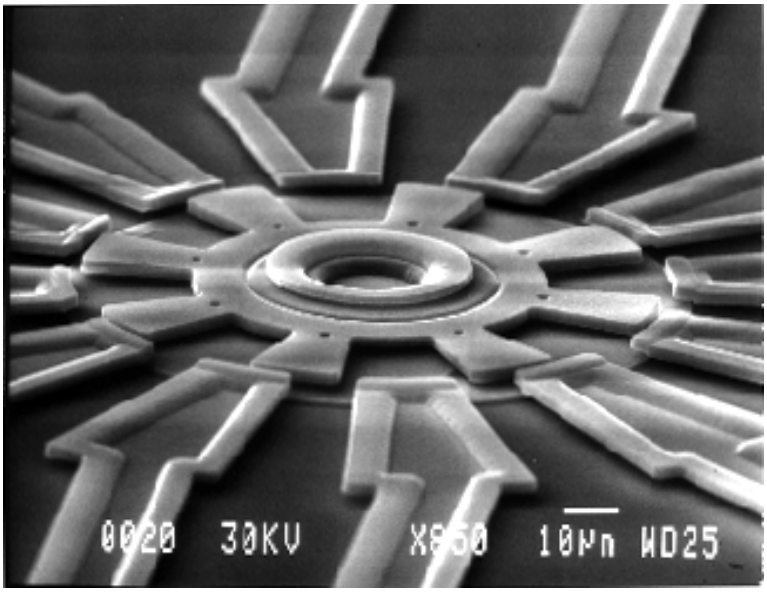

Figure 1.8: A MEMS micromotor fabricated at UC Berkeley by Richard Mullers research group. (figure from [32])

single electron transistors (SSET)[50].

An interesting feature of MEMS and NEMS is how they differ from mechanical systems we are used to seeing in everyday life. Mechanical systems on the macroscale consist of a large number of moving parts interconnected through various gears and linkages. The motion of each of these parts is typically made possible through a wide variety of linear and rotational bearings. In MEMS and NEMS the structures tend to be much simpler, with few interconnected parts, and a majority of the motion occurring through flexure or torsion. While rotational bearings and gears exist, there are few applications that take advantage of them, even though the first rotational MEMS motors were made in 1989.

A picture of the first MEMS micromotor developed by a group at UC Berkeley is shown in Figure 1.8. The center rotor is surrounded by twelve stators. By applying a large potential between a stator and the rotor, the rotor is attracted to a rotational position where it has maximum overlap with the stator. Through appropriately phasing the voltages applied to the stators the center rotor can be driven rotationally. A number of obstacles

made it difficult to incorporate these rotary motors into working devices. The required voltages were quite large and resulted in very little torque; these large fields also caused a large amount of dust to be attracted to the motor, hindering its operation. No easy method was present for transducing the force from the rotary motor, and the friction at the center hub was quite large and eventually caused the failure of the device. A number of groups attempted to tackle the friction problem through lubrication with either fluids[51], gas[52], or self-assembled monolayers (SAMs)[53]. Meanwhile, key research was done at Sandia to use the large linear forces generated by comb drive actuators to drive rotary motion, and to develop a better production method for interlocking gears[54, 55]. Through the use of comb drives and gear reduction, the torque values achievable with these systems were far greater than rotary motors with the original architecture. This motion could easily be coupled into other systems through a variety of transduction mechanisms. Maximum speeds of 300,000 rpm were obtained[55]. Wear along the bearing structure could also be studied with greater detail[56]. These motors are now used for optical switches and mechanical combination locks[57].

While it is clear that gears and rotary bearings in MEMS are now more viable, applications incorporating them are few compared to those that use flexure. Even for optical switching, for which a device using gears and rotors has been made, the more established devices for DLP displays and optical telecommunications use only flexures[34]. The reasons for this lack of applications are obvious, devices based on flexure are more simple to fabricate and have far fewer modes of failure. While MEMS incorporating bearings and gears have few applications today, it is hoped that as the techniques become more resilient, and the applications of simple flexures saturate, these methods will allow MEMS to continue to expand to create other applications.

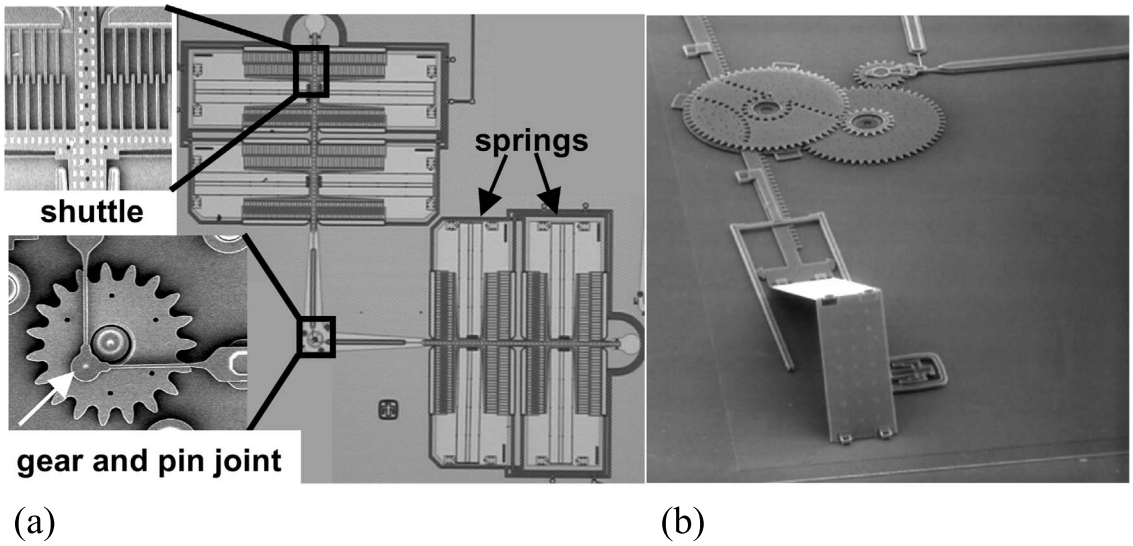

Figure 1.9: (a) Rotary motor developed at Sandia National Laboratory. Two orthogonally opposed linear comb drive shuttles drive the rotary motion of a gear through flexible linkages to a pin joint on the gear. (b) Through multiple gear reductions this motor is able to drive a linear rack and alter the position of an optical mirror. (figure from [58]).

Fabricating devices with nanoscale dimensions is already quite difficult, so it comes as no surprise that all of the NEMS mentioned previously were achieved purely using flexural and torsional beams. Fortunately enough, these simple devices have already been shown to have a great deal of promise. Yet it is clear that if more robust techniques can be developed for the manufacture of bearings, hinges, gears, etc., the ability of NEMS to meet future challenges will increase.

One approach hoping to expand the abilities of NEMS is to merge the bottom-up approaches that are so common for synthesis of nanostructured materials with the top-down approaches typical in NEMS. The first such device created by merging these approaches was realized in 2000 by Rueckes *et al*[59]. This device used the ability of carbon nanotubes to be mechanically pulled together through electrostatic attraction to form a metastable contact. These devices can act as individual memory bits and are currently being fabricated on large scales for this purpose. Nanotubes have a number of physical properties that present them

as an ideal material for use in hybrid NEMS. The physical properties of nanotubes and some of their possibilities in NEMS will be outlined in the next chapter.

Part II

Experimental Studies of Nanotube Based Nanomotors

Chapter 2

Introduction to Carbon Nanotubes

2.1 Structure and Properties

Carbon is a very versatile element with many known allotropes. Some of these allotropes, like diamond and graphite, are naturally occurring and have been known to exist for quite some time, many others have just recently been discovered. Carbon nanotubes, a form of carbon that has excited a great deal of interest, were discovered in 1991[60].

Carbon nanotubes consist of a graphene sheet of sp^2 bonded hexagonal carbon which has been rolled to form a cylinder with a diameter in the nanometer range. They come in two varieties, single walled carbon nanotubes (SWCNT) and multi-walled carbon nanotubes (MWCNT). SWCNT are defined by their rolling or chiral vector, a vector connecting two points on the graphene sheet which are brought together to form the circumference of the nanotube. This rolling vector is shown in Figure as $\mathbf{C}_h = n\hat{\mathbf{a}}_1 + m\hat{\mathbf{a}}_2$. SWCNT are often referred to by the components of their rolling vector (n, m). While most SWCNT are chiral, two achiral varieties exist, zigzag where n or $m = 0$ and armchair where $n = m$. The electronic properties of SWCNT are highly dependent upon chirality with

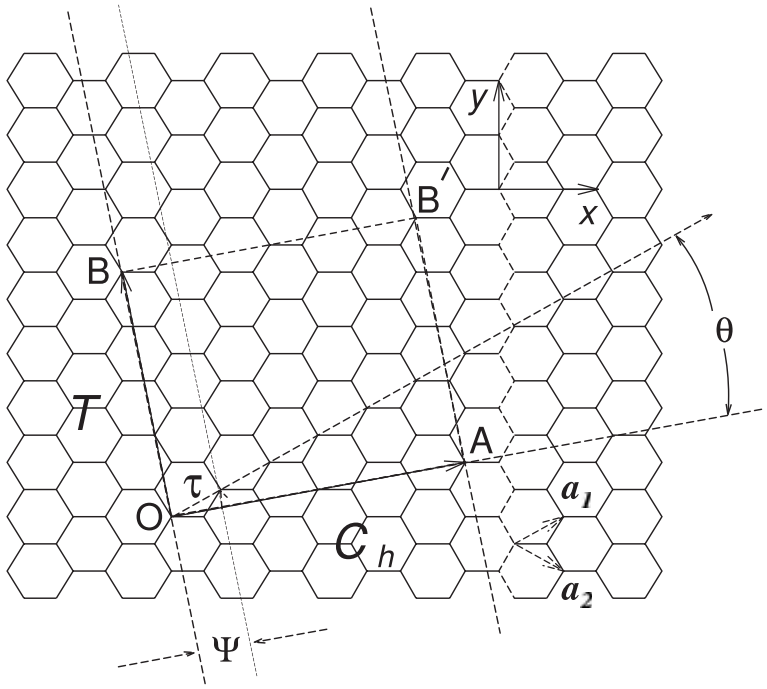

Figure 2.1: Chiral vector ($\mathbf{C}_h$) of a carbon nanotube shown on a graphene sheet of carbon atoms. The unit vectors of the lattice ($\hat{\mathbf{a}}_1$ & $\hat{\mathbf{a}}2$) are also shown. The axis of the nanotube is parallel to the vector $\mathbf{B}$ with the unit cell traced out by the square $OBB'A$. (figure from [62])

1/3 of all possible structures metallic and 2/3 semiconducting. The metallic nanotubes are capable of carrying very high current densities exceeding $10^9 A/cm^2$[61]. A MWCNT is made up of a series of concentrically nested cylinders. The spacing of these cylinders is 3.4Å, which is almost the same spacing found in graphite.

Although we typically think of graphite as being the weak cousin of diamond, the in-plane sp^2 bonds of graphite are stronger than the sp^3 bonds found in diamond. Because a nanotube is made up of sp^2 bonds, they are extremely strong, with Young's modulus of 1TPa or greater. This far exceeds that of steel and kevlar. The strength-to-weight ratio of carbon nanotubes is so high it has been considered for applications as exotic as a space elevator[63].

2.2 Nanotubes as Bearings

With a layer to layer spacing comparable to that of graphite, it was expected that the nested cylinders in MWCNT would be very weakly coupled to each other through van der Waals interactions. One can suppose that these weak interactions might allow the cylinders to slide or rotate within each other to act as linear or rotational bearings. The possibility of the nested cylinders in a MWCNT being able to do such movements was first proposed theoretically in 1993 by Charlier and Michenaud[64]. They investigated the optimal spacing for a double walled carbon nanotube and the energy barriers for linear and rotational movement of a section of a (5,5) nanotube relative to a section of a (10,10) nanotube. The energy barriers were found to be 0.23 and 0.52 meV/atom for translation and rotation of the tubes. As this energy barrier scales with length, it was concluded that for very short segments movement would be possible.

The nanotubes chosen by Charlier were a special case, being commensurate, achiral, and having the same wrapping angle. In 2000, Kolmogorov and Crespi investigated the effects on the energy barrier for linear translation of double walled tubes that were incommensurate, commensurate with same wrapping angles, and commensurate with different wrapping angles[65]. For commensurate tubes with the same wrapping angle, the energy barrier for translation scaled linearly with the number of atoms in the system. This agreed quite well with the previous results of Charlier. For incommensurate tubes however, it was found that the energy barrier was quite flat ($< 0.4eV$) and independent of the number of atoms. This was the first theoretical indication that MWCNT might be able to act as low friction linear bearings. Many other research groups have continued to investigate the energy barriers to rotational and translational movement in double walled carbon nanotubes and their dependence upon chiral mismatch[66, 67, 68].

Simultaneous with the theory work done by Kolmogorov and Crespi, MWCNT were demonstrated to act as linear bearings by John Cumings in our research group[69] and by the Ruoff group at Northwestern University[70]. Two separate *in situ* techniques were used for these experiments. For the work performed by Cumings, a manipulator was used *in situ* in a high resolution transimission electron microscope (HRTEM). Using this manipulator, a MWCNT could be approached with a probe. By applying a voltage pulse the outer walls of the MWCNT could be vaporized (Figure 2.2b), leaving the inner core tubes intact. Then through a smaller voltage pulse mechanical contact could be established with the inner core (Figure 2.2c). Once connected, the inner core nanotubes could be extracted and inserted repeatedly (Figure 2.2d) without any signs of wear on the atomic scale thus demonstrating that MWCNT could act as low friction linear bearings. If the mechanical contact between the inner core nanotubes and the probe was broken, the inner core nanotubes were immediately pulled back into the MWCNT through the van der Waals interaction (Figure 2.2e). A TEM micrograph of a MWCNT with its inner core fully extracted is shown in Figure 2.2f.

The experiments performed by the Ruoff group used an *in situ* manipulation system placed in a scanning electron microscope (SEM). Using the manipulator and electron beam induced deposition (EBID) of organic material, nanotubes were mounted in-between two atomic force microscope (AFM) tips. The nanotube could then be stressed to failure. The nanotubes were shown to exhibit a "sword-in-sheath" mode of failure where the combined length of tube attached to both AFM tips after failure was longer than previous to failure. After failure, and prior to fully extracting the failed tube, the flexure of the AFM tips was used to calculate the extraction force required to remove a tube.

Because of the van der Waals interaction, a constant restoring force opposes the

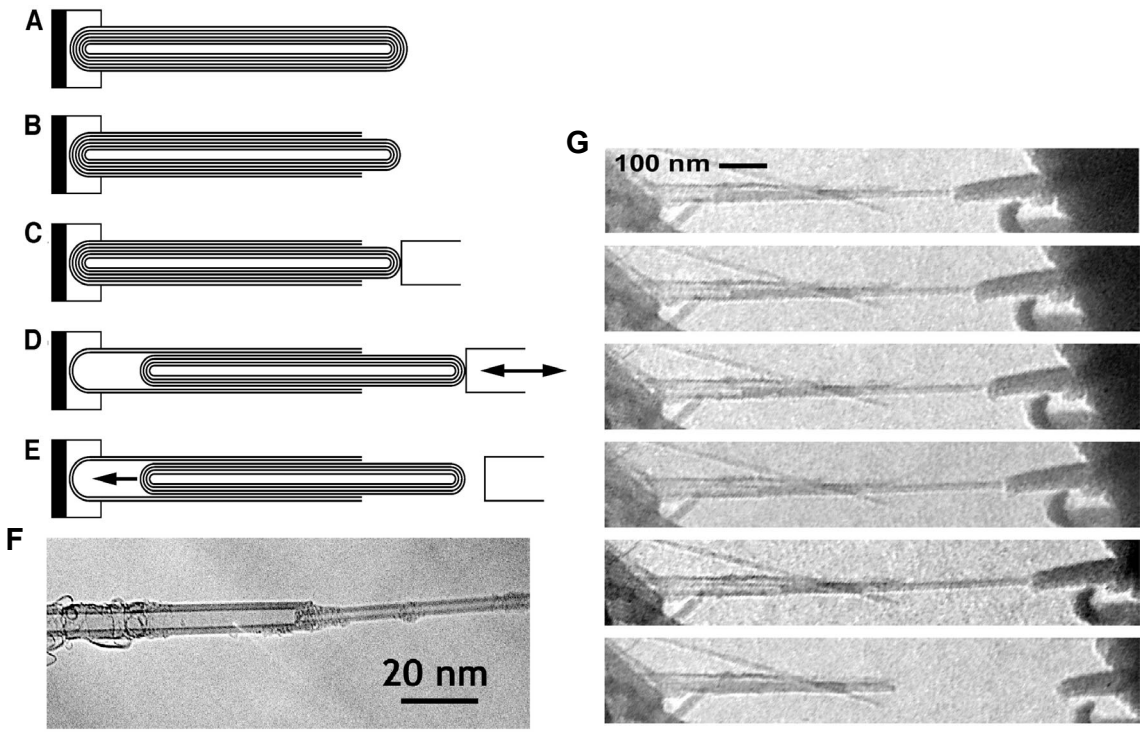

Figure 2.2: (a-e) Conceptual representation of *in situ* creation of a MWCNT linear bearing. (f) TEM micrograph of MWCNT with the inner core of nanotubes fully extracted. (g) Series of sequential video images captured during the extraction of a MWCNT inner core. In the final frame the contact to the manipulator probe is severed and the inner core immediately retracts back into the MWCNT due to the van der Walls interaction. (figures from [69])

extraction of the inner tube. This restoring force was part of the force measured by the Ruoff group and was demonstrated in John Cuming's experiments when the nanotube-manipulator contact was broken and the inner core was immediately pulled back into the MWCNT. It was proposed that if a MWCNT that is open at both ends has an inner core free to oscillate back and forth through the outer shell, it would have a resonance frequency in the GHz range[71]. Since this original paper was published, many research groups have used molecular dynamics simulations to study the resonance frequencies and damping mechanisms of these oscillators[72, 73, 74, 75, 76, 77]. While no unanimous conclusions have been reached, the general consensus is that the majority of damping that occurs in this system is due to excited phonon modes and edge effects.

With the demonstration of the linear bearing nature of MWCNTs, the next obvious experimental step is to demonstrate that nanotubes can also behave as rotational bearings. Unfortunately the *in situ* manipulators that were employed for the linear bearing experiments were ill-suited to do this. To perform this experiment we began to look at using electron beam lithography (EBL) and other microelectronics techniques that were being used to electrically contact nanotubes.

2.3 Nanotube devices

Using EBL, an electrical device measuring the transport properties of an individual SWCNT was made in 1997[78]. These techniques have since been combined with many others used in microelectronics fabrication to create many different electronic devices. Some of these devices have demonstrated the possible application of carbon nanotubes as field effect transistors (FETs)[79, 80] and logic devices[81, 82]. Other devices have been used to study novel nanoscale physics such as Luttinger liquid effects[83], room temperature single electron transistors (RTSET)[84], Aharanov-Bohm oscillations and weak localization[81].

With microelectronic techniques becoming more commonplace for fabricating nanotube electrical devices, we began to explore the possibility of using these techniques to create nanotube mechanical devices. We were not alone in this desire to create a mechanical device using nanotubes, many other groups were simultaneously involved in such endeavors[85, 86, 59, 87, 88]. There are many different physical properties of carbon nanotubes that may be exploited for use in mechanical devices. Their flexibility and strength make them ideal for use in a variety of mechanical switches[59] and oscillators[87, 88]. The ability of the walls to slide across each other can be used in many ways. In linear extension this sleeve bearing structure could be used as a constant force spring[69], nano-rheostat for

a stress sensor[89], mechanical switch[90], GHz oscillator[71] or even a nano piston. The MWCNT should also be able to act as a rotational bearing where it could be used to create nanoscale motors and other NEMS involving rotational movement. As our group had already demonstrated the linear bearing nature of MWCNT we were quite interested in also demonstrating their ability to act as a rotational bearing. Our primary goal in creating a nanoscale electromechanical device using carbon nanotubes was to create a device that would allow us to demonstrate this.

Our first conceptual drawing of a synthetic motor using a MWCNT for the axle and bearing was created by Michael Fuhrer and is shown in Figure 2.3. In our conceptual design a MWCNT is suspended above a substrate through a series of metal supports. The outer walls of the MWCNT have been fractured and removed so that the center section, which is encompassed by a rotor, will be free to rotate. Like the original MEMS micromotors, the rotary motion is driven through electrostatic attraction between outer stators and an inner rotor. The axis of rotation is now parallel to the surface, rather than the perpendicular configuration we are used to seeing in MEMS micromotors. This was done because all previous electronic devices used nanotubes lying along, rather than perpendicular to the surface. The next section will deal with the many ways in which we attempted to fabricate a MWCNT motor with this basic design. While many of the post-docs, graduate students and undergraduate students in our group contributed to this effort, a vast amount of the experiments detailed in the section were done in close collaboration with Tom Yuzvinsky, whose invaluable contributions made their success possible.

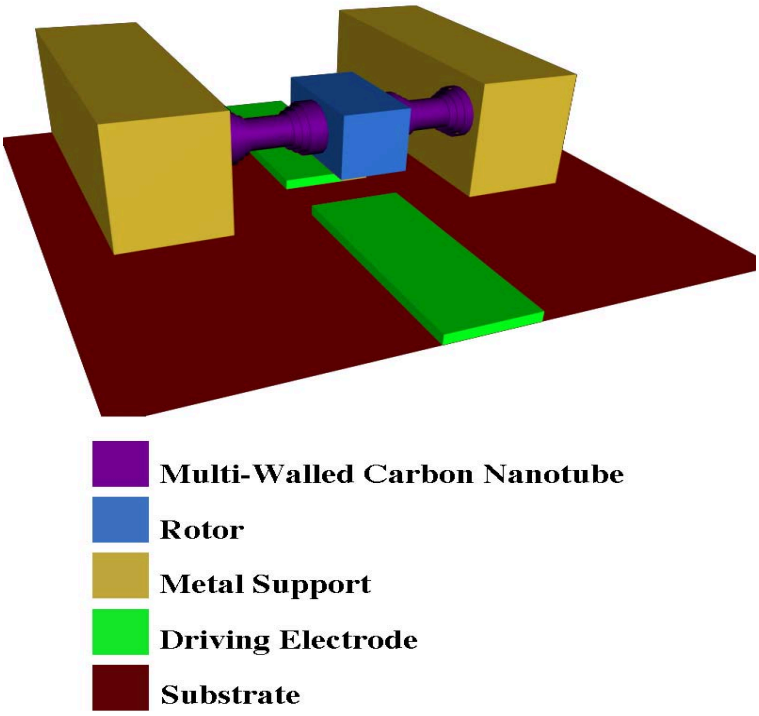

Figure 2.3: Conceptual design of MWCNT nanomotor, as drawn by Michael Fuhrer.

Chapter 3

Nanomotor Construction

3.1 Device Architectures

3.1.1 Introduction

To create a MWCNT NEMS device where the rotary bearing nature of a MWCNT could be demonstrated, three different device architectures were pursued. Each of these architectures exhibited distinct advantages and obstacles. In the following sections we discuss the architectures that were pursued to create the first MWCNT motor device.

3.1.2 Solid Substrate

Through our contact with the McEuen research group we were able to obtain a good orientation to general electron beam lithography (EBL) techniques that were currently being employed to electrically contact individual carbon nanotubes. With a better understanding of what was currently possible we were able to make our first designs for a MWCNT NEMS rotor. For these devices MWCNT which had been deposited on a SiO_2 surface would be contacted with anchors and a rotor and surrounded by two metal stators

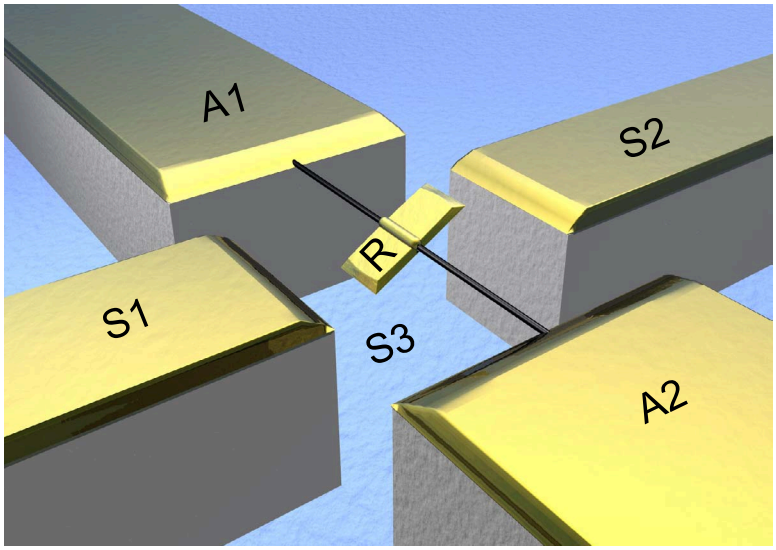

Figure 3.1: Geometry of a MWCNT motor on a solid substrate. A MWCNT is suspended through two anchor electrodes (A1 & A2) and is contacted by a rotor plate (R). The position of the rotor plate is controlled through two opposing metal stators (S1 & S2) and the conducting substrate acting as a third stator (S3).

using EBL. The geometry of the stators, rotor and anchors is shown in Figure 3.1. The two metal stators combined with the conducting Si substrate which functions as a third, allow the rotor orientation to be controlled through electrostatic forces resulting from applied voltages. The rotor paddle and nanotube are suspended through recession of the SiO_2 surface through a wet etch. The anchor pads serve to establish electrical contact to the MWCNT/rotor assembly and to keep the nanotube suspended above the recessed SiO_2 surface.

A general illustration of the steps involved in fabricating these devices is shown in Figure 3.2. MWCNT were deposited out of solution (typically DCE or ODCB) on a substrate where a series of registry or alignment marks had already been deposited. A 500 μm thick degenerately doped Si$\langle 100 \rangle$ wafer with a surface coating of 1 μm of thermally grown SiO_2 was used as the substrate. Once the MWCNT were deposited the surface was mapped with AFM to determine the precise location and character of various MWCNTs.

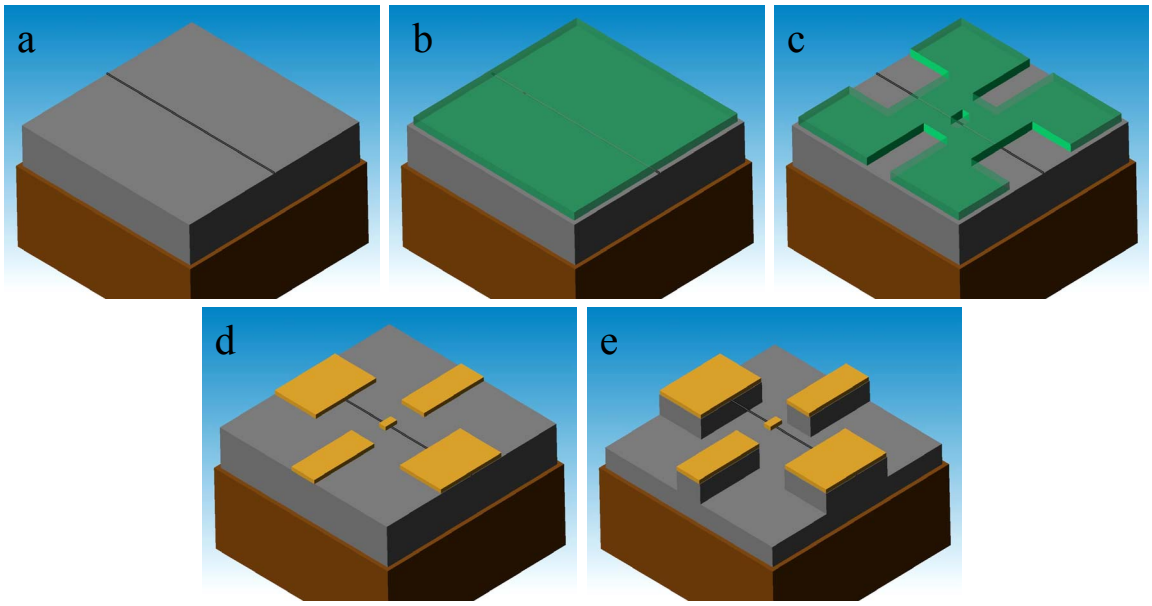

Figure 3.2: Fabrication method for MWCNT motor devices on a solid substrate. MWCNT (a) deposited on a SiO_2 substrate are mapped and (b) coated with electron beam resist then (c) patterned. (d) Anchors, stators and a rotor are patterned through Cr/Au liftoff. (e) The MWCNT and rotor are then suspended through a wet chemical etch.

As we continued to make these devices we began to use FESEM to map the position of the MWCNT rather than AFM as the time and difficulty required in obtaining a detailed SEM image of the MWCNT was significantly less. With a complete mapping of the MWCNTs relative to the alignment marks the contact patterns of anchors rotors and stators to be created through EBL could be designed using DesignCad software. The samples were then coated with electron beam resist and loaded into an e-beam writer. A JEOL 6400 or an FEI XL-30 Sirion SEM fitted with Nabity Pattern Generation System (NPGS) were used as the e-beam writer. The e-beam writer registered to overall alignment marks and patterned the electrode configuration for the device. The exposed resist was then developed for 2' in MIBK:IPA 1:3 solution which removed the exposed areas. The sample was then placed in a thermal evaporator where a thin (1-5 nm) layer of Cr followed by a thick layer (50-80 nm) of Au were deposited. This metallic layer adheres to the substrate in the areas where the

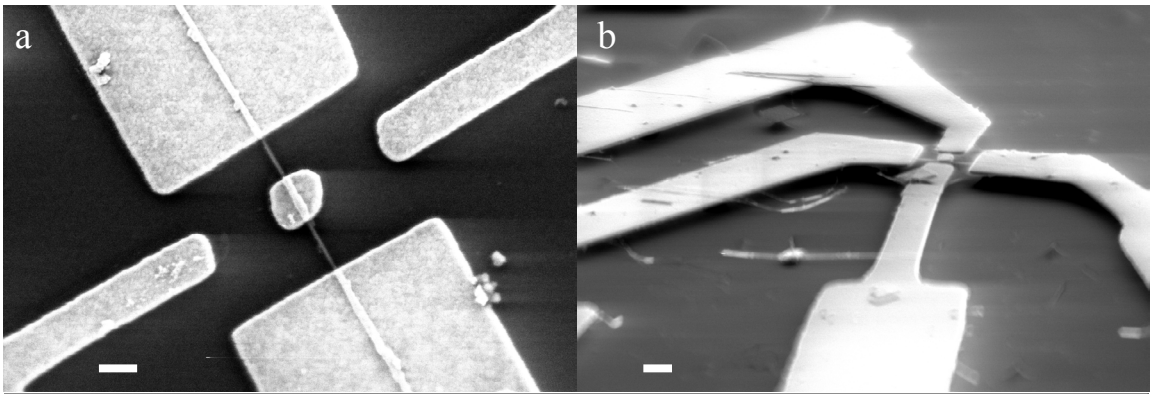

Figure 3.3: MWCNT motor devices on a Si substrate (a) prior and (b) subsequent to the BOE etch. Scale bars are (a) 300 nm and (b) 1 μm.

resist was removed through exposure and development. The remaining metal deposited on the resist is removed with a "liftoff" step in an acetone soak. The duration required in the acetone soak ranged from overnight to less than 30 minutes depending upon the condition of the resist and the temperature of the acetone. Shorter liftoff times were achieved with hot acetone ($\sim 80°$C) and resists which have not had a high thermal load during deposition. A nanotube device formed by this process is shown in Figure 3.3a.

Once the electrode patterns were formed through EBL and Cr-Au liftoff the nanotube was suspended through a wet etch of the SiO_2 substrate. By etching the sample for 9 minutes in a 10:1 Buffered Oxide Etch (BOE) solution $\sim$ 600 nm of the surface was removed. The BOE solution was replaced with DI water through repeated aspiration-dilution cycles. This water solution was then replaced with methanol by the same manner. The samples were then transferred from the methanol solution to a critical point dryer (Tousimis 815) so that they could be removed from solution without surface tension effects destroying the suspended device. An SEM image of a suspended device is shown in Figure 3.3b. With the tube and rotor suspended, the final step to creating the MWCNT motor device was to compromise the outer wall of the MWCNT so that the rotor would be free to rotate. A

variety of methods were used to perform this and are later discussed in Section 3.3.

3.1.3 Electron Transparent - SOI

The original MWCNT linear bearing experiments had the distinct advantage of being able to resolve on the atomic level the behavior of the MWCNT during extension. This allowed John Cumings to conclusively prove that the linear extension was caused by inter-wall sliding, and thus was able to thoroughly investigate the possibility of wear and fatigue on the atomic level. While our initial work on solid substrates made it possible to fabricate a number of devices, all of our characterization was limited to SEM. In hopes of being able to perform rotary bearing experiments *in situ* in the TEM we pursued two different electron transparent architectures. One of these architectures was based upon Silicon-On-Insulator substrates (SOI).

SOI substrates are routinely used in the creation of MEMS devices. An SOI wafer consists of a thin Si layer (50 nm-100 μm) attached to a handle wafer of Si (500 μm thick) by a layer of SiO_2. The thin layer of Si is easily micromachined and then can be released from the larger handle wafer through a wet etch of the SiO_2. By using a Deep Reactive Ion Etch (DRIE) to completely etch through the thin Si layer, a window for TEM imaging may be formed. Aileen Wang had done exactly this for *in situ* mechanical measurements of MWCNT. Aileen had also been developing some promising methods for the placement of individual MWCNT on her devices. With her help we began to investigate the use of SOI to create an electron transparent MWCNT motor device.

The fabrication method used is shown in Figure 3.4. Anchor and stator electrodes were first formed using optical lithography and Cr/Au liftoff (Figure 3.4a). The shape of the anchors had been altered slightly so as to enhance our ability to deposit a single

MWCNT through dielectrophoresis and fluidic trapping. These methods are discussed in more detail in Section 3.2. Once the electrodes were formed, a very thick layer of photoresist was deposited to act as a mask during the DRIE. The photoresist in the area between the anchors and stators was removed through an optical lithography step (Figure 3.4b). The DRIE through the silicon substrate was performed in a Surface Technology Systems Advanced Silicon Etch system (Figure 3.4c). Once the Si layer had been micromachined and the photoresist removed (Figure 3.4d) the substrate was ready for the deposition of a MWCNT through selective deposition techniques. This MWCNT was then anchored to the substrate through deposition of a second set of Anchor pads through optical lithography and liftoff. Simultaneously with this step, a rotor paddle can be patterned onto the MWCNT (Figure 3.4e). The thin Si layer is then freed from the handle wafer through an etch of the SiO_2 in hydrofluoric acid (HF) (Figure 3.4f). While the methods of selectively placing a MWCNT showed a great deal of promise, the difficulty of their execution combined with the potential of other electron transparent devices led this effort to not progress beyond the MWCNT placement step. The other, more promising, electron transparent architecture is discussed in the following section.

3.1.4 Electron Transparent - Si_3N_4

Boron nitride nanotube (BNNT) silo structures were first synthesized in our research group by Willi Mickelson[91]. These silo structures are similar to CNT peapods where a nanotube is filled with C_{60} fullerenes. Because of the variety of inner diameters found in BNNT the C_{60} have a wide variety of packing structures, leading to the name "silos". The electrical transport in these structures could be quite interesting as the majority of conduction should occur through the C_{60} molecules because of the insulating nature of the

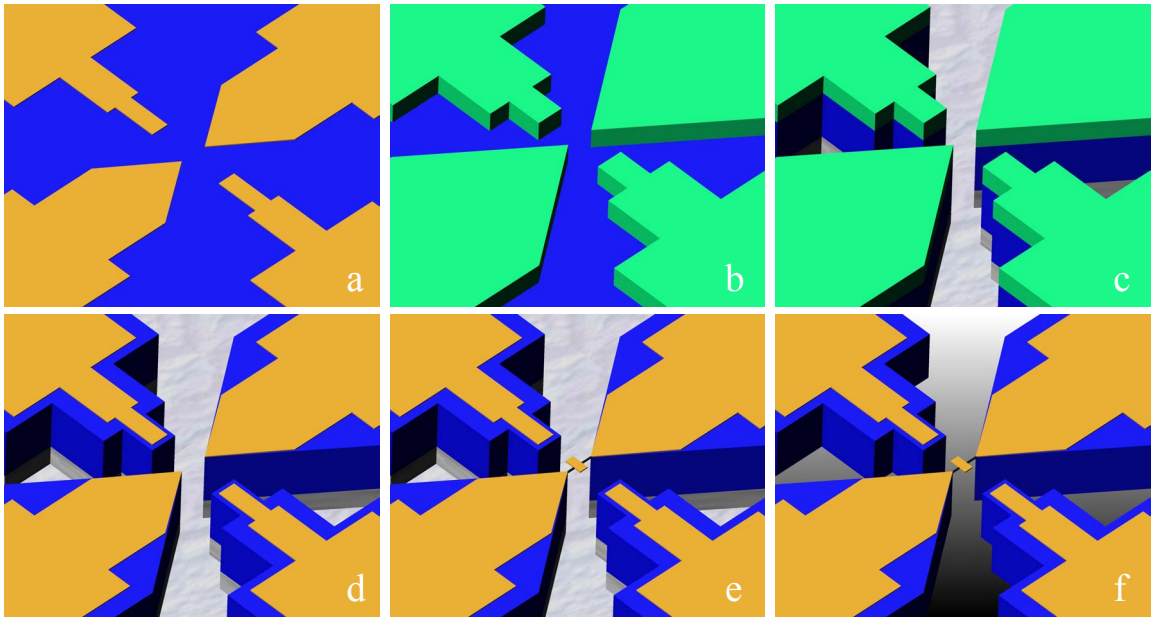

Figure 3.4: Fabrication method for SOI based electron transparent MWCNT motors. (a) Through optical lithography a set of anchor pads and stators are patterned. (b) The substrate is then coated with photoresist and patterned in the areas to be removed through RIE. (c) RIE is then used to etch through the substrate and (d) the resist is removed. (e) A MWCNT is deposited between the anchor electrodes through fluidic and electrophoretic techniques. A second set of anchor electrodes and a rotor paddle are defined through optical lithography. (f) The substrate is then freed from the handle wafer through an HF etch.

BNNT. To truly demonstrate that any transport measurements made were on a silo structure, electron transparent devices were needed for imaging in the TEM. The low population of these structures indicated that random deposition methods on an electron transparent substrate would be far superior to any selective deposition techniques on prefabricated SOI structures.

An ideal candidate for an electron transparent substrate on which electrical measurements could be performed were a series of Si_3N_4 membranes sold by Structure Probe Inc. However upon experimentation with these membranes it was apparent that there were a number of factors which severely limited their usefulness. The Si_3N_4 was too thick to be able to obtain high resolution images. The membrane window was large enough that the strain induced by a layer of electron beam resist would often buckle and fracture the

membrane. Another hurdle that these membranes presented was the lack of any significant dielectric to insulate the electrodes from shorting directly through the Si substrate. Yet the promise of an electron transparent membrane was great. Not only could experiments be performed directly on BNNT silo structures, but it would also be possible to investigate via TEM the electrially driven vaporization (EDV) of MWCNT, MWCNT motor devices, single molecule transport in break junctions, and SWCNT FETs. Unlike the SOI devices where the material must span a fairly large prefabricated gap, smaller materials could be contacted and imaged. The success of electron transparent nanotube devices no longer depended upon elaborate methods of selective placement. With the aim of exploring all of these possibilities I began to fabricate our own Si_3N_4 membrane substrates in the microfabrication laboratory. Once I had constructed basic devices with SiO_2 and Si_3N_4 layers Steve Konsek, a post-doctoral researcher in our group, assumed the reins for the fabrication of membrane devices. Through his patient efforts in exploring the parameter space for Si_3N_4 thin film growth, HF back etching, XeF_2 etching and SF_6 RIE, and alteration of the device architecture to dies of 16 the fabrication process became even more robust and predictable. Figure 3.5 shows many of the steps involved in creating the basic membrane structure.

The Si_3N_4 membranes are formed using a 200 μm Double Side Polished (DSP) Si$\langle 100 \rangle$ wafer. The thinner wafer is used mainly because of the small amount of space available in the TEM. A SiO_2 layer (0.8-1.0 μm) which will serve as the dielectric insulation between the electrical leads and the conducting substrate is grown on the wafer through wet oxidation in a Tystar wet/dry atmospheric furnace. This is then followed by the growth of a thin layer of Si_3N_4 (10-20 nm) in a Low Pressure Chemical Vapor Deposition (LPCVD) Tystar furnace. The Si_3N_4 layer serves primarily as the electron transparent membrane but also acts as an etch mask for an anisotropic wet etch. The wafer is patterned via optical

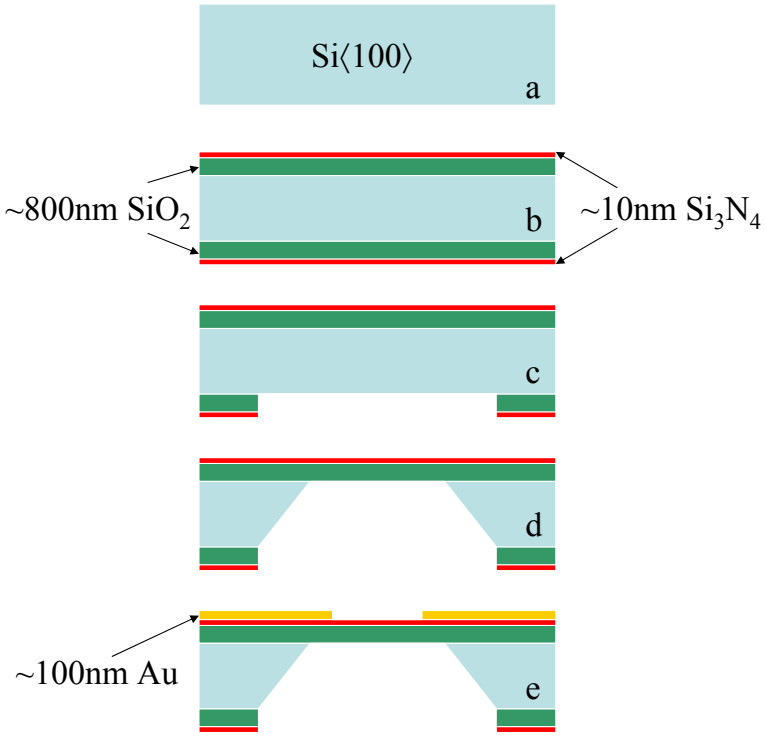

Figure 3.5: Fabrication method of Si_3N_4 membrane. A (a) DSP Si⟨100⟩ is (b) coated with a layer of SiO_2 and Si_3N_4. These layers are (c) selectively removed through an RIE to mask an (d) anisotropic wet etch. (e) Coarse contact pads and electrical leads are then patterned through optical lithography.

lithography for a Reactive Ion Etch (RIE) to remove the Si_3N_4 and SiO_2 layers and expose the Si for the wet etch. After removal of the remaining photoresist, the wet etch is then performed in a KOH solution (1:2 by weight in water) at 80°C. At this temperature KOH is well known to anisotropically etch Si with an etch ratio for the ⟨100⟩ : ⟨111⟩ planes of approximately 400:1. This anisotropy leads to an etch angle of 54.7° allowing the etch window to be designed so that the final membrane window will be approximately 10 mum wide. KOH etches SiO_2 quite slowly (less than half the rate of the ⟨111⟩ plane allowing the etch to be easily stopped when the SiO_2 layer is reached. After the wet etch four large contact pads and leads surrounding each membrane window are patterned using optical lithography and a Cr/Au liftoff. These pads will later be contacted via EBL.

Once this basic membrane is created it is still not electron transparent. To achieve

this the SiO_2 layer must be removed, then routine TEM images can be obtained through the Si_3N_4 membrane. For greater resolution the membrane must either be thinned or completely removed in the area of interest. To make the membranes electron transparent a number of different sequences may be followed depending upon the final resolution needed and the chemical compatibility of the material to be deposited. For materials where high resolution is required which can withstand exposure to HF, a fabrication method is illustrated in Figure 3.6a,e-h where holes patterned in a PMGI e-beam resist were etched through the Si_3N_4 layer via an SF_6 RIE (3.6e). Once the holes have been etched, the nanotubes are deposited (3.6f)and those spanning a hole are electrically contacted via EBL(3.6g). The sample is then coated with a layer of photoresist to protect it while the thick SiO_2 layer is back etched away(3.6h). With the SiO_2 layer removed, the nanotube spanning a hole can be characterized in TEM and via transport.

While the exposure to HF in the SiO_2 back etch is minimized to the last part of the etch, with sensitive materials this exposure is still too much. For these materials it is best to first perform the back etch of SiO_2 on a pristine chip, creating a thin Si_3N_4 membrane (3.6b). This membrane is thin enough that walls on a MWCNT can be discerned. The material to be measured can then be deposited (3.6c) on the thin membrane and contacted through EBL (3.6d).

For materials where high resolution is needed which are also incompatible with the wet etch the Si_3N_4 holes and SiO_2 etch can both be performed prior to the deposition of any material. Unfortunately when using this technique it is quite difficult to have the material span the holes due to the surface tension when drying. For these materials some promising results have been obtained by allowing the HF etch to thin the Si_3N_4 membrane during the SiO_2 etch. While difficult to time the etch so that the membrane is not eliminated

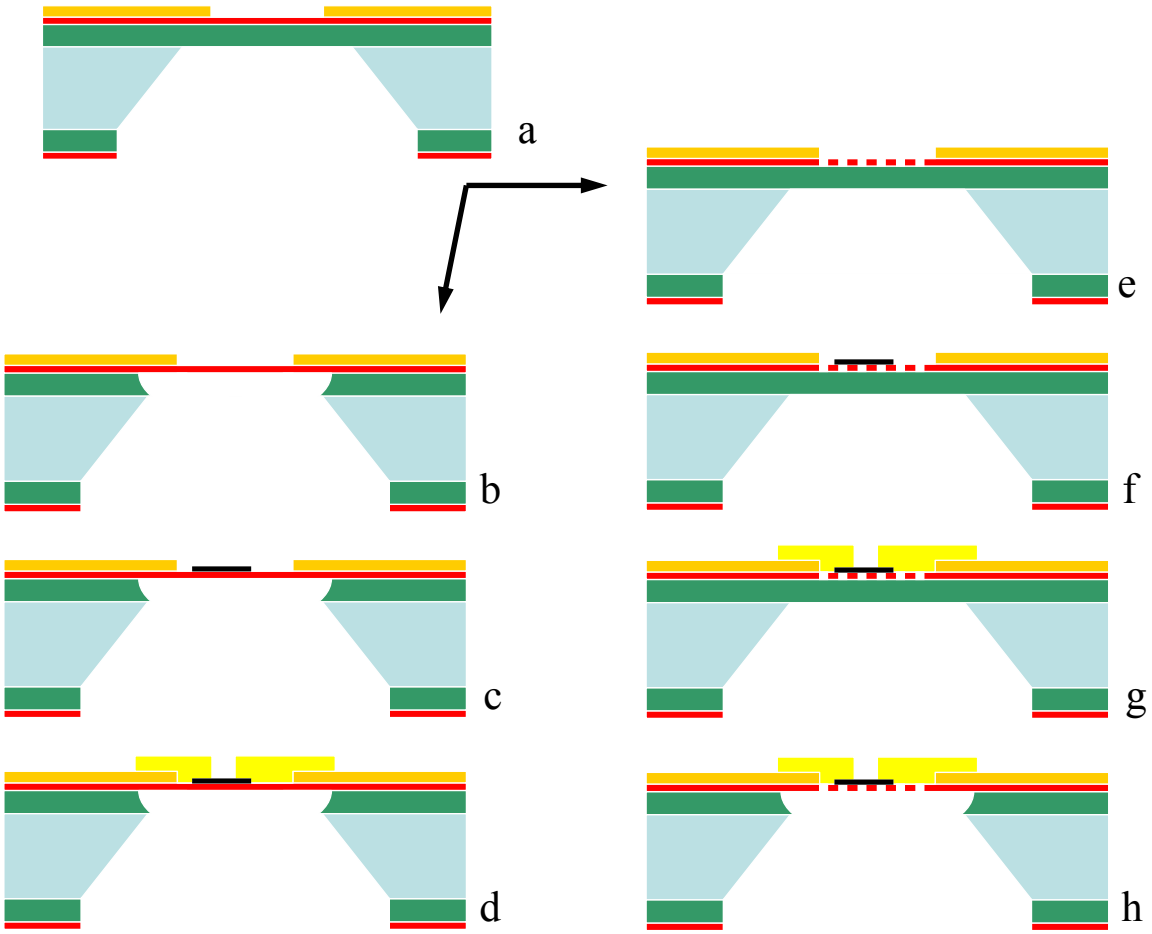

Figure 3.6: Two alternate methods of completing device fabrication on Si_3N_4 membranes for nanoscale materials (a-d) incompatible with HF and (a,e-h) with high resolution requirements.

completely, those devices where the Si_3N_4 membrane was not completely removed did show an improvement in resolution.

The ability to more easily contact MWCNT for transport studies has caused most of our early measurements to be on EDV in MWCNT. Some early MWCNT motor devices however, have been made using these membrane devices and are shown in Figure 3.7. As we are able to increase our success rate with these devices we hope to be able to more reliably produce MWCNT motor and BN silo structure devices.

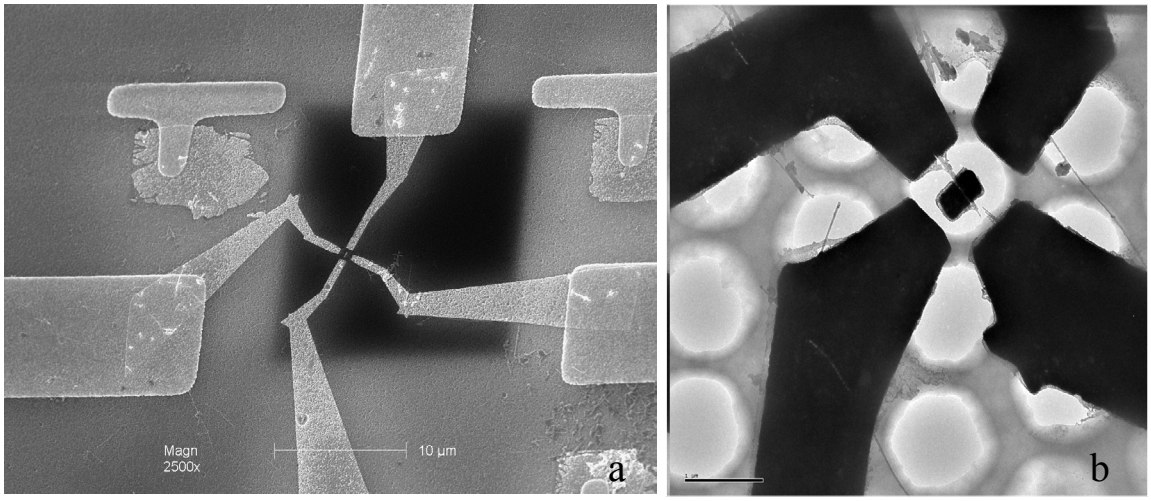

Figure 3.7: (a) SEM and (b) TEM images of two early Si_3N_4 membrane MWCNT motor devices. Scale bars are (a) 10 μm and (b) 1 μm.

3.2 Orientation and controlled placement of nanotubes

3.2.1 Introduction

For most of the early single nanotube devices, nanotubes were deposited in a random fashion out of solution. While this deposition method produced working devices, the yield rate was quite low due to the painstaking process of finding and contacting each device. A good deal of effort has been dedicated to developing methods with greater control over the final nanotube orientation and position. This not only stems from the desire to have greater success in fabricating experimental devices, but also from the hope of being able to incorporate single nanotube devices into large scale manufacturable devices.

In our work with nanotubes we have worked on a number of techniques for controlled placement and orientation of nanotubes. The success of some projects or architectures has depended upon our ability to controllably place a single nanotube in a desired location. Some of these techniques have been developed entirely by ourselves, while others are being developed simultaneously by many research groups. We employed these tech-

niques to achieve high density depositions of non-shorted MWCNT NEMS, deposit ordered arrays of MWCNT for NEMS, and to attempt to place individual nanotubes on our electron transparent SOI structures. These techniques were not only relevant to our work on MWCNT NEMS devices, but also to our work on measuring the thermal conductivity of BNNT where suspended nanotubes must be placed on complex prefabricated structures created by the Majumdar research group in mechanical engineering.

3.2.2 Alignment via Fluid Flow

In depositing MWCNT out of solution via spin coating we found that the nanotubes were often highly aligned. The direction of alignment corresponded to the radial direction from the spin center or the direction of fluid flow. Alignment of nanowires via deposition out of a flowing fluid had already been observed but had not been seen with any nanotube depositions[92]. Although spin coating had been used previously for placing nanotubes on substrates we believe that alignment was not seen due to this effect being highly dependent upon the solvent used and surface chemistry. For our work we have found that we achieve the best alignment for MWCNT placed in orthodichlorobenzene (ODCB), while nanotubes in other solutions more typically used exhibited very little alignment. MWCNT are suspended in ODCB at a concentration of 100 μg/ml by ultrasonication in a VWR Model 75D Aquasonic bath for 60 s at level 3. The solution is then pipetted on to a silicon substrate spinning at least 3000 RPM. Care must be taken to let the substrate dry completely between drops. If not allowed to dry between drops depositions were less dense and less aligned. Alignment is more prevalent for longer sections of MWCNTs with approximately 90% of tubes over 1 μm long lying within $\pm$ 1° of the direction of fluid flow, and 95% within $\pm$ 5°. Alignment can also be seen for SWCNT solutions, but higher speeds

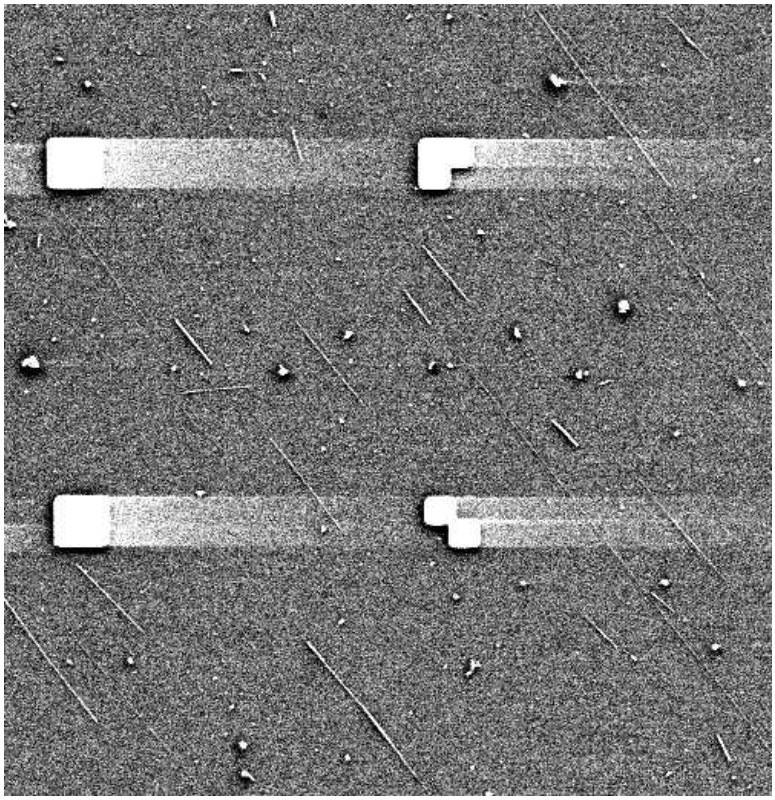

Figure 3.8: Aligned nanotubes deposited on a substrate through spin coating. The spacing between the alignment marks is 8 μm.

of 10,000 RPM are required and the degree of alignment is often lower. Since our original work was performed other groups have begun to use fluid flow to achieve alignment of nanotubes[93, 94], but have used air driven fluid flow instead of spin coating.

We first employed spin alignment to increase the density of nanotubes available for MWCNT motor devices. Because all of the nanotubes were highly aligned, the likelihood of a second nanotube shorting and ruining a device was limited, even at high densities. By increasing the density we were able to choose from a larger amount of prospective MWCNT to find those with proper lengths and diameters. This technique could prove quite useful for a number of experiments. A very tight length distribution of nanotubes could be made if combined with the techniques of Lustig *et al* for nanotube cutting[95]. An array of crossed tube devices could be made through the use of two separate deposition steps, eliminating

the need to fabricate multiple sets of electrodes as done by Heath and colleagues[96] or to fabricate multiple fluidic channels as done in the aforementioned nanowire experiments[92]. Nanotubes may be able to be deposited in predetermined locations to form arrays of single tube devices if combined with surface functionalization techniques. Some surface functionalization techniques developed in our group for use with our alignment technique are discussed in the next section.

3.2.3 Surface Functionalization

Surface functionalization was first used in 1998 by the Roth research group to selectively place nanotubes on a surface[97]. The basic concept of this deposition method was to functionalize the surface of a substrate with a self-assembled monolayer (SAM) terminated by amine groups. When nanotubes are placed in an SDS solution they become negatively charged and are then attracted to where the polar SAM has been deposited. As this technique has been investigated, various solvents, patterning methods and molecules were explored[98, 99, 100, 101, 102, 103]. It has been used to create crossed nanotube devices[99] and most recently an array of SWCNT[103]. While this technique has proven to be quite useful, its success is dependent upon the quality of the SAM, with degraded performance occurring when more than a monolayer is deposited[101]. We have recently developed a unique technique for surface functionalization that does not involve the use of SAMs.

To perform our surface functionalization we first deposit a layer of Poly[methyl methacrylate - methacrylic acid] (P[MMA-MAA] or copolymer) on a Si substrate with a surface layer of SiO_2. This was typically done by spin coating a solution (MMA-MAA EL6) of copolymer at 3000 RPM for 30 seconds. This layer is then baked at 185°C for 3

Figure 3.9: Deposition of aligned MWCNT in a functionalized area. The nanotubes were deposited in higher concentrations at the top and upper right corner as these were the first areas encountered by nanotubes flowing in solution. The alignment of spin coated nanotubes is also visible in this figure. The patterned square to the right of the letters "BL" is 10 μm wide.

minutes. Once the sample has cooled the copolymer layer is removed with an acetone wash of approximately 10 minutes. The acetone wash removes a majority of the copolymer, but leaves a thin layer at the surface. By exposing this remaining surface layer to an extremely large dose in our electron beam patterning system we found we could selectively deposit nanotubes out of an ODCB solution onto the patterned area. One of the first instances of this functionalization is shown in Figure 3.9.

The doses required to pattern the surface layer of copolymer were quite large with a threshold dose of $\sim$ 5000 $\mu C/cm^2$ and an optimal dose of 50000 $\mu C/cm^2$. These doses had to be administered at extremely low acceleration voltages on the order of 1 keV to be effective, if higher voltages were used the effect did not occur. At low acceleration

voltages the scattering cross section of the surface layer becomes quite large, causing all of the electron beam energy to be deposited into the surface layer[104]. When PMMA is exposed to an electron beam at low doseages ($\sim 100\ \mu C/cm^2$), scission occurs causing the exposed resist to be soluble in developing solutions. At higher doses ($\sim 1000\ \mu C/cm^2$) the PMMA becomes cross linked and is no longer soluble in most solvents. The doses required combined with the energy deposited through low acceleration voltages indicate that in our surface layers we may have moved beyond the highly cross-linked structure, known to form at high electron doses, to form a graphitized layer. This graphitized layer was recently shown to form after cross-linking through ion bombardment of PMMA[105].

We have been able to create this surface layer through spin coating and stripping both PMMA and copolymer. While the effect occurs regardless of solution used to deposit the PMMA, it is highly dependent upon the solution used for nanotube deposition. Our best results were seen when using nanotubes deposited out of ODCB. Methoxybenzene, also known as anisole, exhibited some localized deposition while no effect was seen in nanotube solutions of dichloroethane, IPA, acetone, and ethyl lactate. The need for ODCB to perform localized deposition may be related to the recent results that ODCB is known to form a sonopolymer which irreversibly interacts with nanotubes when subjected to ultrasound[106]. While our nanotube solutions were exposed to much less sonication than those in the sonopolymer experiments upon examination in the TEM our mostly pristine nanotubes did have isolated sections covered by amorphous material. Whether this preferential interaction with the PMMA layer is caused by the presence of a sonopolymer or the charge transfer between the nanotubes and the solution is still unclear.

Once this technique was developed we began to use it in combination with fluidic alignment through spin coating to preferentially deposit nanotubes. We found that by using

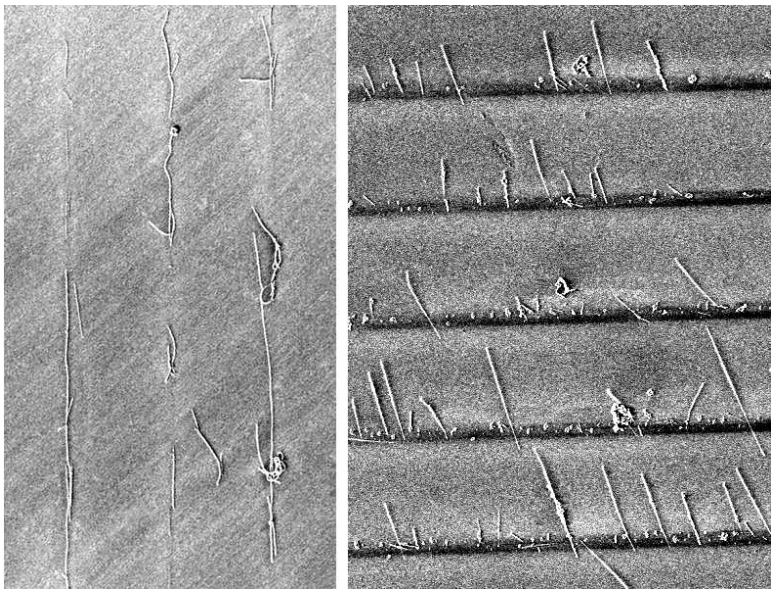

Figure 3.10: Nanotubes deposited through "snagging" on functionalized lines. In the left image SWCNT have been deposited through fluid flow parallel to functionalized lines while on the right MWCNT flowed perpendicular to the functionalized lines

fuctionalized lines perpendicular or parallel to the direction of fluid flow we could "snag" the nanotubes as they flowed along the surface and deposit aligned nanotubes in selected locations. Some of these depositions on functionalized lines are shown in Figure 3.10. By creating an array of small parallel functionalized lines we were able to deposit an array of nanotubes for use as mechanical devices which is shown in Figure 3.11.

While able to create small arrays for mechanical devices we did see a great deal of variation from section to section of our larger scale arrays. The key obstacle that we found in limiting the effectiveness of this technique was that along with selective deposition of nanotubes, graphitic onions and other nanoscale materials that accompany carbon nanotubes were also deposited. The deposition of this "nanojunk" often coated an area before a nanotube could be deposited. Hopefully with more pure materials the arrays would more closely rival those reported by Rao *et al*[103].

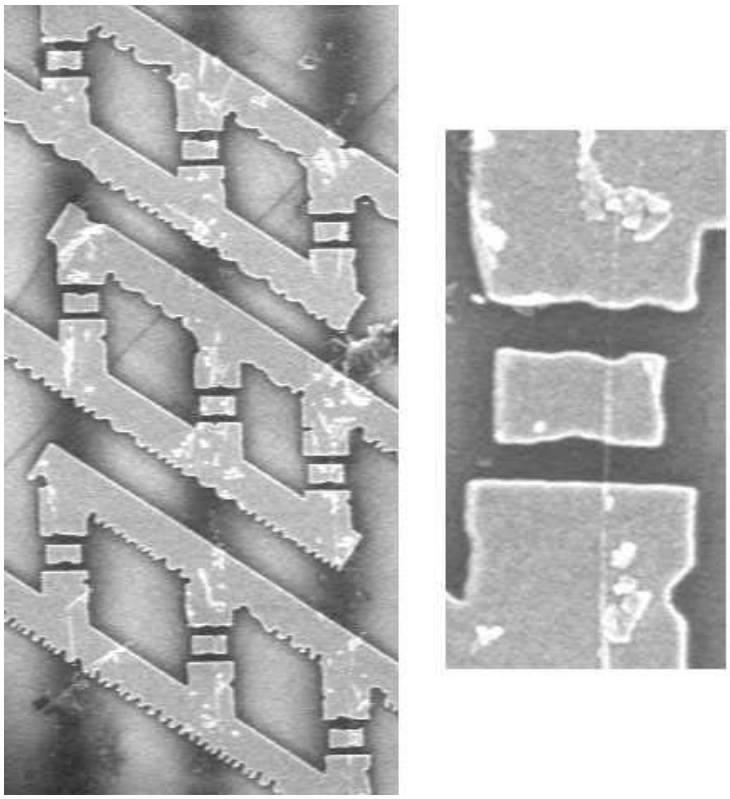

Figure 3.11: An array of MWCNT mechanical devices created using functionalization and alignment techniques. Each of the devices contains a single MWCNT contacted by two anchors and a paddle as shown in the image at the right.

3.2.4 Fluidic Trapping

As we have mentioned previously, a member of our research group, Aileen Wang, had done some preliminary work on using the surface tension of a drying liquid to controllably place nanotubes on a device[107]. As a nanotube solution which had been placed on a device evaporated, the remaining solution would reside in small crevices or trenches through capillary action. With the evaporation of this constricted, its solute (typically carbon nanotubes and other amorphous material) would be deposited across the channel. Fluidic trapping to place nanotubes across trenches had been done by another research group, but without the position control that was present in Aileen's method[108]. Some MWCNT that were deposited using this method are shown in Figure 3.12. This was one of

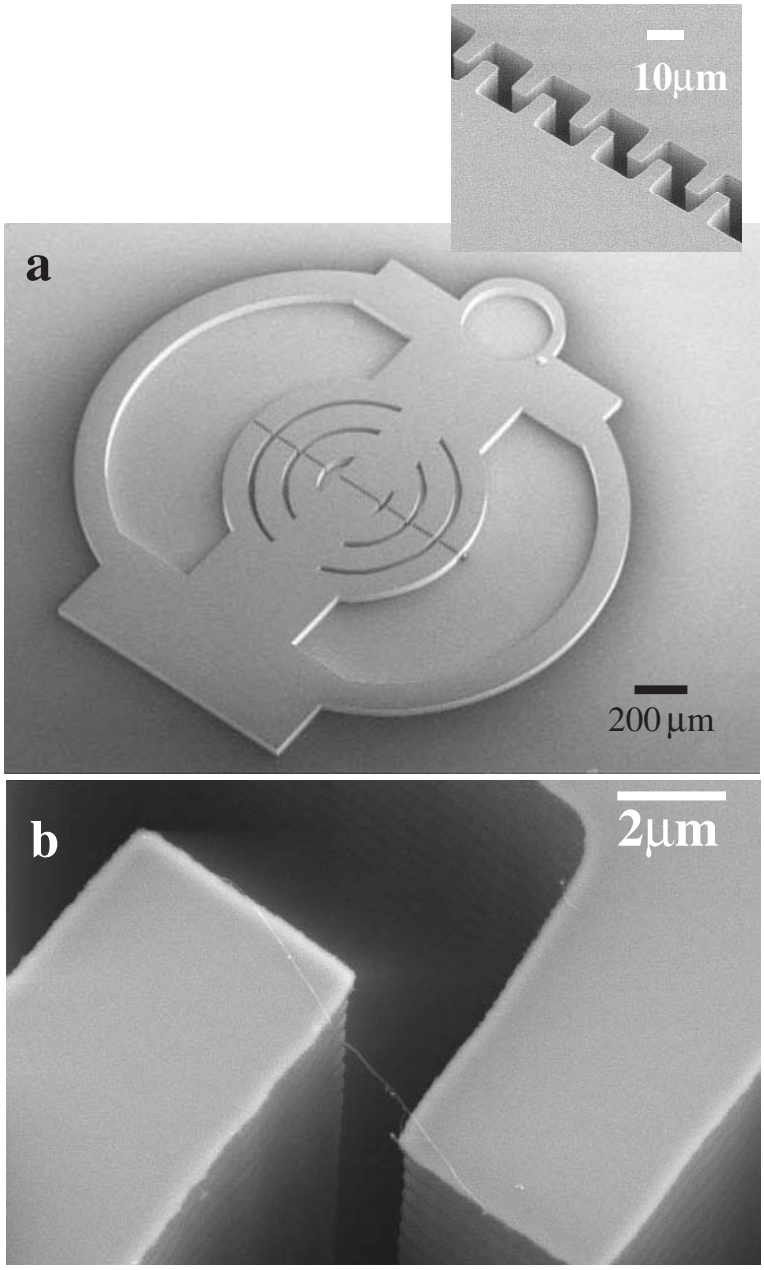

Figure 3.12: SOI structure developed by Aileen Wang for fluidic deposition of MWCNT. The entire structure is shown in (a) with the inset showing the interlocking tooth structure of the center gaps. (b) Through surface tension enhanced deposition approximately 50% of the tooth gaps are spanned by individual tubes.

the first methods that was used in our group to controllably place nanotubes in a desired location.

In hopes of exploiting this method and electrophoretic techniques we developed

the devices discussed in section 3.1.3. We also employed this method for the deposition of BNNT on thermal conductivity measurement devices. While this technique worked quite well for Aileen we found ourselves having much less success. For the BNNT thermal conductivity devices where this was used as the sole technique it worked adequately but with distinct differences from previous experiments. Rather than deposit individual tubes, this method preferred deposition of ropes or even dense fibers of BNNT. Our success rate was also markedly less, closer to 5-10% rather than the 50% previously reported. Some of the ropes and fibers that were deposited are shown in Figure 3.13. For the SOI based motor devices we combined the use of surface tension and electrophoretic techniques. These devices encountered the same problem, with large fibers of nanotubes being deposited rather than individual tubes. The results of this deposition are shown in Figure 3.14.

Considering the factors at play in this deposition method, it is quite expected that ropes will be predominantly deposited. As the constricted solution evaporates the solute becomes quite concentrated, causing all of the nanotubes to agglomerate and form ropes or dense fibers. To deposit a thin rope or single nanotube in the area of interest it would be essential to tune the nanotube density to just the proper point. At higher densities thick ropes will be deposited due to the number of tubes present in the constricted droplet, and at low densities the success rate will be abominably low. To deposit thin ropes the solution density was tuned to the most dilute concentration with reasonable success rates. To aid in the evaporation of the solution the sample was maintained at a temperature of 80°C while $\sim$ 30 drops of dilute solution ($\sim$ 20 μg/ml in ODCB) were deposited. Depositing a single tube using this method proved to be practically impossible for our devices.

In retrospect it is actually quite amazing that Aileen was able to produce the depositions that she did. A number of factors may have contributed to her ability to do

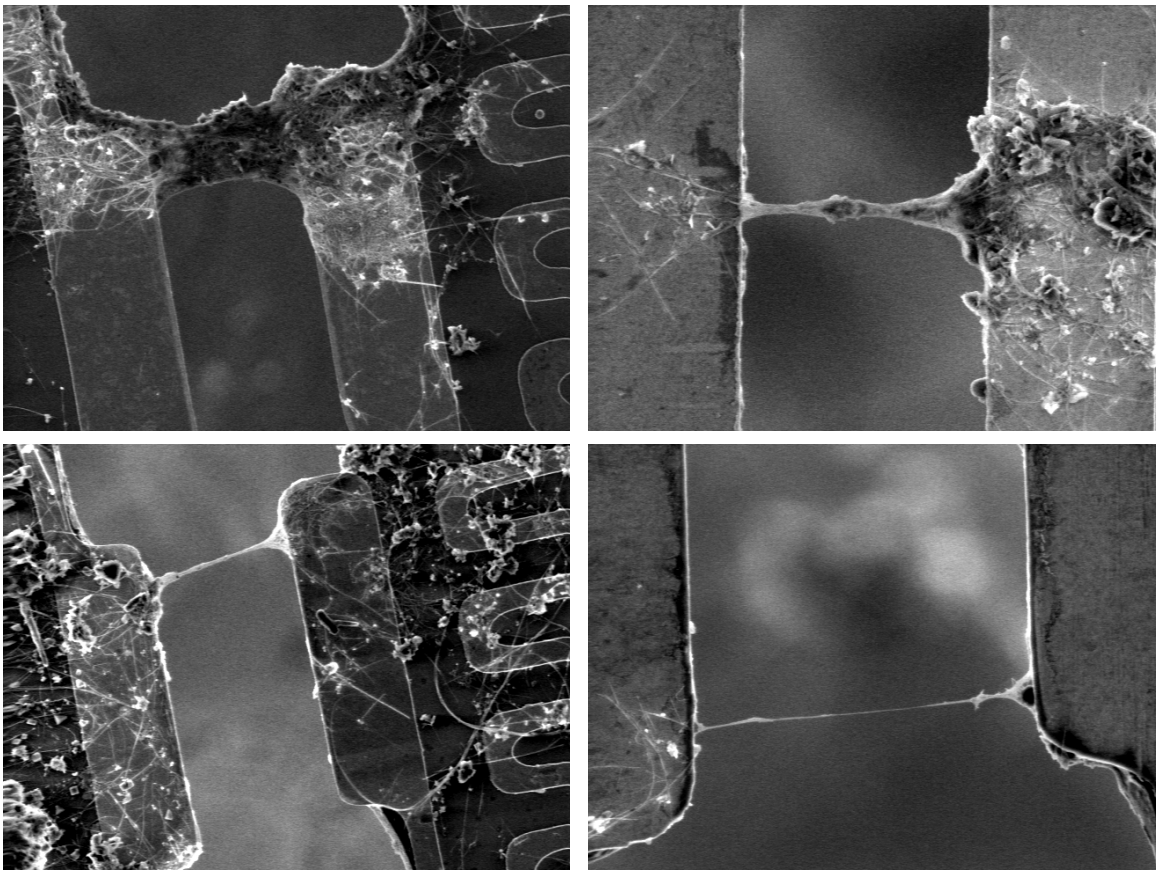

Figure 3.13: Deposition of BNNT through fluidic trapping on thermal conductivity devices. The gap between the two electrodes is ~ 2.5 μm.

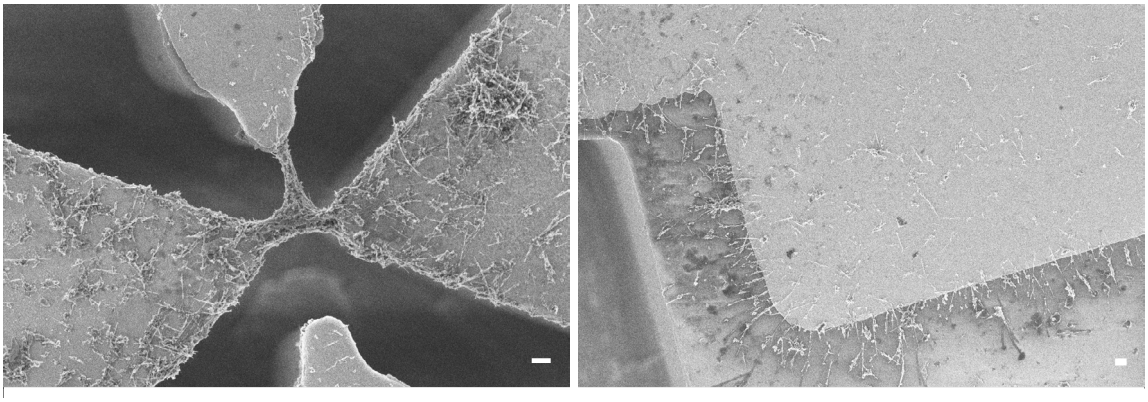

Figure 3.14: MWCNT deposited on an SOI motor device via fluidic trapping and AC DEP. Scale bar is 1 μm.

this without an exact tuning of nanotube density. First the channel where nanotube solution was constricted in her depositions was considerably larger, about 100×50 μm as opposed to $7 \times 2.5 - 5$ μm, and deeper. Unknowingly this large, deep channel may have changed the dynamic as to how the solute was deposited and possibly prevented the concentrating effect that we originally thought was key. Whereas in our devices a small amount of fluid is caught between two surfaces and tended to deposit all of the solute that it contained, it is possible in Aileen's devices the deposition was caused more by tubes becoming caught as the fluid was drawn into the large capillary channel. Another factor that may have contributed to this effect is the average length of tubes used by Aileen were much longer, making them more likely to be caught on the channel at lower densities. Aileen's success and our ability to deposit suspended ropes on a devices suggest that this technique can still be quite useful, but care must be taken in understanding and choosing the proper geometry as this appears to be a key factor in the methods usefulness.

3.2.5 Electrophoresis

Electrophoresis and AC dielectrophoresis (DEP) are useful techniques that are often used for manipulation and separation of small particles and cells[109, 110]. In electrophoresis movement is driven by the charge of the particles in solution, causing them to move in a static electric field toward the electrode of opposite charge. DEP exploits the induced polarization of the particles for alignment and movement of the material in both static and dynamic electric fields. These techniques were first employed by the Nakayama research group to align nanotubes between electrodes[111, 112]. Aileen Wang began to use these techniques in combination with her fluid trapping techniques to deposit MWCNT out of an acetone solution.

From Aileen's early success we were inspired to pursue her techniques further in hopes of depositing a single MWCNT on the electron transparent SOI motor device discussed previously (see Section 3.1.3). Prior to depositing a MWCNT on our SOI motor devices we investigated the use of various solutions, voltages, and frequencies on devices of interdigitated electrodes (IDE) as these were more easily fabricated on a large scale. The results that we found agree quite well with those that have since been obtained by other research groups[111, 112, 113]. We found that with DC voltages we saw both electrophoresis and dielectrophoresis. Electrophoresis was evident from the electroplating of MWCNT on either the positive or negative electrode depending upon the charge acquired by the nanotube in solution (nanotubes in ODCB and IPA plated the negative electrode, while in acetone they plated on the positive electrode). Dielectrophoresis was evident from the propensity of nanotubes to be deposited in areas of fringing electric field. Like other research groups we found that AC dielectrophoresis (AC DEP) in the MHz region was a more powerful technique for depositing nanotubes as it would align nanotubes and deposit them at the edge of the electrodes rather than electroplate the majority of MWCNT on the electrodes[112, 113].

Up until this point all AC DEP depositions of nanotubes had only been used to deposit large quantities of nanotubes between parallel electrodes. We hoped that by tailoring the electrodes and using fluid trapping we would be able to deposit single nanotubes due to the concentration of field and fluid between two pointed electrodes. A 10 or 100 MΩ in series resistor was employed so that once a nanotube had been deposited and made electrical contact, the current would be limited to avoid damage from the applied voltages, and hopefully to prevent further deposition of other tubes by transferring the voltage drop from the electrode gap to the current limiting resistor.

We found that rather than deposit individual tubes our devices tended to be spanned by large bundles of tubes. Many factors led to this concentration of tubes. As we mentioned in the previous section, our change in architecture from the long trenches employed by Aileen most likely changed the manner in which the fluid dried and caused all solute to be concentrated in the fluidic traps. The gap between electrodes was much longer than our average MWCNT length, so many tubes would span the gap collectively before a nanotube of adequate length would be able to. The inability of tubes to make good electrical contact to the electrodes caused deposition to continue to occur even when the gap had been spanned by a small rope of nanotubes. A picture of one of these devices post AC DEP deposition is shown in Figure 3.14.

We were actually not alone in this approach of hoping to deposit a single tube between electrodes through AC DEP, many other groups were also attempting to do this[114, 115]. One group even has succeeded in what we had originally attempted to do, make good electrical contact between a single MWCNT or rope and the electrodes in solution thus stopping further deposition, through the use of Ag electrodes[115]. Using AC DEP, preliminary work has been done attempting to exploit the large difference in dielectric constant between metallic and semiconducting SWNT to separate them[116, 117, 118]. With the knowledge that we have obtained, combined with that of others, it might be possible to revisit this experiment and have a much higher level of success. By using Ag contacts, longer MWCNT tubes and eliminating or better engineering the effects of fluidic trapping it might be possible to place individual MWCNT on SOI devices.

We later used these techniques to orient nanotubes on razorblades so that they overhang the edge. By overhanging the edge they are approachable by our *in situ* manipulation system for mounting on tips for biological or SPM probes, TEM investigation,

or for placement on prefabricated devices such as the thermal conductivity devices. This technique of placing nanotubes on a razorblade was originally pioneered by the Nakayama research group[119]. Andrei Afanasiev worked extensively on refining the technique in hopes of maximizing the number of tubes extended over the edge and their overhanging length. To do this a variety of solutions (ODCB, DCE, IPA, & Acetone) were used in combination with a variety of architectures. In the first architecture an STM tip or razor blade was barely removed out of contact with a counter electrode in solution through the use of a micropositioning stage. It was supposed that this would achieve the best results because the small gap between the electrodes would increase the magnitude of the electric field and concentrate the gradient. However it was found that for an architecture where two razor blades placed on a glass slide with their edges parallel and opposing and separated by approximately 0.5mm yielded better results. In this architecture the best results were achieved when an AC voltage of 40V P-P at 1MHz with a 100 V DC offset was applied while dropping about 5 drops of a 15 μg/ml acetone solution into the gap. While this would produce razorblades with a high density of aligned MWCNT overhanging the edge, the success rate was still only about 10%. An image of one of these successful razor blades is shown in Figure 3.15.

The possibility of depositing BNNT using electrophoretic methods was also investigated. While their low dielectric constant relative to MWCNT made them an unlikely candidate for AC DEP the charge transfer with the surrounding solution (acetone) allowed them to be electroplated on the negative electrode through electrophoresis. Unfortunately this charge transfer was inadequate to deposit BNNT in an aligned manner on any razorblades.

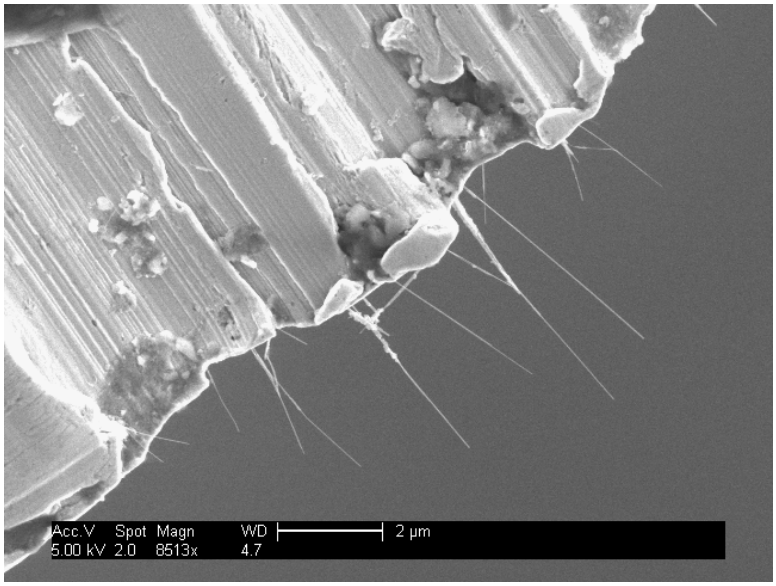

Figure 3.15: Aligned overhanging MWCNT deposited via AC DEP on the edge of a razorblade.

3.2.6 Nanomanipulation

With the limitations of fluidic trapping and electrophoretic methods to manipulate single nanotubes it became apparent that to measure the thermal conductivity of a single BNNT or to place a single MWCNT on an electron transparent structure it might be best to pursue a method of directly manipulating nanotubes. We purchased a commercially available nanomanipulator (attocube ANPx,y,&z100) for use *in situ* in our FEI XL-30 Sirion SEM for nanomechanical measurements and direct nanotube manipulation. The attocube had the advantage of a large range of movement (7mm in x, y, & z) with precise movement on the order of 1 nm while being significantly less expensive than other manipulation setups.

Nanomanipulators had already been used to create nanotube SPM tips by the Nakayama research group[119]. We hoped to use these techniques combined with some of our own to be able to create SPM tips, biological probes, and to place individual tubes on thermal conductivity devices. A stage was built to hold the attocube, and make it possible for SPM tips attached to the attocube to approach various ceramic packages we commonly

use to mount our device substrates (16 pin DIP socket & 28 pin PLCC) or free standing structures with nanotubes such as razorblades with oriented overhanging MWCNT and tungsten wires with BNNT fluff. We could approach SPM tips (either AFM tips or etched tungsten STM tips) to the razorblade or BNNT fluff and contact an individual nanotube. Our original experiments utilized the van der Waals interaction to attach the free end of the nanotube to the tip. The nanotube was then cut using the electron beam to free it from the razorblade. This cutting method is discussed in greater detail in a later section (3.3.5). The nanotube could also be broken through EDV, this method is discussed more fully in Section 3.3.4. With subsequent voltage pulses the nanotube could be shortened and even sharpened following the methods developed by John Cumings and Phil Collins[120].

While this method worked quite well, allowing us to mount nanotubes of desired length onto tips, the method was a bit finicky in which nanotubes could be mounted and how a nanotube would lie on the tip due to the van der Waals interaction. By using electron beam induced deposition (EBID) of Pt through the use of a gas introduction system (GIS) a nanotube could be "glued" to a tip in any position with a much stronger mechanical contact. A 20-30 second exposure with the GIS needle fully retracted at an acceleration voltage of 2kV and a probe current of $\sim$ 55pA (spot 3) and a magnification of 150kX (photo mode) proved adequate to achieve stable mechanical contact to the nanotube. Through TEM investigation we were able to find that the Pt deposition was localized primarily to the tip area, with small Pt balls being present no more than 0.5-1 μm away from the deposition edge. Pt deposition outside of the area of interest could be minimized by allowing the pressure to fully recover after introducing the Pt metallorganic and maintaining the beam blanked during recovery. Once the nanotube was glued into place it could still be broken through cutting or EDV, or by using the increased mechanical strength of the tip-tube contact the

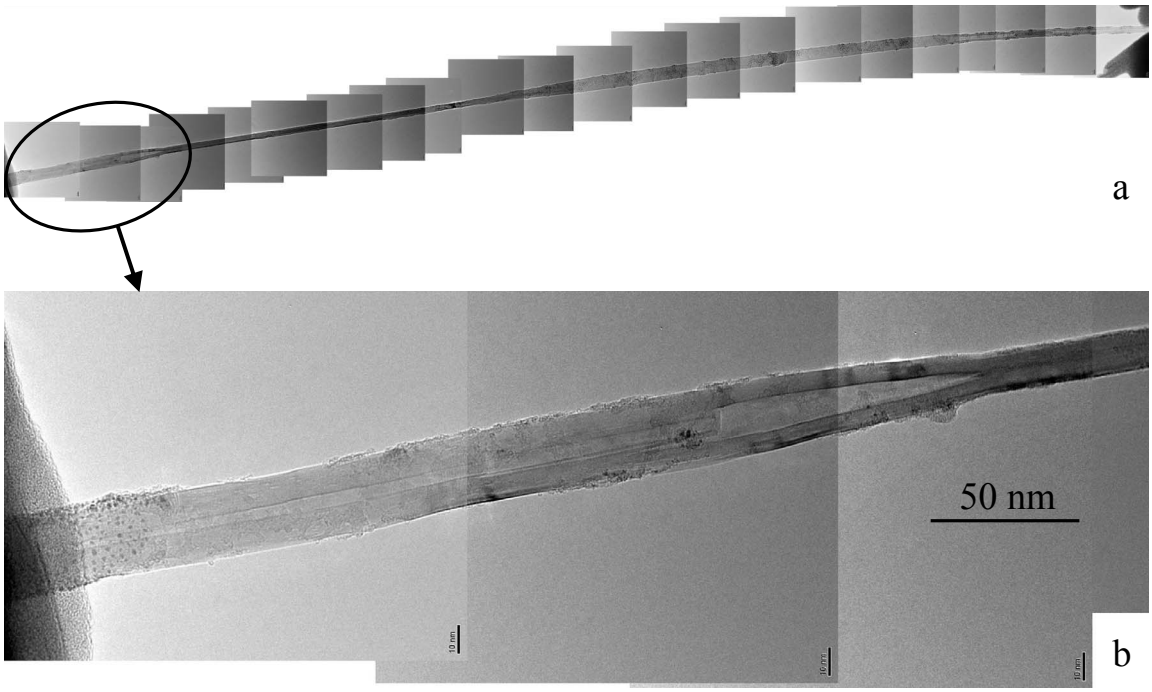

Figure 3.16: TEM image of BNNT mounted on a W tip through SEM nanomanipulation setup. (a) Overall composite image of the entire tube. (b) Enlargement of left hand section of the BNNT. The Pt used to cement the BNNT to the W tip can be seen on the left. The walls are visible and taper in the middle of the tube, making this a less than ideal nanotube for thermal conductivity measurements. Horizontal scale bar is 50 nm, while vertical scale bars are 10 nm.

nanotube could be pulled and would either be entirely removed from the razorblade or fractured from the competing forces of the razorblade and tip.

Not only did we now have a nanotube that could now be placed onto a device, but the nanotube could be fully characterized in TEM prior to placement on a device. This will allow us to correlate thermal behavior of a nanotube to the number of walls present without having to fabricate a device that is electron transparent and small enough to fit into a TEM. A recently obtained TEM image of a BNNT that was mounted on a tip is shown in Figure 3.16. While difficult and somewhat time consuming this method is worth the extra effort because of its ability to place individual tubes on prefabricated devices.

3.3 MWNT bearing creation

3.3.1 Introduction

Of course the key obstacle in creating a MWCNT motor is the alteration of an intact MWCNT to form a free rotational bearing. There are a variety of ways in which the outer walls of a MWCNT may be compromised to form a rotational bearing. Figure 3.17 shows some of the different ways in which we imagined the MWCNT could be altered to create the necessary rotational bearing. Of course this whole experiment presumes from previous theoretical and experimental work on linear bearings that the layered structure of MWCNT will also have a low energy barrier to rotational movement once the outer wall is compromised. In Figure 3.17a we see the representation of a MWCNT prior to any fracturing of the MWCNT. The MWCNT is contacted by two anchors at either end and a rotor plate attached to the outer wall of the MWCNT in the center. If one or several outer walls are fractured locally around the circumference of the MWCNT they may then be free to rotate along with the rotor plate attached, this is illustrated in Figure3.17b. In Figure 3.17c we show another possible method where many of the outer walls of the MWCNT have been removed from the regions between the rotor and anchors. By removing all of this material not only should the rotor be free to rotate, but also slide laterally along the length of the inner core of the MWCNT. One other possibility is that through fracturing the outer walls of the MWCNT in a wide variety of locations we may eventually break the outer walls along the entire circumference of the MWCNT on both sides of the rotor plate as illustrated in Figure 3.17d.

We explored a variety of methods to create the rotational bearing needed and achieved a wide variety of results, many of which appeared to match the conceptual models

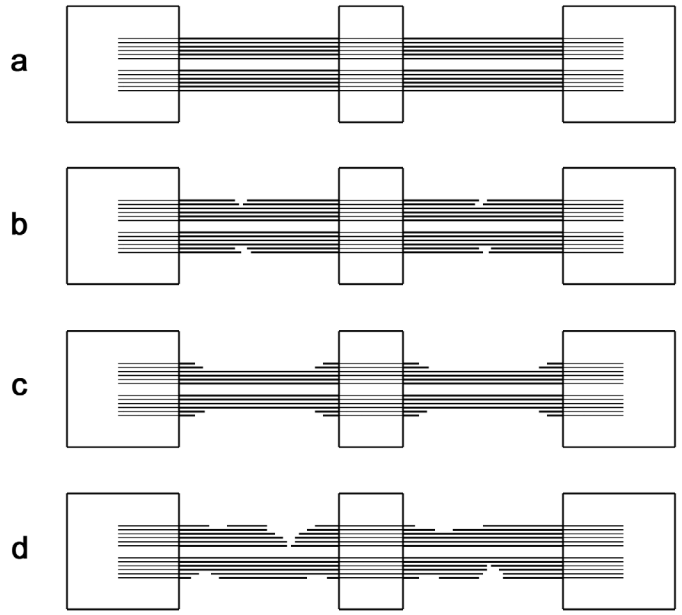

Figure 3.17: Conceptual visualization of a variety of ways in which the outer walls of a MWCNT contacted by two anchors and a rotor may be fractured to create a free rotational bearing.

shown in Figure 3.17. These methods are discussed in the next sections.

3.3.2 Mechanical Stress

We found that through large applied voltages it was possible to rotate the rotor plate of a MWCNT by a small degree. By applying large enough voltages we were able to twist the MWCNT presumably past its elastic limit. Through repeated torsional stresses exceeding the elastic limit a point the rotor plate became quite rotationally free, no longer requiring large voltages to rotate it, and being capable of full 360 degrees of movement. These results are discussed in more detail in the next chapter (see Section 4.2). While the exact method of failure is indeterminable until electron transparent devices are successfully fabricated, we presume that the fracture will somewhat resemble the model of Figure 3.17b. As the nanotube is pulled past its elastic limit the outer wall of the MWCNT fractures at points where the strain is concentrated. Through repeated stresses these fractures are

able to unzip around the entire circumference of the MWCNT, thus eventually creating a rotational bearing. Once the nanotube bearing is formed the lateral position along the axis of the nanotube is constricted by the remaining outer walls.

3.3.3 Reactive Ion Etching

To remove the outer walls fully in a manner similar to Figure 3.17 we attempted to use Reactive Ion Etching (RIE). RIE is a technique that is fairly common in the semiconductor industry. A plasma is formed of a reactive gas such as CHF_3, SF_6, or O_2 in a vacuum chamber. This plasma then is able to easily react with the substrate material and will preferentially remove certain materials. Since oxidation is a commonly used technique for nanotube purification we supposed that by using O_2 as our RIE gas we would be able to slowly remove the outer walls of the MWCNT. We hoped to be able to use this technique for a number of reasons. We had found that using mechanical stress to fracture nanotubes was only possible on thinner tubes (<20 nm), the voltages required to twist larger tubes past the elastic limit exceeded the breakdown strength of our SiO_2 layer. We hoped to form a more parallel process where all of the devices on a silicon chip could be rotationally free simultaneously. This would eliminate the time spent trying to rotationally free each device and would open up the possibility of using these bearings in mass fabricated devices. Finally we hoped by eliminating all of the outer walls we would be able to simultaneously demonstrate the linear and rotational bearing nature of one of our devices. This would more conclusively prove that we were exploiting a rotational bearing and help eliminate doubts that we had merely fractured the nanotube to form an extremely weak spring.

All of the etching was done in a Plasma-Therm PK-12 Parallel Plate Plasma Etcher for our RIE experiments. The samples were etched in O_2 plasmas at a pressure of 100 mTorr

and a power of 15 W for up to 40 seconds. After etching the samples were placed in the *in situ* measurement setup in the LEO 1550 SEM described in Section 4.1.2. We found that devices subjected to identical plasma treatment had their torsional strength weakened to varying degrees. Some devices even appeared to be free, requiring only low applied voltages for large angular displacements, and several times the rotors were already in the vertical position (rotated 90) when first loaded into the SEM. Meanwhile other devices subjected to identical plasma treatment, while weakened, still had appreciable torsional strength, and could only be slightly deflected with large applied voltages. We also found several devices where the rotor was either already stuck to the underlying substrate or would stick upon rotation. In these cases it appeared that the MWCNTs were slightly extended, allowing the rotor in its rest position to contact the surface or to contact it upon rotation. We have seen both from this and from other experiments that once a rotor has touched the surface it is very hard to overcome the van der Waals attraction and pull it out of contact. Unfortunately, the devices that appeared to be rotationally free were prone to failure, unlike the torsionally sheared devices of the previous section. After several rotations the MWCNT would snap somewhere along its length (see Figure 3.18).

We had supposed that because of the graphitic perfection of MWCNT that once a layer had begun to be oxidized it would be more preferential for oxidation to occur along the remaining dangling bonds rather than to begin oxidation of an inner intact layer. These assumptions agreed quite well with previous results in STM experiments where it was shown that when high quality highly oriented pyrolytic graphite (HOPG) substrates were oxidized the formation of monolayer etch holes was highly favored over multilayer etch pits[121]. From our experiments however, this did not appear to be the case. Upon careful examination of the literature we found that the mechanism of oxidation in a reactive oxygen

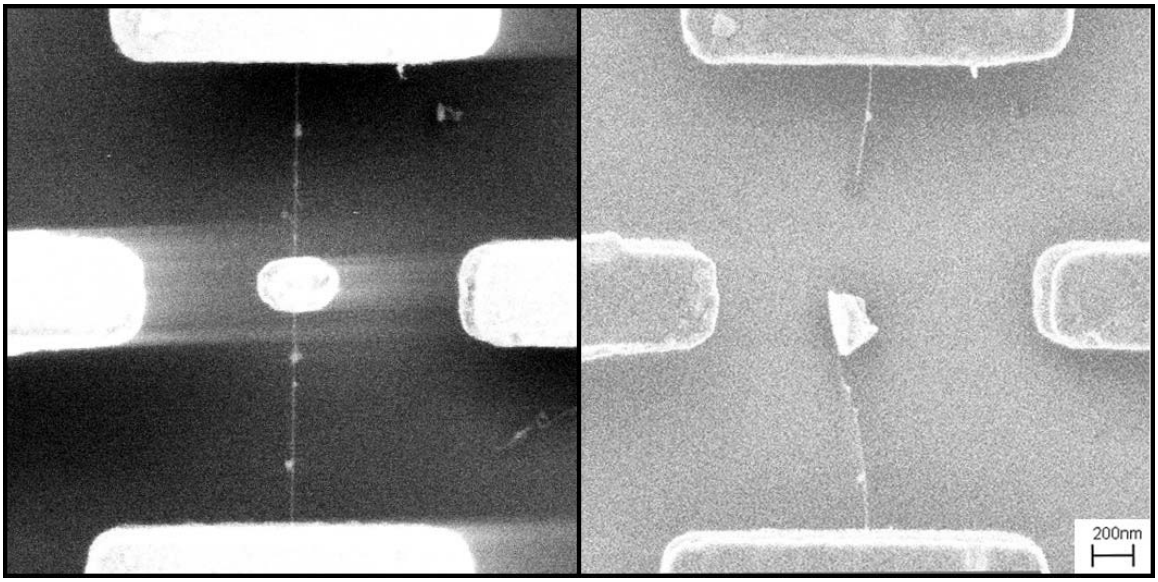

Figure 3.18: SEM image of MWCNT motor prior and subsequent to RIE. After RIE the torsional spring constant was reduced. Upon rotation, the nanotube fractured resulting in the image shown at the right.

plasma is very different from that of molecular oxygen. In glassy carbons it was found that an oxygen plasma is much more likely to create etch pits than molecular oxygen[122]. In subsequent experiments on HOPG it was also shown that an oxygen plasma formed many more etch pits than molecular oxygen[123]. These results can be better understood through a later experiment where 46 different carbons and coals were subjected to oxidation by both oxygen plasma and molecular oxygen. In this experiment it was found that plasma oxidation depended chiefly on exposed surface area and had little dependence on structural or chemical factors[124]. From these experiments and our results we felt we could safely conclude that rather than removing the walls layer by layer the oxygen plasma was actually creating etch pits in a manner similar to Figure 3.17d. While weakening the tube sufficient for it to twist as a torsional spring or even act as a rotational bearing, these etch pits induce too much of a structural flaw, causing these devices to quickly fail. While oxidation with molecular oxygen should be a more effective method to selectively remove the outer walls of

a MWCNT layer by layer without the formation of deep etch pits, this would be difficult to achieve because the electrical contacts would have to be compatible with a high temperature ($< 600°C$) oxidative atmosphere. The tendency of etch pits to form in MWCNT exposed to oxygen plasma appears to have been confirmed by some recent work on oxidation of MWCNT[125].

3.3.4 Electrically Driven Vaporization

After RIE failed to remove the entire outer wall of the MWCNT in the areas between the anchors and the rotor we began to explore the use of electrically driven vaporization (EDV). EDV as a method was first discovered by John Cumings and Phil Collins, members of our research group, while working on the *in situ* TEM linear bearing experiments[120]. They found that by applying a voltage pulse on the order of 3V to a nanotube that had been approached to a counter electrode through the TEM nanomanipulation setup, that the entire end cap of the nanotube would be removed. The amount of walls removed decreased along the length of the tube, leading to a tapering effect. Through repeated voltage pulses the nanotubes were "peeled and sharpened". This technique could be quite useful for forming sharp mechanically robust AFM tips and is currently being employed in our *in situ* manipulation experiments described previously (see 3.2.6) to form SPM tips and biological probes. In subsequent experiments by Phil Collins while at IBM with Phaedon Avouris he demonstrated that at large current densities the current through MWCNT would exhibit a stepwise decay which corresponded to a thinning of the MWCNT[126]. Each current step was believed to correspond to the removal of at least one of the outer walls of the MWCNT. Through controlling the amount of steps in a current decay the quantity of walls removed from the MWCNT could be controlled. We set out to duplicate

these current decays in hopes of using this technique to form nanotube rotational bearings.

To avoid wasting nanotube NEMS devices that we had already fabricated we made separate batches of simple MWCNT electronic devices to explore the relevant parameters in EDV. Devices were made using arc grown MWCNT synthesized by W.Q. Han and arc grown MWCNT synthesized by Lukeman Shih. In these early experiments we gradually ramped the voltage applied across a MWCNT while monitoring the current for extended periods of time at constant voltages. We found that while many nanotubes would experience a failure through a gradual decrease in current or sudden failure, in some devices we would see a stepwise current decay with step sizes of 10-20 μA, the same range of the steps Phil had witnessed. Some of these current decays are shown in Figure 3.19. Stepwise current decays were only seen in devices using MWCNT synthesized by Lukeman Shih. Upon TEM characterization we found that the nanotubes synthesized by Lukeman Shih were more graphitic in nature with far less defects. This was most likely due to the inclusion of small amounts of B in W.Q. Han's synthesis process to produce very long (>10 μm) MWCNT. We also found that current steps were more likely in devices of lower resistance (<25kΩ). By annealing our devices at 400°C for 1 hour in a tube furnace under flowing Ar we could reduce the contact resistance and current noise, and were able to achieve much cleaner breakdowns. Stepwise decays in the current were usually prefaced by a gradual current decay at constant voltage. We presume that this decay usually corresponded to the removal of the outer layer which because of various surface treatments, synthesis, and gas adsorption was less perfect than the inner walls.

Once we felt we somewhat understood the necessary characteristics for reliably achieving EDV we began to perform EDV on our NEMS devices. Through examining our devices via SEM at the various stage of EDV we were able to witness the thinning due to

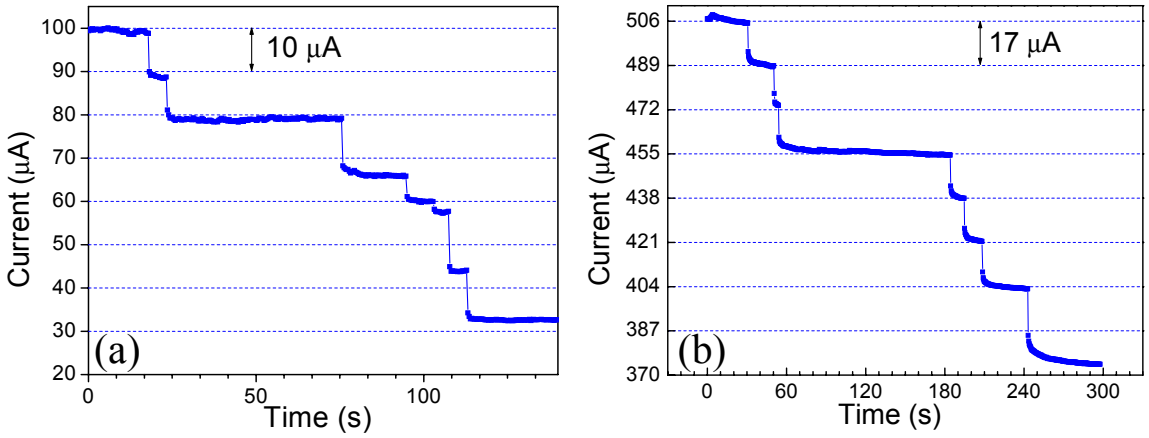

Figure 3.19: Current cascades in MWCNT at constant voltage. (a) A typical cascade is shown with step sizes of 10-20 μA. (b) In some devices the step size was quite regular as is shown here. The constant voltages applied during these two current cascades were 3.6 V and 4.2 V respectively.

EDV. We found that all of the thinning that we were able to witness would occur on one side of the rotor. We could take a device all the way to failure on one side without seeing any thinning or torsional weakening on the other. This was most likely because once the current cascade had initiated on one side, that side had a higher resistance and thus a higher concentration of the voltage drop, and would experience all the remaining current cascade. These experiments demonstrated the need to be able to distinctly apply voltage on each of the exposed sections of the MWCNT. In order to do this it was essential to establish a temporary electrical contact to the rotor plate. While it could be possible to establish this contact through approaching the rotor plate with an AFM tip, this approach would be arduous and time consuming. Instead an extra lithography step was introduced in which a temporary electrical contact would be patterned connecting the surrounding stators and the rotor. Once this electrical short between the stator and rotor had been established current could flow directly through the nanotube from either side of the rotor allowing EDV to occur in both sections. The temporary contact would then be removed prior to suspension of the MWCNT.

Two metals presented themselves as ideal for this contact, Al and Ti. Both of these metals were known to etch rapidly in HF. By etching rapidly in HF these temporary contacts could be eliminated simultaneously with the suspension of the nanotube and rotor and would avoid the need to add any more chemical processing. While both of these metals are routinely used in semiconductor processing, we favored the use of Al for the shorting layer as it is easily evaporated from a tungsten boat in a thermal evaporator, whereas Ti evaporation requires the use of an e-beam evaporator. Our first attempts at shorting mock stators yielded extremely high resistances. Through careful experimentation we found that two factors contributed to this. First in our low temperature anneals of gold contacts to obtain low noise/resistance devices a surface layer of chromium oxide was forming. This was possible because of a eutectic in the Cr-Au system at 400°C. This surface oxide is extremely thin and presented little problem for contacting with a probe station or wire bonder where it is easily pierced mechanically. However this layer remains unbroken when the Al or Ti shorting layers were deposited, causing the stator-rotor resistance to be quite high. To eliminate this effect a much thinner Cr adhesion layer of 1.1 nm was used (good adhesion results were obtained down to 0.6 nm) and all annealing was performed on a Heatpulse 210T rapid thermal annealing system under a flowing Ar atmosphere. All of the anneals had a 30 second ramp with a 5 minute soak at the anneal temperature. We found that the optimum temperature for annealing was between 650°C and 800°C with increasing damage to the contacts occurring at higher temperatures. For these devices a 700°C anneal was used to insure good electrical contact without compromising the leads.

We found that even on pure gold contacts Al shorts would have high resistances while Ti shorts would not. This was most likely due to oxidation of the Al. Both Al and Ti are known to oxidize easily. We had hoped this would not be an issue because of their

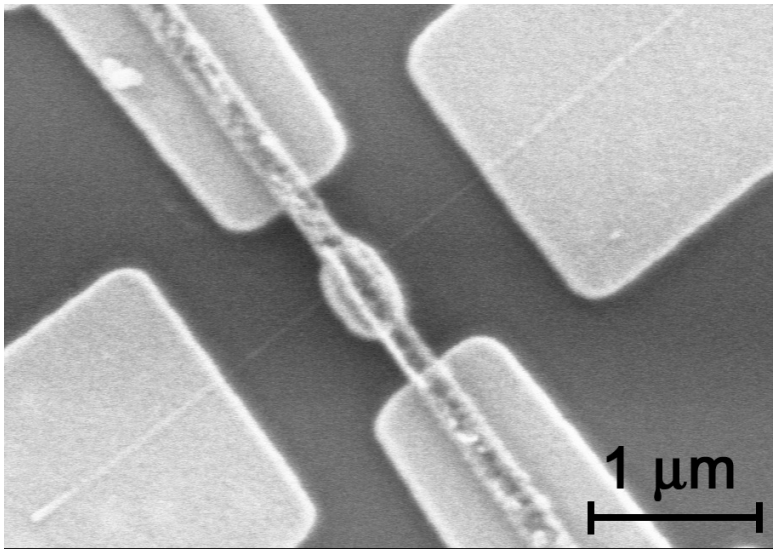

Figure 3.20: Ti short connecting the stators and rotor of a MWCNT NEMS device.

tendency to form a self passivating layer of oxide. Fortunately, Ti made excellent contact and became our metal of choice for these experiments. Xiao Fan Meng of the microlab performed most of the Ti depositions in his personal system as the Ultek e-beam evaporator was out of service for a prolonged period of time and the Edwards e-beam evaporator was not yet functional. One of these shorts is shown in Figure 3.20. All anneals were performed prior to Ti deposition. If performed after the Ti would oxidize during the anneal, eliminating the good electrical contact between the stators and rotor.

Once we had obtained devices which had been annealed with RTA and were shorted with a Ti shorting layer between the two stators and rotor we were then able to perform EDV of the MWCNT on either side of the rotor. To rotationally free the rotor we proposed to obtain 2-3 good current steps after the initial current decay. It proved difficult, however, to induce equal amounts of damage on both sides; the resistance was rarely the same on both sides, often requiring different voltages and currents to begin the current cascades, and sometimes the nanotubes would completely fail without showing any steps at all. When they did occur, the cascades were sometimes difficult to controllably stop. Upon testing the

devices *in situ* in an SEM, we found that many would have significantly reduced torsional spring constants. They would not, however, exhibit free bearing behavior - they would eventually break without showing the freedom of motion seen in the torsionally freed devices. We concluded that one side of the tube had been rotationally freed while the other remained as a torsional spring.

Despite these difficulties we were able to shed more light on the bearing nature of our devices. We repeatedly saw one particularly interesting failure mode. Instead of snapping at some point along its length as was seen with the RIE devices of the previous section, the MWCNT would telescope out, dropping the rotor to the underlying surface. The result of one such failure is shown in Figure 3.21. The linear extension of the MWCNT is quite clear in this figure with the length of the final tube far exceeding that of the original. These results were able to demonstrate that it was possible to remove enough of the outer walls to create a linear bearing with our devices. Unfortunately it was difficult to reliably control so that equal numbers of walls were removed from both sides of the rotor paddle. If too many walls were removed the nanotube was more likely to telescope than to support rotational movement as an axle. Hopefully as we delve further into this technique by performing EDV on electron transparent membranes for TEM we will gain a greater understanding of the variables at play in EDV and a better ability to use it for the creation of free rotational and linear bearings.

3.3.5 Electron Beam Cutting

In our first experiments with motor devices rotationally freed through mechanically stressing the MWCNT past the elastic limit we found that the failure rate of devices seemed to correlate directly to the aperture used in imaging with the LEO 1550 SEM. For the LEO

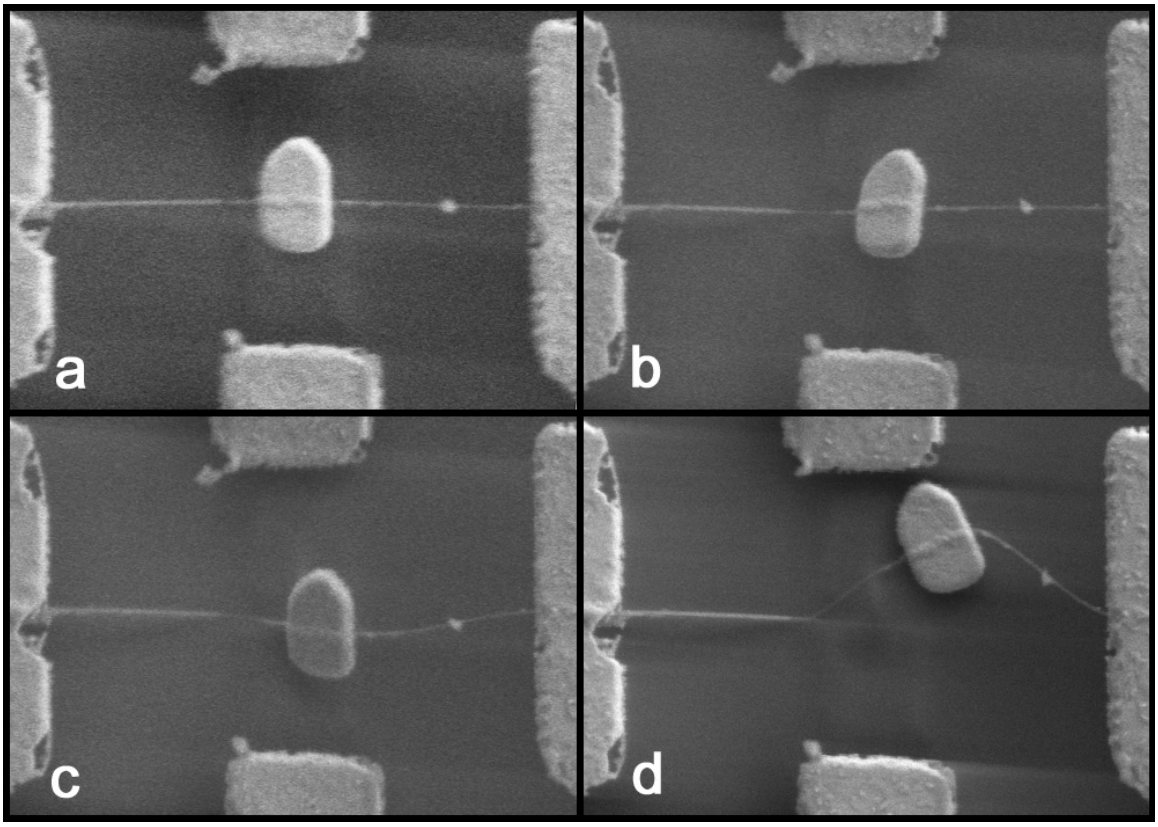

Figure 3.21: Telescopic failure of a MWCNT that has undergone EDV on both sides of the rotor paddle. The images are in sequential order, showing increasing extension: (a) No voltages applied. (b) Rotor pulled down towards substrate (voltage applied to back gate). (c) Rotor pulled towards lower stator. (d) Rotor pulled towards upper stator (though hard to see, the nanotube is still continuous).

SEM the aperture used corresponds directly to the probe current imaging the sample. To investigate the possibility that high probe currents could damage the MWCNT and lead to a higher failure rate MWCNT devices where the nanotube had already been fractured were exposed to large beam currents. By using a line scan at a high magnification it was possible to cut MWCNTs. The ability of the beam to cut through the MWCNT appeared to be best at low acceleration voltages and large probe currents. Figure 3.22 shows one of these devices prior and subsequent to a line scan where the nanotube was cut.

Once we had concluded that exposure to high currents of low acceleration voltage electron beams could cause damage to MWCNT we took great care with our rotor devices

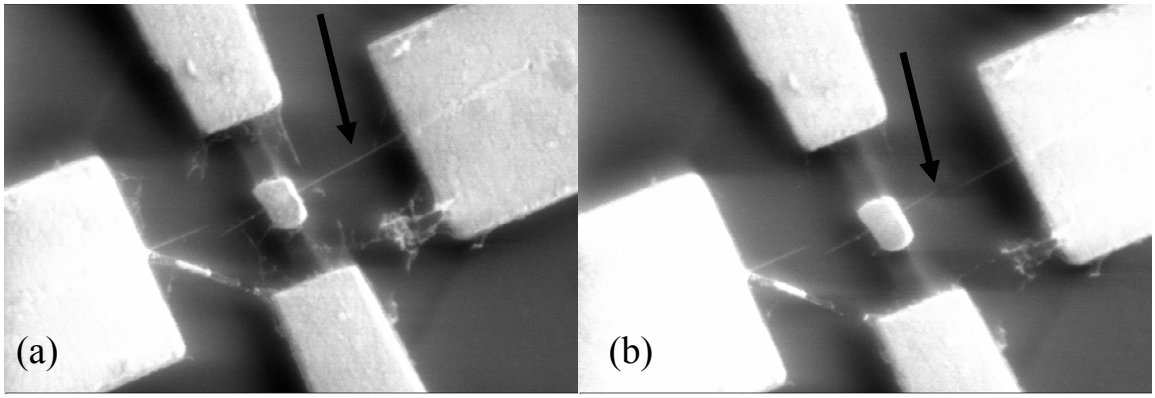

Figure 3.22: Suspended MWCNT device (a) prior and (b) subsequent to exposure to a prolonged line scan by a low energy electron beam. The arrow indicates the area that was exposed to and cut by the electron beam.

to minimize total exposure so as to maximize their lifetime. We also began to use this technique to selectively damage the surrounding nanotube. The MWCNT was exposed to line or area doses of a 1 keV electron beam at the maximum current and magnification possible while a torsional strain was exerted through applied voltages to the back gate stator. These exposures helped accelerate the fracture of the rotor devices to form loose torsional springs or free rotational devices. However our lack of understanding of the mechanism behind the cutting phenomena made it difficult to determine the proper exposure levels. With better understanding of the damage mechanism we hoped to be better able to control the damage to the nanotube.

High energy electron beams had been used previously to cut nanotubes through knock-on damage. In these experiments it was found that the threshold energy required for knock-on damage to occur was >86 keV[127]. Obviously with electron beam energies of $\sim$ 1 keV the mechanism for the cutting that we were observing was quite different. Using our recently purchased SEM we were able to investigate the cause of this beam cutting. For this investigation arc grown MWCNT were dispersed in either ODCB or IPA (no dependence upon the particular solvent used was seen) and deposited onto TEM index grids coated

with lacey carbon purchased from Structure Probe Inc. TEM images were taken before and after cutting in our JEOL 2010 TEM using an acceleration voltage of 100 keV. Once the samples had been imaged in the TEM they were then loaded for cutting into our FEI XL-30 Sirion SEM. By using our own SEM it was possible to have the long sessions, high quality vacuum, and variety of atmospheres required to investigate this effect. During cutting, the SEM was operated in line scan mode at maximum magnification ($10^6\times$), with the nanotube axis perpendicular to the scan line. Several different gasses were introduced through a leak valve, and partial gas pressures were measured with a Stanford Research Systems SRS200 residual gas analyzer. Absolute pressure was measured using a Bayard-Alpert ion gauge and a Terranova 934 controller programmed with the appropriate gas constants.

We were able to cut through nanotubes at a variety of acceleration voltages, beam currents, and gas pressures within the microscope chamber. The cuts were seen as a gradual decrease in height and width of the nanotube line scan profile, and the decrease accelerated as the cut neared completion. We could interrupt any cut by blanking the beam or switching the microscope out of line scan mode. If the nanotube was suspended, as on a TEM grid, a sufficiently damaged region would often act as a loose hinge, with the nanotube swinging around under the charging influence of the electron beam. We have also been able to make oblique cuts by rotating the scan line relative to the nanotube. Figure 3.23 shows a nanotube on a TEM grid before and after cutting. Figure 3.23a shows the uncut nanotube suspended across a gap. The turbulent deposition method displaced the ends of the nanotube perpendicular to its longitudinal axis, subjecting it to a shear strain which was maintained by contact with the grid and other deposited material. This shear strain was released when the nanotube was cut, and the two sections of the nanotube straightened out, as seen in Figure 3.23b. Figure 3.23c is a close-up image of a section of the pristine nanotube

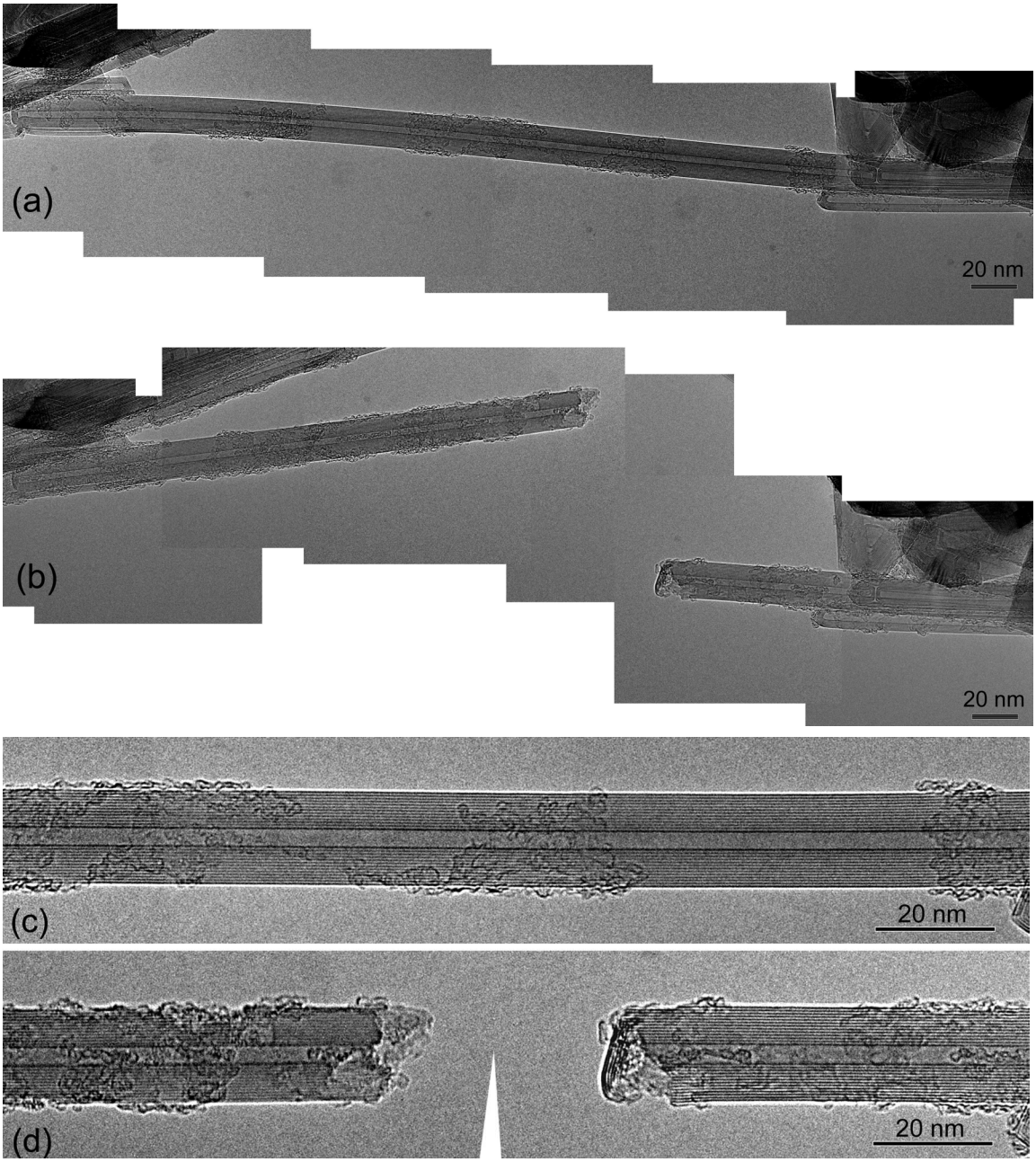

Figure 3.23: Composite TEM micrographs of (a) a nanotube in its pristine state suspended on a TEM grid and (b) the same nanotube after cutting. (c) A close-up image of the same nanotube and (d) the cut segments of the nanotube are shown. The image in (d) has been rotated and aligned to vertically correspond with the same sections in (c). The scale bars are 20 nm.

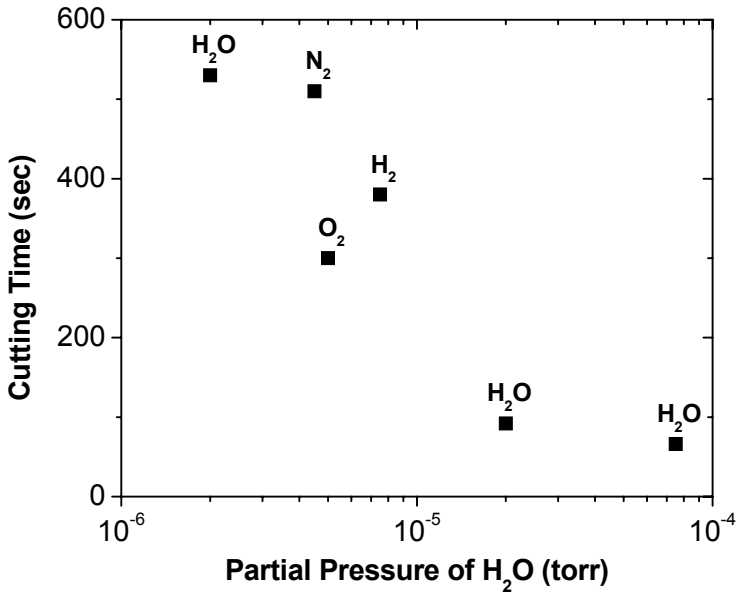

Figure 3.24: Cutting times for multiple cuts on a single nanotube in different atmospheres. The partial pressure of water is shown on the horizontal axis, while the majority gas is shown above the data points. The total pressure was 7.5×10^{-5} Torr during the N_2, O_2 and H_2 trials.

before cutting. Figure 3.23d shows the same section after cutting, with the two cut sections rotated and aligned to vertically correspond with Figure 3.23c. A comparison of these last two images shows that the cut removed approximately 40 nm of material. Furthermore, the damage induced by the electron beam was confined to the immediate region of the cut, with equal damage done to each subsequent layer of the multiwall nanotube.

The most important factor affecting the cutting speed was the presence of water vapor within the chamber. Figure 3.24 shows the results of cutting through a single nanotube at several points along its length in different atmospheres, with an acceleration voltage of 1 keV and a beam current of 118pA. At total pressures below 2×10^{-6} Torr, where most of the residual pressure was due to water vapor, nanotubes could be exposed to the beam for over 10 minutes and still not be visibly damaged. Bleeding in nitrogen to a pressure of 7.5×10^{-5} Torr did not significantly affect the cutting time. Bleeding in

hydrogen at the same pressure resulted in slightly faster cuts, but this may be due to a higher partial pressure of water (our hydrogen source contained a partial pressure of water over 50% higher than in the other gasses). Oxygen consistently increased cutting speed up to twice as fast. Water, at the same pressure, would increase the cutting speed even more, up to ten times as fast. Electron beam induced mass loss is a well known effect in electron microscopy of biological samples[104]. Studies have found that a common source of mass loss is caused by the presence of water[128, 129]. Radiolysis of water molecules is the driving force behind this etching mechanism[130] : highly reactive OH·, H·, and HO_2· radicals can react with carbon atoms to form CO, CO_2, various hydrocarbons and hydrogen gas, leading to mass loss of the original carbonaceous specimen (and similar reactions can be expected when oxygen molecules are ionized in the vicinity of the sample). We propose that this etching mechanism is responsible for damaging the nanotubes.

Interestingly, we found that bundles of nanotubes would consistently be cut faster than individual nanotubes, despite the greater amount of material that must be removed. Theoretical calculations of water adsorption on the outside of nanotube bundles have shown, however, that water molecules will be adsorbed first into the groove between two nanotubes and only at higher densities will they then be adsorbed onto the entire nanotube surface[131]. This suggests that bundles will adsorb more water at a given pressure than individual nanotubes. Since the presence of water greatly accelerates cutting, we can therefore expect nanotube bundles to be easier to cut.

Two-contact electrical transport while cutting shows a steady increase in the resistance of the nanotube during the cut, with no steps or jumps showing opening or closing of discrete conductance channels. We did find, however, that by passing current through the nanotube during a cut we could reduce the damage done to the nanotube and greatly

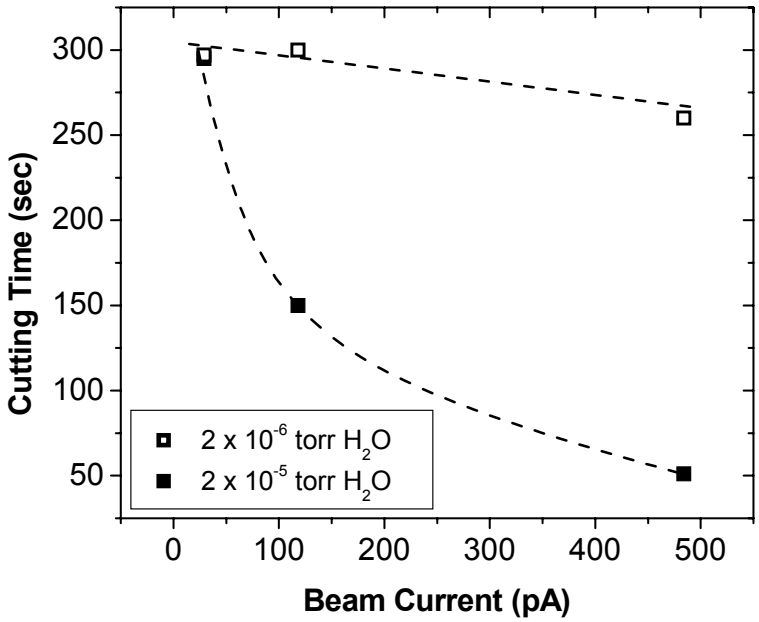

Figure 3.25: Cutting times for multiple cuts on two nanotubes in different atmospheres at different beam currents. In both cases the majority gas was water vapor. The dashed lines are guides for the eye.

increase its lifetime under the beam. For example, putting 1.7V across a nanotube with an initial resistance of 15kΩ would decrease the cutting rate by a factor of 4 (this cut took 20 minutes, while two separate cuts on the same nanotube with no voltage applied took 5 minutes each). Resistive heating of the nanotube may reduce the damage through two possible mechanisms. It has been shown that raising the temperature of nanotubes to over 300C reduces knock-on damage by annealing out defects via the increased mobility of interstitial atoms[132]. Also, by increasing the temperature of the nanotube we decrease the sticking coefficient of water molecules impinging on the surface, thus limiting the number of molecules present to aid in the cut.

Figure 3.25 shows the results of cutting two nanotubes exposed to different partial pressures of water at various beam currents. At a higher partial pressure, increasing the beam current speeds up the cutting process. This is simply the consequence of adding more energy to the system, thus increasing the rate of the chemical reaction. At low water vapor

pressure (2×10^{-6} Torr), however, this effect was greatly suppressed, and even high beam currents ($\sim$ 500 pA) would not significantly increase cutting speed. Therefore we propose that at low pressures the rate is limited by the amount of water present rather than the amount of energy supplied by the electron beam. Figure 3.26a shows cutting times for multiple cuts on several nanotubes at different acceleration voltages. Contrary to nave expectation, increasing the acceleration voltage of the electron beam increases the cutting time. This effect is due to the cross section for the ionization of a water molecule decreasing as the incoming electrons become more energetic. Schutten *et al* have measured the total ionization cross section for water for this range of electron energies[133]. A normalized plot made by rescaling the cutting times of different nanotubes to match at common acceleration voltages is shown in Figure 3.26b, together with a plot of the inverse of the total ionization cross section.

From our results it is evident that precautions must be taken during all SEM/nanotube experiments to limit beam-induced damage. We have also been able to damage and cut inorganic nanostructures (BNNT), extending this caveat to SEM work on all sensitive nanomaterials. With our increased understanding of the mechanism behind electron beam cutting this technique should be more easily applied to the rotational freeing of the rotor devices. We have also been able to use this technique to simply cut through nanotubes. There are a number of situations where this has been useful. As mentioned previously, nanotubes attached to SPM probes were cut to free the nanotube from bulk material or a razor blade. We have also used this technique to remove shorts formed by nanotubes and photoresist residue. While other methods to cut nanotubes *in situ* in SPM[134, 135] or TEM[136, 137] exist, the ease and usefulness of electron beam cutting far exceeds these previous methods.

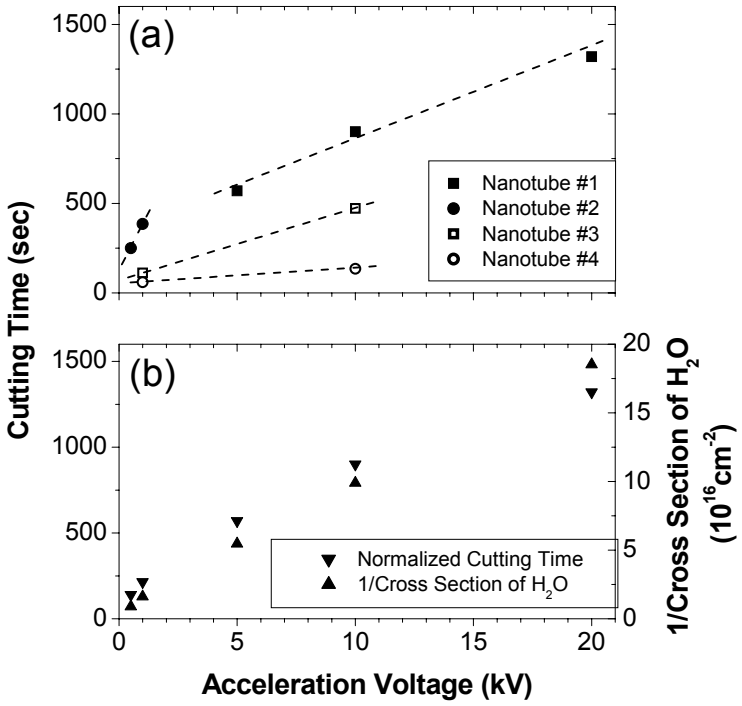

Figure 3.26: Cutting time vs. acceleration voltage. (a) Cutting times for multiple cuts on several nanotubes at different electron beam energies. The dashed lines are guides for the eye. (b) Normalized cutting data from three nanotubes at different electron beam energies. The inverse of the total ionization cross section for water molecules as a function of electron energy is also plotted, and follows the same trend.

Chapter 4

Nanomotor Operation

4.1 Experimental Setup

4.1.1 Sample Mounting and ESD

Using the methods outlined in Section 3.1.2 Tom Yuzvinsky and I fabricated MWCNT motor devices. To place these devices into an SEM for *in situ* deflection experiments, the solid substrates were mounted on 16 pin DIP or 28 pin PLCC ceramic chip carriers. Ag paint served as a mechanical and electrical contact to the backside of the Si chip and thus the back gate stator. Electrical contact to the nanomotor anchors and side stators was established by bonding 0.00125-inch Al-1%Si wire to the bonding pads using a West Bond 7400B Ultrasonic Wedge Bonder. We soon found that bonding caused the highest rate of failure of our devices. While difficult to determine the exact cause of failure it was presumed to be electrostatic discharge (ESD). To limit the failure rate induced by the bonding step the bonding pads of each set of anchor electrodes were electrically shorted in the EBL step. This prevented any stray current from passing through the nanotube during the bonding step. For the first set of devices where the focus was on torsional strain and

failure through passing the elastic limit it was acceptable to short these electrodes since no electrical transport was being performed on the MWCNT.

For MWCNT nanomotors to be freed by EDV it wasn't possible to fabricate shorted anchor electrodes because this would make the nanotube completely inaccessible for EDV. In the first attempts to contact unshorted devices with a good amount of ESD precautions the failure rate was even larger than the previous devices. It was clear that a method of shorting the anchor electrodes after EDV and prior to bonding was needed. A pattern of wires extending from the bonding pads to a common point was added to the EBL designs. After EDV and the BOE etch had been performed these wires could be shorted by placing a small drop of dilute Ag paint using the wire bonders manipulation arm. This shorting step helped greatly reduce the amount of devices lost during wire bonding. The Ag paint shorts had the added advantage that they could easily be removed after bonding using a probe station manipulator for any further transport measurements.

The true source of these ESD problems was difficult to determine. Whether the MWCNT devices were more susceptible to ESD because of EDV, chemical etching, suspension above the substrate or variability of an old wire bonder is unclear. However it was clear after many failed attempts a full set of ESD precautions needed to be consistently used. While these precautions may seem gratuitous, the severity of the problem dictates the use of an abundance of caution. For wire bonding both the bonding head and platform are shorted to the bonder chassis through alligator clips. Chip carriers are mounted in carbon foam carrying packs during bonding to ensure grounding and eliminate ESD that may have been occurring during the cutting of shorted DIP leads or the transfer of devices from the bonding stage to carbon foam carrying packs. In addition an extra lithography step has been introduced where a layer of Au is patterned, shorting all of the bonding pads.

For devices where bonding pads and leads have already been established through optical lithography, the Cr/Au lithography step can be forgone since no adhesion layer is needed for the short electrodes connecting the nanotubes to the bonding pad leads. This not only has the advantage of requiring one lithography step instead of two, but also helps establish better contact to the MWCNT. After the device has been fully contacted via wire bonding, the shorting wires are scratched via a probe station manipulator. The lack of a Cr adhesion layer allows the probes to easily sever the electrical shorts.

Transferring devices into the SEM for *in situ* measurements also requires a great deal of ESD precautions. Each BNC connector on the breakout box is equipped with a three position switch. This allows each pin of the chip socket to either be connected to the inner conductor of the BNC, floating, or grounded to the BNC shield. When placing a chip carrier into the socket, all of the pins are grounded using the BNC switches. The carbon foam of the carrying case, tweezers, and person handling the device are also all grounded using alligator clip leads and grounding straps. With this complete grounding protocol in place few devices are lost in the process of transferring.

4.1.2 SEM Observation

To observe the movement of a mounted MWCNT *in situ* in an SEM it was essential to be able to load an electrically connected device in a reasonable amount of time and be able to capture images of its movement. The first *in situ* SEM experiments were performed on a JEOL JSM6340F field emission SEM (FESEM) located at the the National Center for Electron Microscopy (NCEM). This microscope had the advantage that it was commonly used by our group for imaging and NCEM was flexible enough to allow an electrical feedthrough to be placed on the instrument for *in situ* experiments. A 16 pin DIP Socket

mounted on an Al sample puck was connected to the electrical feedthrough using Be-Cu crimp/solder spring-style connectors. While this setup allowed the first *in situ* nanomotor experiments to take place, the time required to transfer in a sample was excessively long (>6 hours) due to the fact that this diffusion pumped system was not equipped to quickly pump down after a complete vent to air. Additionally it was quite difficult to obtain time on the machine because of the small amount of time slots available per day.

To overcome the difficulties associated with the SEM at NCEM we began to use a LEO 1550 FESEM administered by the microlab. This microscope had the advantage of being fairly easy to reserve for long sessions, achieved superior resolution at low acceleration voltages, was already fitted with two 25 pin type-D electrical feedthroughs, and typically pumped down after a complete vent to air via a turbopump in less than 15 minutes. A 16 pin ZIF (zero insertion force) socket was mounted on an Al sample stud to allow for easier mounting of the chip carriers. A series of four 4 pin Molex power connectors were used to connect the chip socket to the 25 pin feedthrough. This setup was a great improvement, with a combined mounting/pumpdown time on average of one hour, many samples could be viewed in a single session. In this setup the first deflection of a MWCNT nanomotor device was observed. This deflection was captured through static images of the rotor in various positions. It was quickly apparent that for further experiments it was desirable to be able to capture live video of the deflection of the rotor. This would greatly speed the experiments by being able to forgo the time consuming process of capturing and naming images and would allow the capture of any AC movement of the rotor.

The ideal method of video capture would be to capture an AVI of each successive frame at the raster rate of the SEM beam. This would prevent any loss of information in the video capture process. Unfortunately no SEMs are set up for this type of video

capture. A likely alternative of finding software to capture the monitor output at the VGA refresh rate proved quite difficult. The best method we were able to employ to record the live SEM signal was to use a VGA-to-TV converter. While this worked well it did have two disadvantages; pixels are lost when the image is downsampled to TV resolution and the frame rate is lowered to 29.97 frames per second. On the LEO 1550 FESEM all video conversion was done using an Avermedia Averkey 500 Pro VGA-to-TV converter. The S-Video signal was recorded using a Sony DCR-TRV350 camcorder which allowed the S-Video signal to be captured at a quality higher than VHS and easily transferred to computer via a firewire output. This setup was eventually replaced with a Panasonic DMR-HS2 DVD recorder when this became commercially available. This recorder could capture a high quality S-Video signal directly to a hard drive or DVD. DVD is obviously a medium of choice for its quality, ease of computer transfer, and ability to scroll through quickly in search of the section of interest. Relevant data such as the name of the device or applied voltages could be captured directly onto the video recording through SEM comment boxes. This documentation method was eventually replaced by direct recording of most comments onto the audio channel as this allowed more detail to be recorded in less time.

When the *in situ* measurement setup was transferred to our FEI XL-30 Sirion FESEM some further improvements were made on the measurement setup. Because of outgassing problems with the ZIF socket a 16pin DIP socket was made using vespel and Samtec pins, a commercial 28pin PLCC socket was also added for larger substrate devices. In this microscope the pumpdown time for the measurement setup was now less than 15 minutes. Molex connectors were replaced with two HR-10 12-pin connectors which held more pins and required less force for insertion and removal. These connectors were already used in the JEOL AFM system so their vacuum compatibility was known to be good. It is

worth noting that the Omnetics plastic circular connectors currently used for the attocube system are also quite convenient for vacuum use. A text overlay system (Decade Engineering XBOB) was added so that all relevant voltages and currents could be recorded directly on to the video image. Two other video converters were purchased (CORIOgen Eclipse CS-460 and Grandtec MagicView GMV-4500) in hopes of overcoming the resolution loss caused by the VGA-to-TV conversion. By converting a zoomed in area the resolution loss in VGA-to-TV conversion can be overcome. These units not only had promising zoom features, but were also capable of video overlay which would provide an overlay alternative if the XBOB system caused resolution to degrade in the overlay. Currently the setup of choice is to use the CORIOgen CS-460 with the XBOB performing the text overlay onto the signal from the CORIOgen. An audio channel is still acquired for relevant information not recorded by the text overlay system. All video is recorded with a Sony RDR-GX7 DVD Recorder. In the future as *in situ* SEM video capture becomes more commonplace and as HDTV technology matures, better resolution should be possible.

4.2 Static Deflections

The first experiments performed on suspended MWCNT motor devices mounted in the SEM were on static deflection of the rotor paddle. By applying a large voltage to the anchor electrodes we supposed that it would be possible create a large enough attraction to cause the rotor paddle to rotate. The energy of a parallel plate capacitor can be written as $U = \frac{1}{2}CV^2 = \frac{1}{2}\frac{\epsilon A}{x}V^2$. Thus if we calculate the force, $F = \frac{\partial U}{\partial x} = -\frac{1}{2}\frac{\epsilon A}{x^2}V^2$, we see that it will be attractive and scale as $\frac{1}{x^2}$ in distance and as V^2 in voltage. Any anisotropy in size or centering of the rotor paddle should lead to non-equalized attractive forces, resulting in slight deflection of the rotor paddle. Displacement of the paddle will lead to an increasing

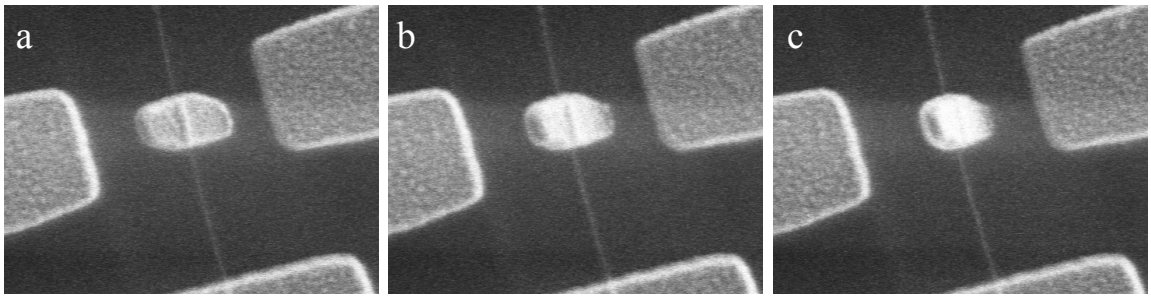

Figure 4.1: SEM images of static deflection of a MWCNT motor device through application of large electrostatic fields to the anchor electrode.

force on the more proximate side of the paddle and thus an increasing torsional strain. The force that the paddle experiences increases rapidly with the applied voltage and proximity to the substrate.

Using a Keithly 2400 Sourcemeter and Labview code writen by Chris Regan a voltage was gradually applied to the back gate stator while maintaining the stators at ground. Voltages of up to 100 V could be applied to the back gate stator, although typically voltages in excess of 85 V were not applied because of the danger of electrical breakdown. A current limit of 0.1 μA was used to mitigate any damage that would occur during electrical breakdown.

One of the first devices to be deflected through these applied voltages is shown in Figure 4.1. Through careful analysis of the rotor width in the SEM images the angular deflection vs. applied voltage could be obtained. Using commercial finite element analysis (FEA) software (FEMLAB 2.2) the electric field throughout the system can be calculated based on the voltage applied to the anchors and the rotational position of the rotor. The energy density of the electric field,$u = \frac{1}{2}\epsilon E^2$, can be integrated to give the total electrostatic energy of the system, $U = \int u dV$. A plot of the absolute value of the calculated electric field surrounding the rotor at two voltages and rotor positions is shown in Figure 4.2. By examining the change in electrostatic energy vs. angular position at each applied voltage

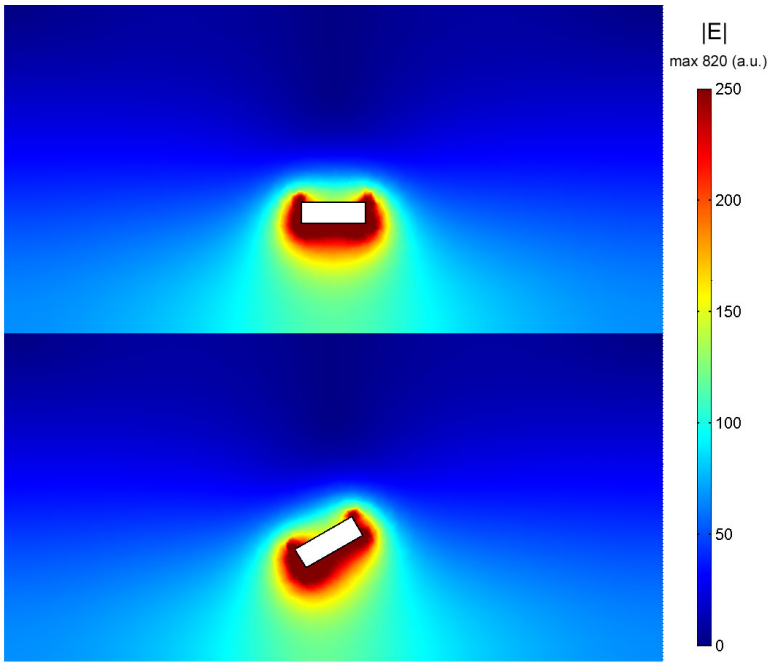

Figure 4.2: Plot of the absolute electric field surrounding the rotor plate in a MWCNT motor at two angular orientations as calculated through FEA.

a mean value of the torque applied to the system can be extracted, $\frac{\triangle U}{\triangle \theta} = -\bar{\tau}$. This mean torque can then be used to calculate the average torsional spring constant, $\frac{\triangle \bar{\tau}}{\triangle \theta} = -\bar{\kappa}$. The spring constants that were obtained using this method for our devices were 10^{-12} to 10^{-15} N·m which is within the range of torsional spring constants obtained by Williams *et al* in AFM experiments on MWCNT[85]. This large range of spring constants was primarily due to the different diameters of MWCNT that were used in these experiments.

Using a continuum mechanics model the effective shear modulus of the MWCNT can be estimated. A MWCNT is clearly different from a bulk cylinder with a finite determinable thickness, however obtaining a shear modulus at least provides a good framework for comparing MWCNT to bulk materials. The formula for the spring constant of a doubly clamped cylinder[138] is,

$$\kappa = \frac{2\pi(r_{out}^4 - r_{in}^4)G}{l} \tag{4.1}$$

where r_{out} and r_{in} are the outer and inner radius of the MWCNT, G is the shear modulus, and l is the length of exposed tube between the two anchors. It should be noted that the formula used by Williams *et al*[85] was for a singly clamped cylinder and was thus incorrect by a factor of four. Assuming a loose coupling between walls, a majority of the strain will occur in the outer wall whose thickness can be approximated as the inter-shell spacing (3.4 Å), thus $r_{out} - r_{in} = 3.4$ Å. The shear moduli calculated from our results were 100 to 300 GPa which was within the range that Williams *et al* should have obtained.

There are a number of factors that introduce uncertainty into these results. The shear modulus obtained is highly dependent upon the radius because $G \propto \frac{1}{r^4}$. Ideally the radius of the nanotube would be extracted from AFM images obtained prior to fabrication of the MWCNT motor device. However this was not done due to the time consuming nature of obtaining these images. The radius of the nanotube was extracted by examining the MWCNT in the SEM, which is not as accurate as AFM or TEM. This small uncertainty in radius introduces a large uncertainty in shear modulus because of the dependence of G on radius. The other major source of uncertainty in the modelling of these experiments was the charging influence of the electron beam. All of the FEA assumed that the only source of electrostatic potential was the voltages applied to the stator electrodes. It is clear that a constant current of electrons will cause surface charging to occur which will modify the electrostatic fields. Nonetheless these methods proved adequate for order of magnitude estimates of the torsional spring constant and shear modulus of the MWCNT used in these experiments.

Once it was possible to reliably torque devices, we began to explore how repeated torsional stress and high angular deflection affected these devices. With repeated low angle deflections little change was seen in the behavior of MWCNT motor devices. however for

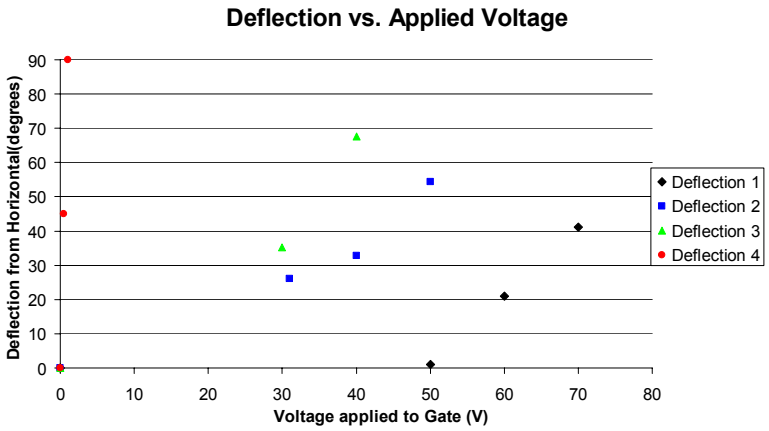

Figure 4.3: Plot of the angular deflection of the rotor plate in a MWCNT device vs. voltage applied to the back gate stator. The deflections (1, 2, 3,& 4) are chronological in order, though not sequential. As these deflections were repeated the nanotube weakened, until eventually the device reached a point where it required very little voltage for movement and appeared to be rotationally free (Deflection 4).

devices where it was possible to deflect the rotor over large amplitudes, the behavior was seen to alter. With each repetition the rotor would deflect further with the same applied voltage. As the torsional rigidity of the MWCNT continued to weaken it could be deflected 90° with less applied voltage each cycle. When applied voltages were removed the rotor would return to its equilibrium position, which gradually moved farther away from horizontal. To place the rotor in a horizontal position a voltage had to be introduced on the side stators to attract the rotor to the horizontal position. With repeated 90° rotation of the rotor the torsional stiffness of the MWCNT would suddenly weaken to the point where there was no restoring force and voltages required for deflection were less than 1V. A plot of the angular deflection of the rotor vs. applied voltage at various points along this process is shown in Figure 4.3.

Because of the very low voltages required for angular movement of the final device and the lack of any restoring force, these devices appeared to be "rotationally free." Using the previous FEA models an upper limit to the spring constant for this new state was

calculated. The spring constant of the device had decreased by at least four orders of magnitude to be at most 10^{-19} N·m. The rotor was now free to be rotated to any orientation in 360°. This was done by applying low level (<5 V) DC voltages to the two side stators and the conducting back gate stator using three separate DC power supplies. Figure 4.4 shows the rotor in various positions with a depiction of the rotor/nanotube cross section to illustrate its position in the SEM image. If the applied voltages were removed the rotor remained in the same position for many minutes until eventually under the influence of surface charging from the SEM electron beam the rotor would be pulled to a vertical position. We had indeed rotationally freed the outer wall of a MWCNT, creating a MWCNT motor!

As mentioned previously, we presume that these large angular deflections were exceeding the elastic limit of the MWCNT. Because the walls of the MWCNT are loosely coupled, a majority of the strain was concentrated on the outer wall of the MWCNT. When this wall was twisted past the elastic limit local damage was induced and it began to fail. With repeated strains, damage continued to occur at the points where local damage had been induced previously as these were now the weakest part of the outer wall. Eventually the entire outer wall of the MWCNT fails on each side of the rotor paddle, creating a rotationally free device. The inner shells, having been subjected to little strain, remain intact and are able to act as an axle/support for the rotor and fractured outer wall of the MWCNT.

Conclusively proving that the MWCNT motor consisted of a MWCNT acting as a rotational bearing and not an extremely loose torsional spring was not possible in this configuration. While the very low voltages required for movement, lack of any restoring force and ability to move the rotor 360° were quite suggestive of a rotational bearing, they were

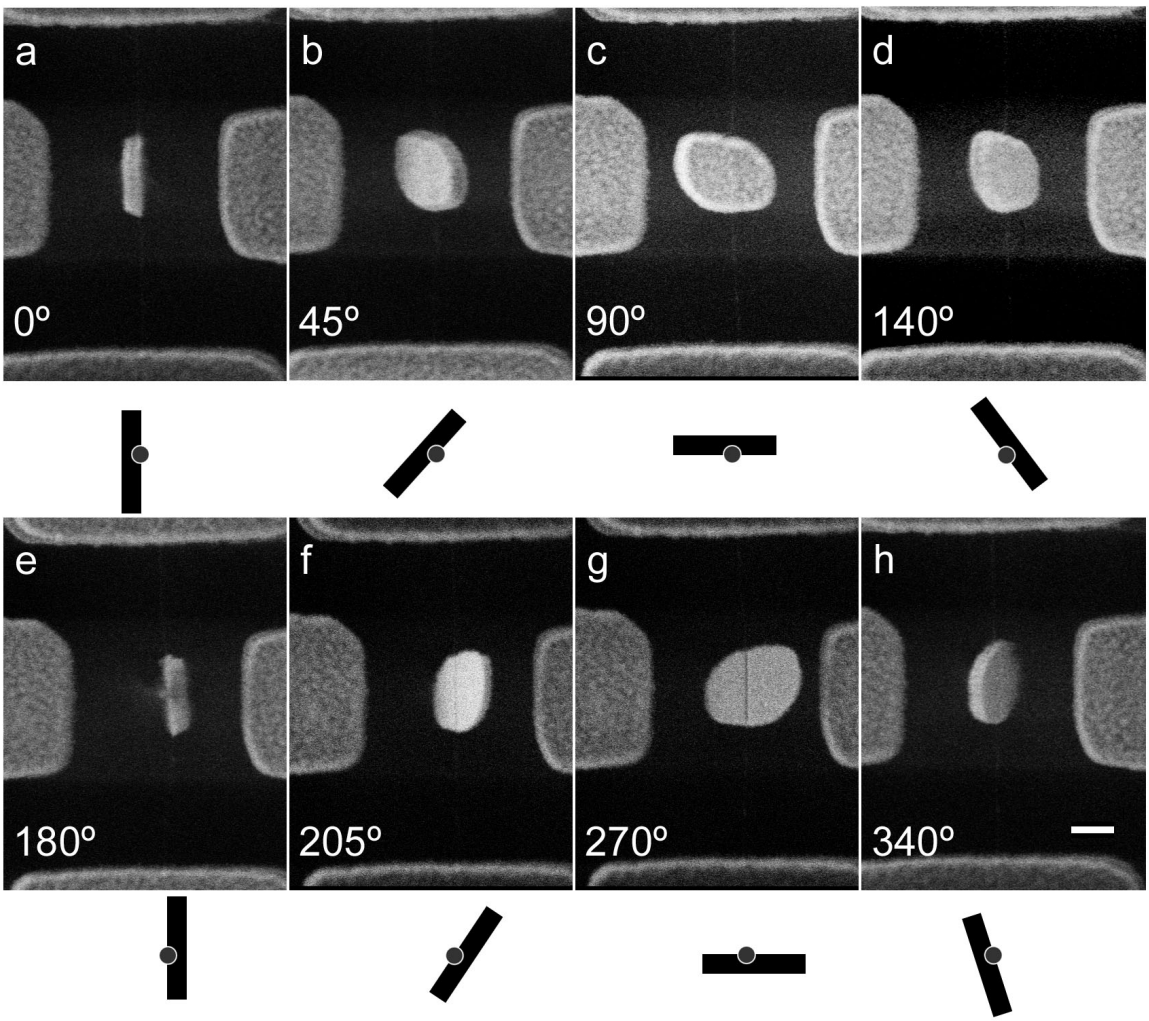

Figure 4.4: SEM images of a MWCNT motor device where the rotor plate is rotationally free and able to reach any position within 360°. Below each image is a cross sectional depiction of the rotor orientation. The nanotube (barely visible) runs vertically through each image. The scale bar is 300 nm.

not adequate for a complete proof. The inability to perform a continuous static rotation greater than 360° was the chief reason it was possible that these devices were not true rotational bearings. This limit appeared to be a result of the architecture and amount of stators in the device. Because there were only 3 stators and the MWCNT lay in the plane of the two side stators it was not possible to continuously rotate the MWCNT motor. To continuously rotate the rotor plate, appropriately positioned side stators with the MWCNT situated out of their plane or a fourth stator is needed. To introduce a fourth stator two

methods appeared viable. An *in situ* manipulator could be used to place a probe directly above the rotor to act as a fourth stator or a series of extra lithography steps could be introduced whereby an air bridge is formed to create a fourth stator. While these methods should work, at the time we had not yet purchased an SEM nor was the success rate adequate to withstand the extra lithography steps and complexity that air bridges would introduce. Thus with a fourth stator presenting a good deal of difficulty we began to attempt to lower the plane of the side stators. Thin stator electrodes were fabricated such that during the HF etch the side stators would sink with the receding surface oxide, below the horizontal plane of the MWCNT. We were not alone in this approach as Bourlon *et al* also recognized the need to have the side stators located beneath the MWCNT and used thin stator electrodes in their experiments on MWCNT motors[86]. While promising, the success rate of these devices were quite low. As the Si_3N_4 membrane project was simultaneously maturing the sunken stator architecture was abandoned in favor of an architecture where more conclusive proof of what was occurring on the atomic level would be possible.

While difficult to determine whether these original devices were truly free rotational bearings or extremely loose and resilient springs in some ways may be irrelevant. Considering that coupling any rotary motion of the paddle into another system would be a formidable task, full continuous rotational movement may provide little advantage over movement over 360°. Full 360° movement is more than adequate to perform optical switching, selective functionalization, and other possible tasks.

4.3 Dynamic Deflections

Finite frequency operation of the MWCNT motor was also possible, using a variety of suitably phased ac and dc voltage signals to the three stators and rotor plate. In one

simple operation mode, we applied out-of-phase common-frequency sinusoidal voltages to the side stators (S1 & S2), a doubled-frequency signal to the back gate stator (S3), and a dc offset to the rotor plate (R), i.e. S1=$V_\circ \sin(\omega t)$, S2=$V_\circ \sin(\omega t - \pi)$, S3=$V_\circ \sin(2\omega t + \frac{\pi}{2})$, R=-$V_\circ$. Although the resulting spatial and temporal drive forces are actually quite complex, roughly speaking this sequence allowed the rotor plate to be sequentially electrostatically attracted to the next available stator. Using this drive sequence we were reliably able to alternately flip the rotor plate between the extremal horizontal (90° and 270°) positions.

Although in principle very high frequency operation should be possible (restricted only by the stripline bandwidth of the leads and, ultimately, inertial effects of the rotor plate), our SEM image capture rate limited direct real-time observations of rotor plate oscillations to frequencies of typically several Hertz. We found that the transitions between the extremal horizontal positions could be made faster than the image video capture rate of 33 msec. Figure 4.5 shows two images of the MWCNT motor, recorded 33 msec apart, showing the rotor plate respectively in the 90° and 270° positions. We were able to rotationally drive MWCNT motors in this fashion for many thousands of cycles, with no apparent wear or degradation in performance. In this configuration, the MWCNT clearly serves as a reliable, presumably wear-free rotational degree of freedom granting NEMS element. This characterization was performed in a pressure of 10^{-6} to 10^{-5} Torr, although we anticipate reliable operation at higher pressures.

4.4 Discussion

We note that our MWCNT motor is the first true MWCNT-based NEMS device, in that it fully integrates electronic control and mechanical response. This distinguishes it from previous nanotube-based mechanical devices which require relatively large and complex

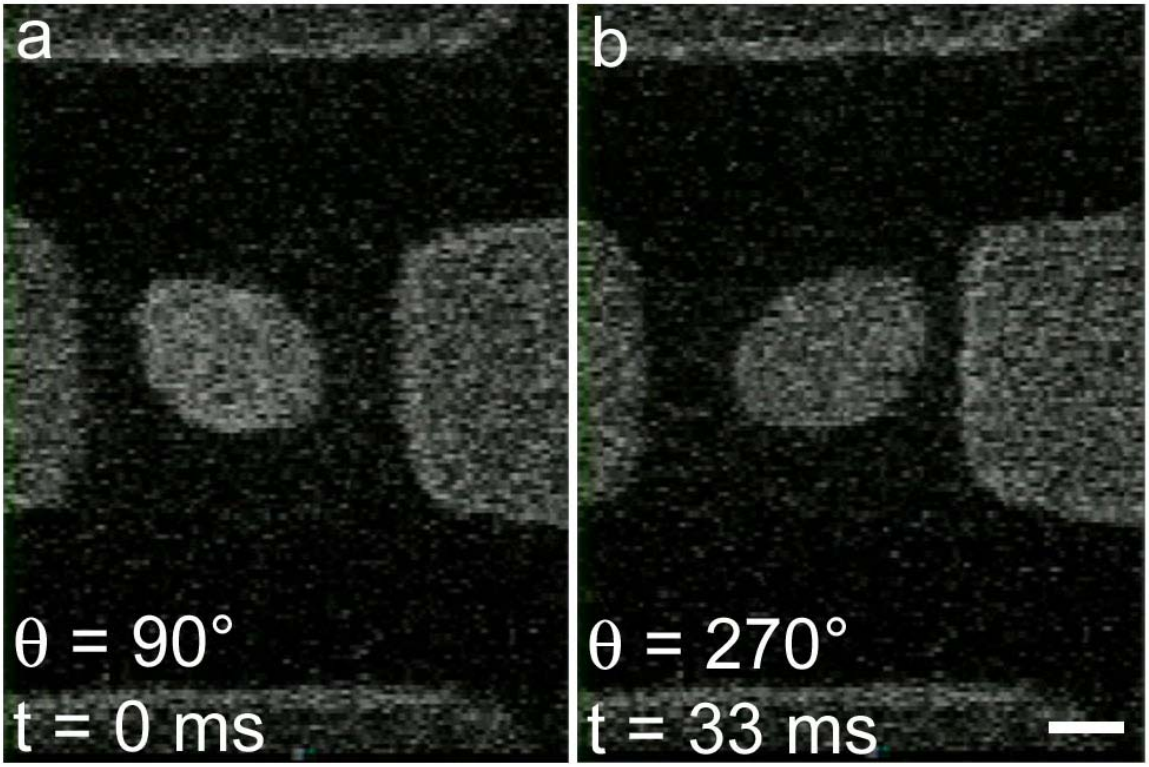

Figure 4.5: Two subsequent SEM video images of the rotor paddle taken during continuous movement. Through applying appropriately phased AC voltages to the stator electrodes the rotor paddle could be driven between the two horizontal positions shown. The time required for switching between these positions was less than the time between frames (33 msec). This movement could be sustained for thousands of cycles without any noticeable signs of wear or fatigue. The scale bar is 300 nm and the MWCNT (not visible) runs vertically through the middle of each frame.

external control systems (such as piezo-driven manipulators) to achieve operation [85, 139, 69, 70]. Unlike existing chemical and biological motors, our MWCNT motor is designed to operate over a wide range of frequency, temperature and environmental conditions, including high vacuum and harsh chemical environments.

While creation of the world's smallest motor is quite a feat there is still a great deal that our research group hopes to learn from these devices. If able to successfully perform experiments on MWCNT motors using the electron transparent substrates we will be able to investigate on the atomic scale the character of the bearings created by a variety of mechanisms. We also hope to determine whether the stress is concentrated along the outer

wall of the MWCNT or distributed to inner shells through some unforeseen coupling. The determination of how many walls are involved in torsional deformation and their exact radii will give a much more accurate determination of the shear modulus.

With the continued development of *in situ* probing techniques, more exact numbers for the torsional spring constant of these devices will be determined through the use of AFM cantilevers. Using these probes the coefficients of static and dynamic friction in these rotational devices will also be determined. An alternate method of obtaining the spring constant through resonance experiments is also being explored. The natural frequency of these devices as determined through their expected torsional spring constants and the moment of inertia of the gold rotor paddle should be 1-100 MHz. If the radius of tube, length of exposed tube, and rotor geometry are chosen appropriately, the resonance frequencies can reach the GHz regime where possible applications include mass sensing and RF signal processing. These ongoing experiments on nanotube based NEMS resonance devices are discussed in the next Chapter.

Part III

Other Nanotube NEMS structures

Chapter 5

NEMS resonators

5.1 Q in NEMS

A great deal of the excitement over NEMS has been driven by their prospective ability to replace traditional RF selection filters and to be used as ultra sensitive mass sensing devices[49]. However, for NEMS to effectively function in these applications it is essential that the resonance peak be fairly sharp. A broad peak would have too wide a bandwidth to effectively block out neighboring frequencies in RF filter applications and would limit the mass sensing resolution because of the greater uncertainty in resonance frequency. The quality factor (Q) of a resonator is determined by the amount of energy dissipated per cycle and is directly related to the width of the resonance peak, with higher Q causing sharper resonance peaks. The Q is typically defined as $Q = 2\pi\ W_\circ/\Delta\ W$ where $W_\circ$ is the total vibration energy and $\Delta\ W$ is the energy lost per cycle. As the Q decreases not only are the resonance peaks wider, limiting possible applications, but more power is needed to drive the resonator at resonance causing the prospective applications to consume more power.

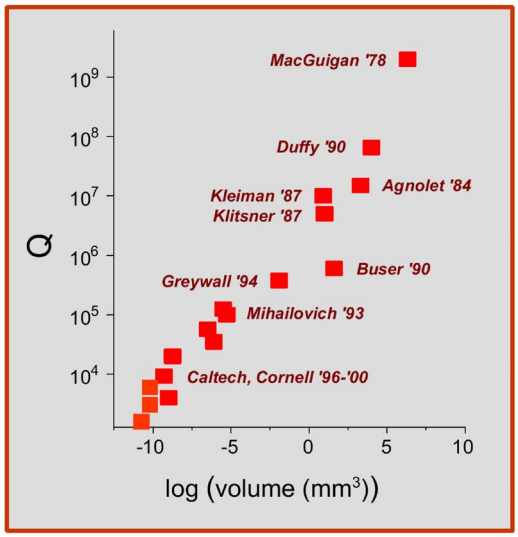

a

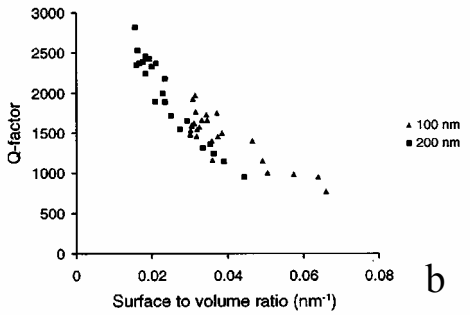

b

Diameter (nm)	log(vol(mm^3))	Surface:Volume (nm^{-1})
1.4	-14.8	2.9
10	-13.1	0.4
20	-12.5	0.2

c

Figure 5.1: (a) As the volume of experimental resonators has decreased, so has the Q. (figure from [48]) (b) The degradation of the Q was correlated directly to an increase in the surface-to-volume ratio in Si wire resonators. (figure from [141])(c) The log(vol(mm^3)) and surface-to-volume ratios are given for a 1 μm long nanotube of various diameters.

There are a number of extrinsic and intrinsic sources of damping that will lower the Q in nanomechanical systems. Some extrinsic factors which are known to cause a degradation in Q are viscous damping from air, clamping losses, and anharmonic coupling between vibration modes[140]. Because these factors are extrinsic, they can be easily overcome through performing all experiments in vacuum ($<$ 1 mTorr), careful consideration of the clamping geometry and exciting only low level oscillations in the linear regime. Intrinsic factors are of course much more difficult to overcome since they are inherent to the system. Included in intrinsic loss mechanisms are surface layer effects including adsorbates and interfaces, bulk defects and dislocations, phonon-phonon and phonon-electron interactions, and thermoelastic damping[140, 48, 50].

As resonators have scaled towards the nanoscale a general trend of decreasing Q has been observed[48]. In Figure 5.1a a plot of the Q obtained in various experiments is plotted versus the log of the resonator volume. From this dependence it appeared that

the increased surface-to-volume ratio was causing an increase in the intrinsic dissipation independent of the experimental setup. Further experiments where the geometry of single material resonators was altered and the Q determined as a function of size, temperature and pressure have confirmed that the dissipation experienced in NEMS is a surface effect directly correlated to their high surface-to-volume ratio[141, 142, 140, 143]. While it is clear that the increased surface-to-volume ratio of NEMS is the primary cause for their low values of Q, the exact damping mechanism is still unclear and is a well studied topic. The increased density of defects due to the surface layer, surface oxidation, adsorbates and surface reconstruction are a few of the causes that have been proposed.

5.2 Nanotubes as NEMS resonators

While progress in understanding the intrinsic mechanisms behind damping in nanomechanical oscillators may enable traditional NEMS materials to surpass the current limits to Q, it may be possible that the intrinsic damping is insurmountable. In hopes of further understanding and perhaps circumventing the surface dominated dissipation in traditional NEMS, alternative materials are being explored. Recent experiments on nanocrystalline diamond found that NEMS resonators, although promising, experienced dissipation markedly similar to that found in traditional materials[144].

Nanotubes present themselves as an ideal alternative material for NEMS studies. From the physical characteristics of nanotubes it is difficult to predict what the value of their Q's should be. The $\log(volume(mm^3))$ and the surface to volume ratios of nanotubes, as indicated in Figure 5.1c, suggest that if they follow the trend of traditional NEMS materials their Q's will be exceptionally low, possibly in the single digits. Additionally, if interfaces play a strong role in damping it is possible the many layers of MWCNT although

supposed to interact minimally, could act as a maximum amount of interfaces per unit volume. However, a number of factors suggest that nanotubes could be excellent NEMS materials and may even be immune to the surface damping effects seen in other NEMS. The ratio of $\sqrt{E/\rho}$ in nanotubes should be extremely large, giving very high natural resonance frequencies. The atomic perfection of nanotubes suggest that it should be possible to create a "single crystal" resonator without any defects, which have been suggested to be the key cause of dissipation currently seen in NEMS. Because SWCNT consist of a single layer, there are no surface relaxation effects or interfaces which may be the sources of the surface dependent dissipation. With nanotubes potential to either act as high Q, high frequency oscillators or to help elucidate the intrinsic damping mechanisms present in NEMS, many research groups have studied various nanotube oscillators. Our groups ongoing efforts in nanotube resonators, framed by the concurrent work of other research groups, is discussed in the next sections.

5.2.1 Singly Clamped Beams

When raw nanotube fuzz is imaged in a TEM it can be seen to consist of many singly clamped nanotubes. These singly clamped nanotubes oscillate due to thermal vibrations. Using the temperature dependence of the oscillation amplitude the elastic modulus of nanotubes can be determined[145, 146]. Through the addition of a manipulable counterelectrode to a TEM stage, singly clamped nanotubes were driven to resonance using an applied AC electric field by the DeHeer research group[147]. Various harmonics were excited to confirm this effect. The elastic modulus of the nanotubes were determined using the observed diameters and resonance frequencies. In these experiments it was found that the elastic modulus and Q were highly dependant upon nanotube diameter with the high-

est moduli (1.2 TPa) and Q ($\sim$500) being observed for small diameter nanotubes. Larger diameter nanotubes were found to have much lower values which was attributed to wavelike distortions along the MWCNT walls when bent. This experimental method was also used by the Bando research group to determine the average elastic modulus and Q of BNNT[148]. The average elastic modulus determined was $\sim$700 GPa with Q on the order of 700. Unlike the original MWCNT experiments no strong correlation between nanotube diameter and elastic modulus or Q was seen. The low Q obtained in both of these systems may also be due to interlayer coupling and clamping losses.

5.2.2 Doubly Clamped Beams

With the use of advanced lithography and manipulation techniques it is possible to construct doubly clamped nanotube resonators. These devices have the advantage that they are free standing devices that could be directly incorporated into a mass detector, rf filter, or quantum resonator. Previous detection techniques that were used for NEMS resonators such as optical interferometry and magnetomotive detection, did not lend themselves well to nanotube devices so alternative methods were explored. The first doubly clamped resonator in which a SWCNT rope was driven to resonance was done by Reulet *et al*[149]. An external antenna was used to drive the nanotube rope at resonance and the resonance peaks were detected through the high temperature sensitivity of resistance in a SWCNT rope which has become superconducting through the proximity effect. Recently the contacts to a coiled nanotube have shown a piezoresistive response as the free standing part of the coil is driven into resonance through an electric field applied from an SPM probe[150]. The most promising doubly clamped SWCNT resonator was demonstrated recently by Sazonova *et al* which consists of a self sensing, locally driven, room temperature resonator[88]. In this

experiment a suspended semiconducting SWCNT is driven into resonance using AC voltages applied to the conducting back gate. As the nanotube oscillates, the changing position leads to a change in capacitance between the nanotube and the gate which greatly affects the number of charge carriers on the semiconducting tube and therefore its conductance. These conductance changes could be sensed by using the nanotube as a mixer. The resonance frequency of this SWCNT resonator could also be tuned by applying a DC bias to the gate voltage causing the nanotube to be attracted to the gate which would increase the tension and drive up the resonance frequency. These results were quite promising in that a room temperature nanotube oscillator was fabricated which did not require external probes or microscopes to drive or sense its motion. However the highest values for Q that were obtained, 200, were quite low.

TEM was a powerful tool in the previous singly clamped nanotube experiments, allowing the nanotube diameter, defect density and damping mechanisms to be directly examined. Because of techniques developed in our research group, we are in a unique position to construct doubly clamped oscillators which can be examined *in situ* with TEM. There are actually two avenues through which doubly clamped electron transparent devices are being constructed. Kenny Jensen and Çağlar Girit have become quite adept at using the *in situ* Nanofactory manipulation stage to contact both ends of MWCNT in the TEM. Then by applying an AC current directly to the nanotube the resonance frequencies can be excited presumably through the Lorentz force created by the magnetic field of the TEM lens. Additionally they have been able to perform resonance experiments on doubly clamped telescoping MWCNT which should allow better determination of the interwall damping, tension, and other important characteristics of MWCNT. The other method that is being pursued is to fabricate a freestanding doubly clamped SWCNT oscillator on the electron

transparent Si_3N_4 membranes. These devices will have a number of distinct advantages over the devices used previously by Sazonova *et al* in that they will allow the entire tube to be examined for HF damage, defects, multiple walls and small ropes–all of which may have contributed to the low Q values. The use of van der Waals interaction as a clamping mechanism will also be avoided as this may have also been a factor in the low Q values obtained. By applying large currents to the nanotubes it may be possible to anneal out any defects and to drive off surface adsorbates through local heating. The electron transparency of these devices will allow the resonances of these devices to be confirmed through both the techniques used by Sazanova *et al* and direct imaging of motion within the TEM.

5.2.3 Torsional Resonators

Prior to fully compromising the outer walls of the MWCNT in the motor devices these devices were actually equivalent to previous NEMS torsional oscillators[151]. With a nanotube acting as a torsional spring the resonance frequencies of these devices would be 1-100 MHz depending upon the nanotube diameter and shear modulus. The resonance frequency $\omega = \sqrt{\frac{\kappa}{I}}$, from equation 4.1 and the moment of inertia of the rotor paddle $\omega \propto \sqrt{\frac{(r_{out}^4 - r_{in}^4)/l}{\rho w h L^3}}$. By altering the length and diameter of the MWCNT and the size of the rotor paddle it might be possible to push the resonance of MWCNT torsional resonators into the GHz range. Determining the Q of these devices will provide insight into the effectiveness of MWCNT as NEMS resonators and the presence of inherent damping mechanisms such as interlayer coupling.

As the primary focus of the creation of these devices was to demonstrate the rotational bearing nature of a MWCNT, little time was spent in the beginning on exploring their torsional resonances. However, torsional resonance was often observed in the SEM in

devices where the MWCNT had been partially compromised. These partially compromised MWCNT were seen to oscillate about their near vertical rest positions. The resonances were visible as stripes in the SEM image as the rotor paddle swung in and out of the electron beam as shown in Figure 5.2. Presumably the charging influence of the electron beam rastering across the SiO_2 surface and the MWCNT rotor paddle was the driving force of the observed resonances.

Because the MWCNT was partially compromised, the observed resonances were at frequencies of a few hundred kHz rather than several MHz. By performing a Fourier transform of the paddle area the period of oscillation in pixels can be extracted. If the beam dwell time per pixel is derived from the image width and the linescan rate, this oscillation period can easily be converted to seconds. The linescan rate was doubled thereby causing the pixel period to halve, as would be expected if the extra time required for overscan and raster return was small compared to the total linescan time. Over time the resonance frequencies of these devices would decrease as the MWCNT became increasingly compromised. The calculated torsional spring constants of $10^{16} - 10^{17}\ N \cdot m$ were orders of magnitude less than those obtained for intact devices. In these observations of torsional resonance there was no way to calculate the Q of these devices. It can be assumed that since the MWCNT is damaged and the resonance frequency was seen to slowly decrease that the Q will be quite low.

Ideally resonance experiments could be performed on torsional resonators in which the MWCNT had not been physically compromised. This would allow a more exact determination of the shear modulus of MWCNT and determination of the device Q. Our first attempts to perform resonance experiments on uncompromised MWCNT were to exploit the *in situ* measurement setup of the SEM. Using low level AC voltages applied to the

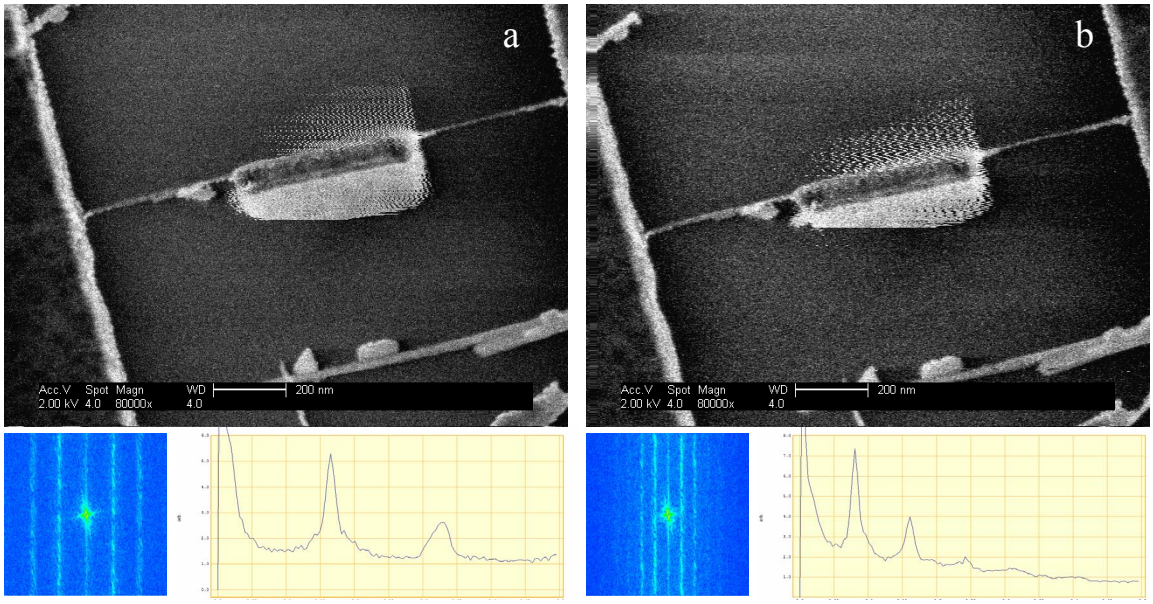

Figure 5.2: SEM images of rotor paddle resonating at 250 kHz imaged at two line scan rates of (a)0.42 ms/line and (b)0.21 ms/line. Each line consists of 645 pixels. The Fourier transform of the paddle area is shown at the lower left hand corner of each image along with the average line scan of the Fourier transform at the lower right hand corner.

conducting back gate we hoped to see movement of the rotor paddle in the SEM image when the resonance frequencies were reached. Unfortunately because of the low acceleration voltages used in SEM when low level voltages are applied it causes the electron beam to deflect. This caused image movement due to the applied AC voltages to dominate over any rotational movement of the rotor paddle. However, these frequency scans would often result in a compromised MWCNT with a vertical rotor paddle. This was presumably due to torsional resonance causing the MWCNT to rotate past its elastic limit. Even these events were difficult to discern within the oscillating image. Other approaches were also explored for sensing resonance within the SEM experimental setup. Using the *in situ* nanomanipulator a probe could be placed within close proximity of the rotor paddle. The resonance circuit was then set up so that this probe could act as a touch sensor or a capacitive antenna but a null result was obtained in both cases. Trying to use possible piezoresistive effects

in the device the resistance was also tracked as AC voltages were applied. This approach also yielded no results. Gavi Begtrup and Andras Kis continue to investigate piezoresistive effects in torsionally strained nanotubes.

Optical interferometry has been used previously to investigate the resonances of torsional NEMS oscillators[152]. We investigated the possible use of this technique through collaboration with the Bokor group or construction of our own setup either from scratch or using commercially available laser doppler vibrometers (Polytec USA). While doing this Papadakis *et al* were able to first successfully demonstrate the use of this technique to detect torsional resonances in MWCNT torsional resonators[153]. In their results they found that their devices had resonance frequencies of 1-10 MHz with Q values on the order of 100. Using the diameter and resonance frequencies of the nanotubes the shear moduli were calculated for strain of both all layers of the MWCNT and the outer layer only. There was a sharp division in the results suggesting a division in the strain distribution; with the strain likely occurring in only the outer layer of some nanotubes and in all layers for others.

While the low Q values obtained by Papadakis *et al* may be indicative of intrinsic damping in MWCNT due to interlayer coupling, defects or nanoscale surface effects, it may also have been a result of easily remedied causes. From our experiments on MWCNT on TEM membrane devices a number of effects have been witnessed which could easily result in large damping. We have seen that often MWCNT that appear to be single nanotubes in the SEM are actually ropes. The coupling between the nanotubes would then lead to very large damping and could possibly be the cause of the division in shear modulus that was seen. To suspend the MWCNT the samples were etched in HF which can damage the layers of the MWCNT. Figure 5.3a shows an image of a MWCNT post an HF etch obtained by Steve Konsek and Shaul Aloni. The large amount of defects in an HF etched nanotube can

lead to surface damping effects and possibly cross linking between layers. To eliminate the defects induced the nanotube can be annealed, restoring it to a graphitic state as shown in Figure 5.3b. One other effect that was seen in TEM experiments was the contamination of Au balls and electron beam resist along the length of the MWCNT during the fabrication process. A TEM image of this contamination is shown in Figure 5.4. The cause of this contamination is still not fully understood. Like the HF induced defects, this contamination can be removed through high temperature annealing.

In the SEM images of Papadakis *et al* the MWCNT appear to be quite nonuniform. This nonuniformity may easily be due to the above mentioned effects or other unmentioned effects. It is clear that MWCNT with nonuniform surfaces will suffer a great deal of dissipation due to the numerous imperfections. To truly demonstrate that the low Q values obtained were due to intrinsic effects and not defective MWCNT or ropes it will be useful to perform these experiments on a TEM membrane with MWCNT and SWCNT which have been annealed.

In the end, low Q values may be inherent in nanoscale systems and insurmountable in nanotubes, but there are still many factors to eliminate and understand. TEM membranes will be an essential tool in this process, allowing mechanical experiments to be performed on perfect nanotubes. These experiments will help demonstrate the true mechanical behavior of nanotubes and illuminate the intrinsic damping mechanisms. As with previous NEMS experiments, temperature dependence of Q will help enlighten the causes and energy scales of damping[142, 140, 144]. Tom Yuzvinsky is the chief member of our group responsible for carrying forward this work on nanotube NEMS.

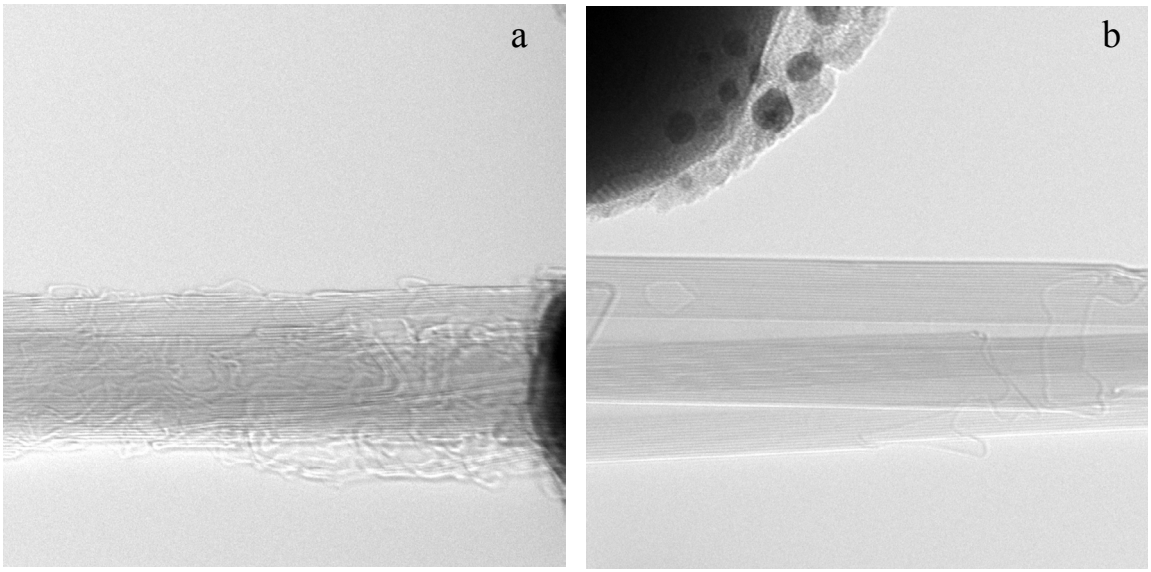

Figure 5.3: TEM images of a MWCNT that has been subjected to an HF etch (a) prior and (b) subsequent to a high current anneal. (a) After the HF etch a large amount of surface damage and defects are easily visible. (b) Once annealed the nanotube can be restored to it's original graphitic state with markedly less surface defects.

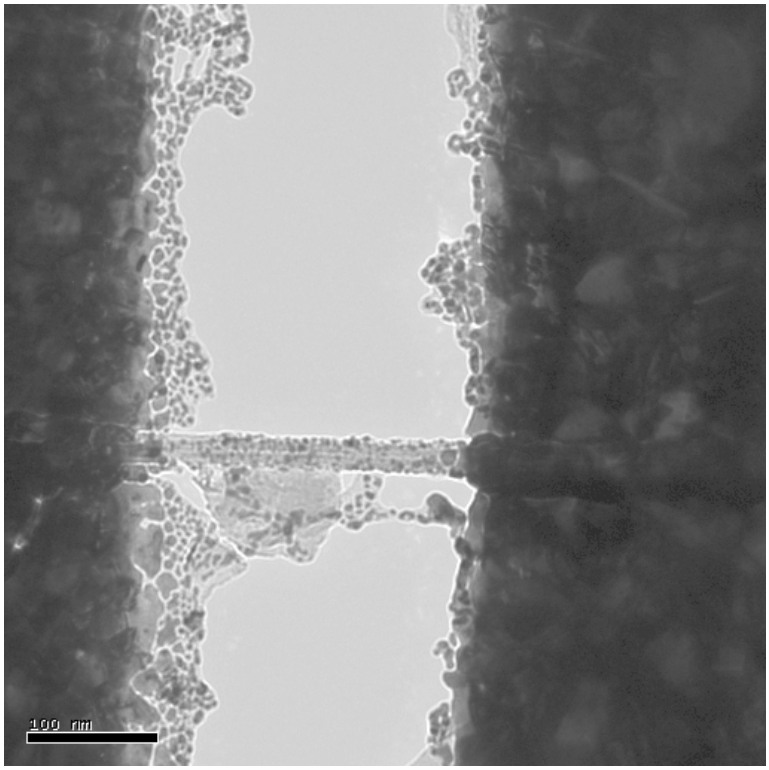

Figure 5.4: TEM image of surface contamination of Au and electron beam resist on an as fabricated MWCNT device. The scale bar is 100 nm.

5.3 Other NEMS devices

As we have previously stated, the electron transparent architecture of the Si_3N_4 membrane devices is an exciting and promising tool for correlating atomic structure with mechanical and electrical behavior of nanostructures. This architecture can be used for nanotube NEMS resonators to investigate damping mechanisms and for MWCNT motors to study the true nature of the rotational bearing. The membranes enable a host of other promising NEMS experiments which many members of our research group are currently working on, a few of which are briefly discussed here.

In Section 3.3 it was mentioned that a MWCNT which has been cut at both ends can potentially act as a GHz oscillator with the inner core oscillating back and forth within the outer shell[71]. The Si_3N_4 membranes are ideal for the creation and study of such devices. To construct a GHz oscillator two cuts will need to be made on a MWCNT which is electrically contacted at bothe ends and in the middle. The middle electrical contact will probably be a lithographically defined metal electrode, but could be a second nanotube if it is found that the metal electrode interferes with the telescoping ability of the MWCNT. Using a nanotube rather than a metal electrode may also be helpful in TEM imaging as a nanotube electrode will allow visualization of the entire nanotube. The MWCNT can be cut either by using the electron beam method outlined in Section 3.3.5 or by using a voltage pulse applied from an SPM probe as done by Park *et al*[135]. The MWCNT can also be severed by performing EDV all the way to failure of the MWCNT.

Once the MWCNT is cut the device can be loaded in the TEM and an electric field applied between the two cut ends of the nanotube to investigate whether it is possible for a MWCNT not cut by EDV to telescope, and if that telescoping can be performed by a DC applied electric field rather than direct mechanical extraction. By applying a voltage

between the two cut ends the attractive electrostatic force exerted will resemble that of a parallel plate capacitor, $F \propto \frac{V^2}{d^2}$ where d is the distance between the two cut ends. A possible difficulty with this method is that because the force is $\propto \frac{1}{d^2}$ once telescoping has begun it will be difficult to stop. This may cause the two ends to come into contact at a high potential, resulting in immediate vaporization of the entire tube. A possible method that could be used to overcome this effect would be to add electrodes to both sides of the nanotube which are parallel to each other and the nanotube as shown in Figure 5.5. Approximating this situation as parallel plates, the capacitance of these electrodes to the nanotube would then be $C = \frac{2\epsilon(l+x)h}{w}$ where l is the length of nanotube overlapping with the electrodes, x is the telescoped length, h is the device height and w is the distance between the nanotube and the electrodes. The force exerted by applying a voltage to the two electrodes will be $F = \frac{\partial U}{\partial x} = \frac{\partial \frac{1}{2} C V^2}{\partial x} = \frac{1}{2}\frac{\epsilon l h V^2}{w}$ and will be independent of the extension length. Use of side electrodes will allow the inner core of the nanotube to be extracted without the danger of vaporization on contact with the other side. The capacitive forces generated in both of these geometries should be fairly similar and in the range of pN/V^2. By applying voltages of tens of volts, enough force should be generated to extract the inner core of the MWCNT.

Once DC voltages have been attempted the next step is to apply AC voltages to determine the resonance frequency of the device. If the DC experiments were successful a good estimate of the extraction forces required and voltage thresholds will enable selection of the proper frequency range and voltage levels. However even if DC voltages proved inadequate to extract the inner core it is possible that when resonance is reached the inner core may be extracted. Resonance of the inner core will primarily be detected directly through the acquired TEM video signal. In many respects direct detection of nanotube

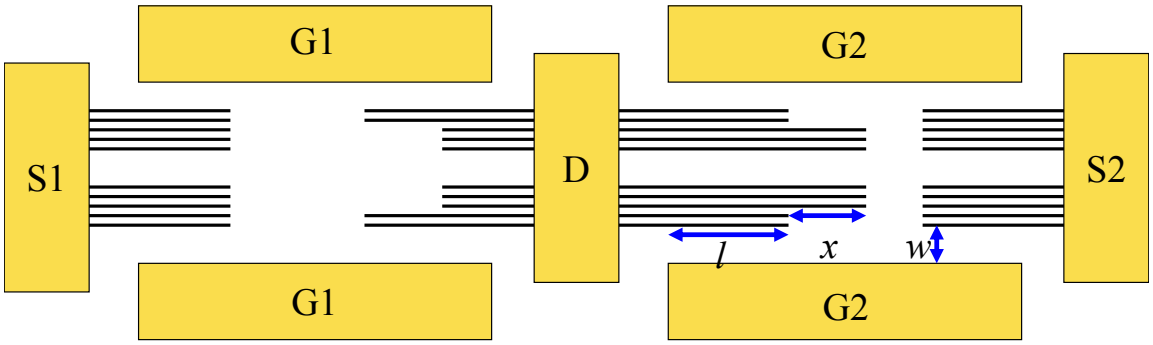

Figure 5.5: A conceptual model of a MWCNT GHz oscillator. The inner core of the MWCNT can be extracted by applying an attractive potential between the center nanotube section (D) and either the opposing nanotube sections (S1 or S2) or the capacitive electrodes (G1 or G2).

resonance via TEM imaging is an ideal method for this experiment. The architecture of the GHz oscillator does not lend itself to optical or magnetomotive detection techniques which have worked previously and the extremely small capacitances will make capacitive sensing quite difficult. If driven to large enough amplitudes it may be possible to detect resonance through current flow between the cut nanotube ends as the inner core acts as an electron shuttle. It is worth mentioning that concurrently with these experiments on GHz oscillators, other members of our research group Andras Kis, Kenny Jensen, Çağlar Girit, Willi Mickelson and Shaul Aloni are obtaining promising results using an *in situ* AFM cantilever to examine the telescoping of MWCNT in TEM. There is even the possibility that they may be able to create and examine a GHz oscillator *in situ* without the use of lithography and Si_3N_4 membranes.

An obvious corollary to the experiments on telescoping MWCNT and GHz oscillators would be to contact nanotube peapods and silo structures consisting of BN and C nanotubes filled with C_{60}. The transport characteristics of the BN silo structures could prove to be quite interesting due to the fact that the band gap of the C_{60} is less than that of the BN nanotube itself. Additionally there are a number of mechanical effects that

might be seen. It is possible that mechanical shuttling of the C_{60} molecules might be seen when external electric fields are applied. This effect would be especially likely in insulating BN. The shuttling fullerenes might even exhibit some mechanical resonances which would cause nonlinear changes in the nanotube impedance at resonant frequencies. It is also possible that if the nanotube is cut, C_{60} molecules can be directly extracted by an external electric field. Once again insulating BN is a very promising candidate for this experiment. Currently Gavi Begtrup is steadily progressing towards realizing these GHz oscillator and peapod/silo structure experiments.

Our research group is also quite interested in break junction devices on Si_3N_4 membranes. To date many interesting experiments on break junction devices have been performed where conductance plots have been suggestive of transport through a single nanostructure[154, 155, 156]. Yet there has been no way to confirm that the transport path truly involves a single nanostructure. While the main goal of these experiments is to correlate electrical transport with the quantity of nanostructures in a break junction there are a number of mechanical systems that can be studied through the use of these break junctions. One such mechanical system that would be ideal for study within break junctions are the rotaxanes. Self assembled monolayers of rotaxanes sandwiched between two electrodes have been shown to switch between two resistance states[26]. However these devices consist of thousands of rotaxanes and there is no way to conclusively demonstrate the position of the rotaxane macrocycle. By placing single rotaxane molecules or even small groups of rotaxanes on a break junction the transport behavior can be directly correlated to the orientation of the molecular shuttles. While Au is typically the material of choice in break junction devices, Gavi Begtrup has proposed using our ability to selectively cut a nanotube or severe through EDV to form a break junction for this experiment. Although a nanotube is not as

well suited as Au for making good electrical contact to a rotaxane, a cut nanotube will form a break junction which is itself electron transparent and extremely narrow in all dimensions, lending itself very well to this experiment. Conclusively demonstrating the switching of a single rotaxane molecular switch and its accompanying transport characteristics will be a major step for supramolecular chemistry and single molecule electronics.

Overall we are quite thrilled that we were able to accomplish the very difficult task of creating a MWCNT motor and developed many valuable techniques for manipulating and aligning nanotubes in the process. The prospect of being able to fully correlate atomic structure with mechanical and electrical behavior is quite exciting with many promising experiments currently underway. These experiments will lead to a greater understanding of damping mechanisms in nanotubes and the introduction of a new standard of structural characterization in nanoscale experiments.

Bibliography

[1] R. P. Feynman, Journal of Microelectromechanical Systems **1**, 60 (1992).

[2] R. Feynman, Journal of Microelectromechanical Systems **2**, 4 (1993).

[3] K. E. Petersen, Proceedings of the Ieee **70**, 420 (1982).

[4] R. T. Howe and R. S. Muller, Ieee Transactions on Electron Devices **33**, 499 (1986).

[5] Y. C. Tai and R. S. Muller, Sensors and Actuators **20**, 49 (1989).

[6] L. S. Fan, Y. C. Tai, and R. S. Muller, Sensors and Actuators **20**, 41 (1989).

[7] M. Mehregany, S. D. Senturia, J. H. Lang, and P. Nagarkar, Ieee Transactions on Electron Devices **39**, 2060 (1992).

[8] C. Mavroidis, A. Dubey, and M. Yarmush, Annual Review of Biomedical Engineering **6**, 363 (2004).

[9] J. J. Schmidt and C. D. Montemagno, Annual Review of Materials Research **34**, 315 (2004).

[10] B. S. Lee, S. C. Lee, and L. S. Holliday, Biomedical Microdevices **5**, 269 (2003).

[11] J. Howard, *Mechanics of motor proteins and the cytoskeleton*, Sinauer Associates Publishers, Sunderland, Mass., 2001.

[12] M. Schliwa, *Molecular motors*, Wiley-VCH, Weinheim Great Britain, 2003.

[13] R. Yasuda, H. Noji, K. Kinosita, and M. Yoshida, Cell **93**, 1117 (1998).

[14] M. J. Gresser, J. A. Myers, and P. D. Boyer, Journal of Biological Chemistry **257**, 12030 (1982).

[15] H. Noji, R. Yasuda, M. Yoshida, and J. Kinosita, K., Nature **386**, 299 (1997).

[16] R. Yasuda, H. Noji, M. Yoshida, J. Kinosita, K., and H. Itoh, Nature **410**, 898 (2001).

[17] R. K. Soong et al., Science **290**, 1555 (2000).

[18] R. Stracke, K. J. Bohm, J. Burgold, H. J. Schacht, and E. Unger, Nanotechnology **11**, 52 (2000).

[19] K. J. Bohm, R. Stracke, P. Muhlig, and E. Unger, Nanotechnology **12**, 238 (2001).

[20] L. Limberis, J. J. Magda, and R. J. Stewart, Nano Letters **1**, 277 (2001).

[21] L. Limberis and R. J. Stewart, Nanotechnology **11**, 47 (2000).

[22] Y. Hiratsuka, T. Tada, K. Oiwa, T. Kanayama, and T. Q. P. Uyeda, Biophysical Journal **81**, 1555 (2001).

[23] B. Yurke, A. J. Turberfield, A. P. Mills, F. C. Simmel, and J. L. Neumann, Nature **406**, 605 (2000).

[24] H. Yan, X. P. Zhang, Z. Y. Shen, and N. C. Seeman, Nature **415**, 62 (2002).

[25] V. Balzani, A. Credi, F. M. Raymo, and J. F. Stoddart, Angewandte Chemie-International Edition **39**, 3349 (2000).

[26] A. H. Flood et al., Australian Journal of Chemistry **57**, 301 (2004).

[27] T. R. Kelly, H. De Silva, and R. A. Silva, Nature **401**, 150 (1999).

[28] N. Koumura, R. W. J. Zijlstra, R. A. van Delden, N. Harada, and B. L. Feringa, Nature **401**, 152 (1999).

[29] D. A. Leigh, J. K. Y. Wong, F. Dehez, and F. Zerbetto, Nature **424**, 174 (2003).

[30] N. Koumura, E. M. Geertsema, M. B. van Gelder, A. Meetsma, and B. L. Feringa, Journal of the American Chemical Society **124**, 5037 (2002).

[31] R. A. van Delden, N. Koumura, N. Harada, and B. L. Feringa, Proceedings of the National Academy of Sciences of the United States of America **99**, 4945 (2002).

[32] J. W. Judy, Smart Materials & Structures **10**, 1115 (2001).

[33] V. K. Varadan, Nanotechnology: Mems and nems and their applications to smart systems and devices, in *SPIE-Int. Soc. Opt. Eng. Proceedings of Spie - the International Society for Optical Engineering, vol.5062, no.1, 2003, pp.20-43. USA.*

[34] B. Bhushan, *Springer handbook of nanotechnology*, Springer-Verlag, Berlin ; New York, 2004.

[35] H. Fujita, Proceedings of the Ieee **86**, 1721 (1998).

[36] G. T. A. Kovacs, *Micromachined transducers sourcebook*, WCB, Boston, Ma., 1998.

[37] M. Gad-el Hak and C. O. service), *The MEMS handbook*, CRC Press, Boca Raton, Fla., 2002.

[38] M. J. Madou, *Fundamentals of microfabrication : the science of miniaturization*, CRC Press, Boca Raton, Fla., 2nd edition, 2002.

[39] S. D. Senturia, *Microsystem design*, Kluwer Academic Publishers, Boston, 2001.

[40] N. Maluf and K. Williams, *Introduction to microelectromechanical systems engineering*, Artech House, Boston, 2nd edition, 2004.

[41] J. D. McBrayer, An overview of sandia national laboratories' mems activities, in *2002 IEEE Aerospace Conference Proceedings (Cat. No.02TH8593). IEEE. Part vol.4, 2002, pp.4-2024 vol.4. Piscataway, NJ, USA.*

[42] B. Warneke, M. Last, B. Liebowitz, and K. S. J. Pister, Computer **34**, 44 (2001).

[43] H. B. Chan, V. A. Aksyuk, R. N. Kleiman, D. J. Bishop, and F. Capasso, Science **291**, 1941 (2001).

[44] K. Schwab, E. A. Henriksen, J. M. Worlock, and M. L. Roukes, Nature **404**, 974 (2000).

[45] D. Rugar, R. Budakian, H. J. Mamin, and B. W. Chui, Nature **430**, 329 (2004).

[46] M. D. LaHaye, O. Buu, B. Camarota, and K. C. Schwab, Science **304**, 74 (2004).

[47] H. G. Craighead, Science **290**, 1532 (2000).

[48] M. L. Roukes, Nanoelectromechanical systems, in *Technical Digest. Solid-State Sensor and Actuator Workshop (TRF Cat. No.00TRF-0001). Transducers Res. Found. 2000, pp.367-76. Cleveland, OH, USA.*

[49] M. Roukes, Physics World **14**, 25 (2001).

[50] A. N. Cleland, *Foundations of nanomechanics : from solid-state theory to device applications*, Advanced texts in physics, Springer, Berlin ; New York, 2003.

[51] K. Deng, V. R. Dhuler, M. Mehregany, and E. W. Jansen, Measurement of micromotor dynamics in lubricating fluids, in *Proceedings. IEEE. Micro Electro Mechanical*

Systems. An Investigation of Micro Structures, Sensors, Actuators, Machines and Systems (Cat. No.93CH3265-6). IEEE. 1993, pp.260-4. New York, NY, USA.

[52] A. H. Epstein, Journal of Engineering for Gas Turbines & Power-Transactions of the ASME **126**, 205 (2004).

[53] U. Srinivasan et al., Lubrication of polysilicon micromechanisms with self-assembled monolayers, in *Technical Digest. Solid-State Sensor and Actuator Workshop. Transducer Res. Found. 1998, pp.156-61. Cleveland, OH, USA.*

[54] E. J. Garcia and J. J. Sniegowski, Sensors and Actuators a-Physical **48**, 203 (1995).

[55] J. J. Sniegowski and E. J. Garcia, Ieee Electron Device Letters **17**, 366 (1996).

[56] D. M. Tanner et al., The effect of frequency on the lifetime of a surface micromachined microengine driving a load, in *1998 IEEE International Reliability Physics Symposium Proceedings. 36th Annual (Cat. No.98CH36173). IEEE. 1998, pp.26-35. New York, NY, USA.*

[57] S. L. Miller et al., Routes to failure in rotating mems devices experiencing sliding friction, in *SPIE-Int. Soc. Opt. Eng. Proceedings of Spie - the International Society for Optical Engineering, vol.3224, 1997, pp.24-30. USA.*

[58] D. M. Tanner, J. A. Walraven, S. S. Mani, and S. E. Swanson, Pin-joint design effect on the reliability of a polysilicon microengine, in *2002 IEEE International Reliability Physics Symposium. Proceedings. 40th Annual (Cat. No.02CH37320). IEEE. 2002, pp.122-9. Piscataway, NJ, USA.*

[59] T. Rueckes et al., Science **289**, 94 (2000).

[60] S. Iijima, Nature **354**, 56 (1991).

[61] Z. Yao, C. L. Kane, and C. Dekker, Physical Review Letters **84**, 2941 (2000).

[62] M. S. Dresselhaus and P. Avouris, Introduction to carbon materials research, in *Carbon Nanotubes*, volume 80 of *Topics in Applied Physics*, pages 1–9, 2001.

[63] B. C. Edwards and H. E. Bennett, Space elevator feasibility test using laser power beaming, in *SPIE-Int. Soc. Opt. Eng. Proceedings of Spie - the International Society for Optical Engineering, vol.4632, 2002, pp.141-7. USA.*

[64] J. C. Charlier and J. P. Michenaud, Physical Review Letters **70**, 1858 (1993).

[65] A. N. Kolmogorov and V. H. Crespi, Physical Review Letters **85**, 4727 (2000).

[66] R. Saito, R. Matsuo, T. Kimura, G. Dresselhaus, and M. S. Dresselhaus, Chemical Physics Letters **348**, 187 (2001).

[67] Y. E. Lozovik, A. Minogin, and A. M. Popov, Physics Letters A **313**, 112 (2003).

[68] T. Vukovic, M. Damnjanovic, and I. Milosevic, Physica E-Low-Dimensional Systems & Nanostructures **16**, 259 (2003).

[69] J. Cumings and A. Zettl, Science **289**, 602 (2000).

[70] M. F. Yu, B. I. Yakobson, and R. S. Ruoff, Journal of Physical Chemistry B **104**, 8764 (2000).

[71] Q. S. Zheng and Q. Jiang, Physical Review Letters **88** (2002).

[72] Y. Zhao, C. C. Ma, G. H. Chen, and Q. Jiang, Physical Review Letters **91** (2003).

[73] J. Servantie and P. Gaspard, Physical Review Letters **91** (2003).

[74] W. L. Guo, Y. F. Guo, H. J. Gao, Q. S. Zheng, and W. Y. Zhong, Physical Review Letters **91** (2003).

[75] S. B. Legoas et al., Physical Review Letters **90** (2003).

[76] J. L. Rivera, C. McCabe, and P. T. Cummings, Nano Letters **3**, 1001 (2003).

[77] P. Tangney, S. G. Louie, and M. L. Cohen, Physical Review Letters **93**, 065503/1 (2004).

[78] S. J. Tans et al., Nature **386**, 474 (1997).

[79] S. J. Tans, A. R. M. Verschueren, and C. Dekker, Nature **393**, 49 (1998).

[80] R. Martel, T. Schmidt, H. R. Shea, T. Hertel, and P. Avouris, Applied Physics Letters **73**, 2447 (1998).

[81] A. Bachtold, P. Hadley, T. Nakanishi, and C. Dekker, Science **294**, 1317 (2001).

[82] V. Derycke, R. Martel, J. Appenzeller, and P. Avouris, Nano Letters **1**, 453 (2001).

[83] M. Bockrath et al., Nature **397**, 598 (1999).

[84] H. W. C. Postma, T. Teepen, Z. Yao, M. Grifoni, and C. Dekker, Science **293**, 76 (2001).

[85] P. A. Williams et al., Physical Review Letters **89** (2002).

[86] B. Bourlon, D. C. Glattli, C. Miko, L. Forro, and A. Bachtold, Nano Letters **4**, 709 (2004).

[87] A. Husain et al., Applied Physics Letters **83**, 1240 (2003).

[88] V. Sazonova et al., Nature **431**, 284 (2004).

[89] J. Cumings and A. Zettl, Physical Review Letters **93**, 086801/1 (2004).

[90] L. Forro, Science **289**, 560 (2000).

[91] W. Mickelson, S. Aloni, W. Q. Han, J. Cumings, and A. Zettl, Science **300**, 467 (2003).

[92] Y. Huang, X. F. Duan, Q. Q. Wei, and C. M. Lieber, Science **291**, 630 (2001).

[93] M. D. Lay, J. P. Novak, and E. S. Snow, Nano Letters **4**, 603 (2004).

[94] H. J. Xin and A. T. Woolley, Nano Letters **4**, 1481 (2004).

[95] S. R. Lustig et al., Nano Letters **3**, 1007 (2003).

[96] M. R. Diehl, S. N. Yaliraki, R. A. Beckman, M. Barahona, and J. R. Heath, Angewandte Chemie-International Edition **41**, 353 (2001).

[97] M. Burghard, G. Duesberg, G. Philipp, J. Muster, and S. Roth, Advanced Materials **10**, 584 (1998).

[98] J. Muster et al., Journal of Vacuum Science & Technology B **16**, 2796 (1998).

[99] J. Liu et al., Chemical Physics Letters **303**, 125 (1999).

[100] K. H. Choi et al., Surface Science **462**, 195 (2000).

[101] E. Valentin et al., Microelectronic Engineering **61-2**, 491 (2002).

[102] J. C. Lewenstein, T. P. Burgin, A. Ribayrol, L. A. Nagahara, and R. K. Tsui, Nano Letters **2**, 443 (2002).

[103] S. G. Rao, L. Huang, W. Setyawan, and S. H. Hong, Nature **425**, 36 (2003).

[104] J. Goldstein, *Scanning electron microscopy and X-ray microanalysis : a text for biologists, materials scientists, and geologists*, Plenum Press, New York, 2nd edition, 1992.

[105] Y. Koval, Journal of Vacuum Science & Technology B **22**, 843 (2004).

[106] S. Niyogi et al., Journal of Physical Chemistry B **107**, 8799 (2003).

[107] Y. M. Wang, W. Q. Han, and A. Zettl, New Journal of Physics **6** (2004).

[108] J. Chen and W. A. Weimer, Journal of the American Chemical Society **124**, 758 (2002).

[109] H. A. Pohl, *Dielectrophoresis : the behavior of neutral matter in nonuniform electric fields*, Cambridge University Press, Cambridge ; New York, 1978.

[110] M. P. Hughes, Electrophoresis **23**, 2569 (2002).

[111] K. Yamamoto, S. Akita, and Y. Nakayama, Japanese Journal of Applied Physics Part 2-Letters **35**, L917 (1996).

[112] K. Yamamoto, S. Akita, and Y. Nakayama, Journal of Physics D-Applied Physics **31**, L34 (1998).

[113] X. Q. Chen, T. Saito, H. Yamada, and K. Matsushige, Applied Physics Letters **78**, 3714 (2001).

[114] L. A. Nagahara, I. Amlani, J. Lewenstein, and R. K. Tsui, Applied Physics Letters **80**, 3826 (2002).

[115] R. Krupke et al., Applied Physics a-Materials Science & Processing **76**, 397 (2003).

[116] R. Krupke, F. Hennrich, H. von Lohneysen, and M. M. Kappes, Science **301**, 344 (2003).

[117] R. Krupke, F. Hennrich, M. M. Kappes, and H. V. Lohneysen, Nano Letters **4**, 1395 (2004).

[118] S. Baik, M. Usrey, L. Rotkina, and M. Strano, Journal of Physical Chemistry B **108**, 15560 (2004).

[119] H. Nishijima, S. Akita, and Y. Nakayama, Japanese Journal of Applied Physics Part 1-Regular Papers Short Notes & Review Papers **38**, 7247 (1999).

[120] J. Cumings, P. G. Collins, and A. Zettl, Nature **406**, 586 (2000).

[121] F. Stevens, L. A. Kolodny, and T. P. Beebe, Journal of Physical Chemistry B **102**, 10799 (1998).

[122] M. Perez-Mendoza, M. Domingo-Garcia, and F. J. Lopez-Garzon, Carbon **37**, 1463 (1999).

[123] J. I. Paredes, A. Martinez-Alonso, and J. M. D. Tascon, Carbon **38**, 1183 (2000).

[124] A. Cuesta, A. Martinez-Alonso, and J. M. D. Tascon, Carbon **39**, 1135 (2001).

[125] Y. J. Lee, H. H. Kim, and H. Hatori, Carbon **42**, 1053 (2004).

[126] P. C. Collins, M. S. Arnold, and P. Avouris, Science **292**, 706 (2001).

[127] B. W. Smith and D. E. Luzzi, Journal of Applied Physics **90**, 3509 (2001).

[128] H. G. Heide, Laboratory Investigation **14**, 1134 (1965).

[129] D. Joy, C. Joy, and D. Armstrong, in *Electron probe microanalysis : applications in biology and medicine*, edited by K. Zierold and H. K. Hagler, Springer series in biophysics ; v. 4, pages 127–136, Springer-Verlag, Berlin ; New York, 1989.

[130] Y. Talmon, H. T. Davis, L. E. Scriven, and E. L. Thomas, Journal of Microscopy-Oxford **117**, 321 (1979).

[131] J. Marti and M. C. Gordillo, Journal of Chemical Physics **119**, 12540 (2003).

[132] F. Banhart, T. Fuller, P. Redlich, and P. M. Ajayan, Chemical Physics Letters **269**, 349 (1997).

[133] J. Schutten, F. J. Deheer, H. R. Moustafa, A. J. Boerboom, and Kistemak.J, Journal of Chemical Physics **44**, 3924 (1966).

[134] A. Rubio, S. P. Apell, L. C. Venema, and C. Dekker, European Physical Journal B **17**, 301 (2000).

[135] J. Y. Park, Y. Yaish, M. Brink, S. Rosenblatt, and P. L. McEuen, Applied Physics Letters **80**, 4446 (2002).

[136] J. X. Li and F. Banhart, Nano Letters **4**, 1143 (2004).

[137] C. H. Kiang, W. A. Goddard, R. Beyers, and D. S. Bethune, Journal of Physical Chemistry **100**, 3749 (1996).

[138] W. C. Young, R. G. Budynas, and R. J. Roark, *Roark's Formulas for stress and strain*, McGraw-Hill, New York ; London, 7th edition, 2001.

[139] P. A. Williams et al., Applied Physics Letters **82**, 805 (2003).

[140] P. Mohanty et al., Physical Review B **66** (2002).

[141] D. W. Carr, S. Evoy, L. Sekaric, H. G. Craighead, and J. M. Parpia, Applied Physics Letters **75**, 920 (1999).

[142] K. Y. Yasumura et al., Journal of Microelectromechanical Systems **9**, 117 (2000).

[143] V. B. Braginskii, V. P. Mitrofanov, V. I. Panov, K. S. Thorne, and C. Eller, *Systems with small dissipation*, University of Chicago Press, Chicago, 1985.

[144] A. B. Hutchinson et al., Applied Physics Letters **84**, 972 (2004).

[145] M. M. J. Treacy, T. W. Ebbesen, and J. M. Gibson, Nature **381**, 678 (1996).

[146] N. G. Chopra and A. Zettl, Solid State Communications **105**, 297 (1998).

[147] P. Poncharal, Z. L. Wang, D. Ugarte, and W. A. de Heer, Science **283**, 1513 (1999).

[148] A. P. Suryavanshi, M. F. Yu, J. G. Wen, C. C. Tang, and Y. Bando, Applied Physics Letters **84**, 2527 (2004).

[149] B. Reulet et al., Physical Review Letters **85**, 2829 (2000).

[150] A. Volodin et al., Nano Letters **4**, 1775 (2004).

[151] S. Evoy et al., Journal of Applied Physics **86**, 6072 (1999).

[152] A. Olkhovets, S. Evoy, D. W. Carr, J. M. Parpia, and H. G. Craighead, Journal of Vacuum Science & Technology B **18**, 3549 (2000).

[153] S. J. Papadakis et al., Physical Review Letters **93** (2004).

[154] H. Park et al., Nature **407**, 57 (2000).

[155] J. Park et al., Nature **417**, 722 (2002).

[156] W. J. Liang, M. P. Shores, M. Bockrath, J. R. Long, and H. Park, Nature **417**, 725 (2002).

Appendix A

List of Acronyms

AFM	Atomic Force Microscope
ATP	Adenosine Triphosphate
BNNT	Boron Nitride Nanotube
BOE	Buffered Oxide Etch
CVD	Chemical Vapor Deposition
DCE	Dichloroethane
DEP	Dielectrophoresis
DNA	Deoxyribonucleic Acid
DRIE	Deep Reactive Ion Etch
EBID	Electron Beam Induced Deposition
EBL	Electron Beam Lithography
EDV	Electrically Driven Vaporization
ESD	Electrostatic Discharge
FEA	Finite Element Analysis
FESEM	Field Emission Scanning Electron Microscope

GIS	Gas Introduction System
HF	Hydrofluoric Acid
HOPG	Highly Ordered Pyrolytic Graphite
IDE	Interdigitated Electrodes
IPA	Isopropyl Alcohol
LPCVD	Low Pressure Chemical Vapor Deposition
MEMS	Microelectromechanical Systems
MIBK	Methyl Isobutyl Ketone
MWCNT	Multi-Walled Carbon Nanotube
NCEM	National Center for Electron Microscopy
NEMS	Nanoelectromechanical Systems
ODCB	Orthodichlorobenzene
PMMA	Polymethylmethacrylate
Q	Quality Factor
RIE	Reactive Ion Etch
RPM	Revolutions per Minute
RPS	Revolutions per Second
SAM	Self Assembled Monolayer
SDS	Sodium Dodecyl Sulfate
SOI	Silicon-on-Insulator
SWCNT	Single Walled Carbon Nanotube
SEM	Scanning Electron Microscope
TEM	Transmission Electron Microscope

Appendix B

Microfabrication Recipes

B.1 Si_3N_4 membranes

B.1.1 Substrates

For the fabrication masks used it is essential that the Si wafers used are:

- 100 mm in diameter
- 200 μm thick (The etch mask windows are tuned for this thickness.)
- DSP (Actually this is the only way wafers this thin come.)
- $\langle 100 \rangle$ orientation (The KOH anisotropic etch requires this.)

All other parameters are irrelevant. Of the suppliers that I have tried I most prefer International Wafer Service (www.siwafer.com). They have a good amount of surplus wafers, fast turnaround, and do not require you to order full lots (25 wafers). If you need to use an alternate supplier, Susan Kellog of the microlab staff keeps a good list of other options.

The wafers are very thin because of original TEM restrictions given by John Cumings. Because these wafers are much thinner than typical wafers care must be taken at all

times when handling them to avoid accidental breakage.

B.1.2 Oxide/Nitride Layers

1. Clean Wafers (*sink 6*)

   Use standard microlab recipe for Piranha clean, DI rinse and spin dry to clean 200 μm wafers and any 500 μm that will be used as test wafers.

2. Oxide Growth (*tystar2*)

   Use standard recipe, 2wetoxa, with time determined by growth charts. 02:20:00 yields $\sim$ 8500 Åat 1050°C. If desired include one or two test wafers for later etch tests.

3. Nitride Deposition (*tystar9*)

   Use standard recipe, 9snita, with selected nitride thickness. A deposition time of 00:02:20 yields $\sim$ 100 Å. Process monitors and previous users can give more current deposition parameters. Typically this deposition step is performed on all wafers from previous oxide growth, and a clean test wafer (HF dipped to remove native oxide). This clean test wafer can then be used to more easily determine the nitride thickness using the ellipsometer *sopra*. For thicker nitride films the photospectrometer *NanoDUV* can be helpful to verify the thickness.

B.1.3 Membranes

1. Coat (*svgcoat1,2*)

   Use standard recipe of coat=2 and bake=1. This will coat the substrate with OCG 825 (G-line) at 5000 RPM with a 60 sec bake at 90°C. As many wafers have been broken on these tracks it is important to warm up the tracks with dummy wafers and scrap thin

wafers to ensure that they are operating properly. I-line is more typically used with the *ksaligner* and can be used in lieu of G-line, but it requires a post exposure bake (i.e. an extra trip along the developer tracks). We found G-line was able to achieve adequate resolution for membrane and contact pad patterning while eliminating two extra trips along the *svgdev* tracks.

2. Expose (*ksaligner*)

   To define the etch mask use the masks labelled MEM5 or MEM6. MEM5 will yield larger windows of ~ 30 μm, while MEM6 produces smaller, more robust windows of ~ 10 μm. The exposure recipe used was Hard Contact, 100 μm alignment gap, with an exposure time of ~ 2.5 s, the exact time can be determined using dummy wafers. If the wafer alignment pins were too high they would contact the mask instead of the wafer, leading to poor exposures.

3. Develop (*svgdev*)

   Use standard recipe of develop=2 and bake=7. This will develop with OCG 934 2:1 developer, 2×30 s soak and no bake. As with *svgcoat* be sure to adequately test the tracks.

4. Hard Bake (*VWR*)

   Hard bake photoresist at 120°C for 80 minutes in a teflon cassette.

5. RIE etch (*lam2*)

   Use standard recipe SIO2ET as a template for a timed etch completely through the oxide and nitride films. Copy step 5 to step 3, and step 6 to step 4 and alter the COMPL(etion) parameter to “time”, this will allow a timed etch using 850 W of RF

power with a 3:1:4 mixture of CF_4:CHF_3:He. Use 3 dummy wafers to warm up the etcher and then check the etch rate with a test wafer. Typical etch rates are supposed to be $\sim$ 500 nm/minute but were often seen to be much lower. It is best to overetch by $\sim$ 30% to ensure that the oxide layer is fully removed. If performing reliably, detection monitors may be used to ensure complete etching.

6. Ash (*technics-c*)

   Use standard ashing recipe to completely remove photoresist, 300 mTorr O_2 at 300 W for 7 min.

7. KOH etch (*sink3*)

   Etch wafers in 80°C 2:1 (by weight) H_2O:KOH for 200 minutes. During the etch ensure that the solution is being constantly agitated and that the wafers are not tilted so as to trap etch gasses within the etch pits. Use the QDR (quick dump rinse) station to rinse wafers, then blow dry with N_2. Because the wafers now have Si_3N_4/SiO_2 membranes they are even more fragile than previously.

B.1.4 Contact Pads and Alignment Marks

Originally, contact pads were patterned prior to the KOH etch. This was necessary because previous masks etched out trenches on all 4 sides of individual membranes. These trenches allowed membrane chips with consistent dimensions to be fabricated and extracted without wafer cleavage. However the handling of these individual membrane chips for device fabrication was problematic and the trenches allowed the wafers to easily fracture. The trenches were eliminated and membranes grouped in 4×4 arrays to make the wafers more robust and device fabrication easier with larger (1 cm square) pieces. Smaller membrane

windows were also introduced to eliminate the need for CPD. The small membranes are robust enough that an air gun can be used to dry the sample. Without the trenches the wafers could now withstand the patterning of contact pads after the KOH etch. If this begins to destroy devices it would be possible to revert back to old process of patterning electrodes prior to the KOH etch. It is preferable to create contact pads after the KOH etch because scratches induced during contact pad patterning create extra etch pits.

The process for creating the contact pads is as follows:

1. Coat (*svgcoat1,2*)

   Use standard recipe of coat=2 and bake=1 to coat the opposite side of the wafers with OCG 825 (G-line) at 5000 RPM with a 60 sec bake at 90°C. Extra care must be taken with the more fragile membrane wafers to ensure that the tracks are handling the wafers well.

2. Expose (*ksaligner*)

   Use backside alignment to align contact pads mask to etched alignment marks at (12.04, 50.08) and (10.02, 50.39). Expose with hard contact, $\sim$ 2.5 s exposure and a 100 μm alignment gap.

3. Develop (*svgdev*)

   Use standard recipe of develop=2 and bake=7. This will develop with OCG 934 2:1 developer, 2×30 s soak and no bake. As stated before extra care should be taken with these delicate wafers.

4. Cr/Au Deposition(*v401* or *edwardseb3* or our Thermionics e-beam evaporator)

   A thin Cr adhesion layer followed by a thick layer of Au can be evaporated in any of the three machines listed above. Typical thicknesses were 30 Å of Cr and 1000 Å of

Au. Care must be taken in the e-beam evaporators to ensure that the photoresist is not overheated which severely affects the ability to lift off the Cr/Au film.

5. Liftoff

Soak in acetone to dissolve the photoresist. When dissolved the Cr/Au film can easily be sprayed off using a squirt bottle or syringe while the wafer remains submerged in acetone. Rinse with IPA and blow dry.

B.1.5 Devices

Once the substrates have been fabricated there are still many steps involved in creating a final device. The wafers must be cleaved into 1 cm square pieces which have a 4×4 array of membrane windows and contact pads. While using a dicing saw such as *disco* is useful for thicker substrates it was best to cleave these pieces by hand considering the fragile nature of the substrates. Taking into account the natural cleavage planes of a $\langle 100 \rangle$ wafer, a small scratch was made in the wafer edge where cleavage was to begin. A tweezer or scribe tip was then placed under this scratch and used as a fulcrum while pressure was applied equally to both sides of the scratch so that the wafer would cleave starting from the scratch and propagate along the natural cleavage planes. Once 1 cm pieces have been cleaved there are still 3-4 more processes involved in creating a final device. These are a backside etch of the oxide layer, etching holes in the nitride membrane for higher resolution, depositing the nanostructures of interest and establishing electrical contact to the nanostructures. The steps involved in these processes are as follows:

Backside Etch

1. Spincoat Shipley 1818 photoresist at 2000 RPM on all samples to be etched. This layer of photoresist will protect the nitride and nanostructures on the topside of the wafer by limiting their exposure to HF. This is especially important considering that Si_3N_4 is etched by HF.

2. Bake photoresist 60 s at 90°C

3. Repeat steps 1 & 2 to avoid HF penetration of the photoresist.

4. Cleave a 1 cm chip into 4 test samples

5. Etch test samples in 49% HF for 20, 25, 30 and 35 seconds while holding with teflon tweezers and agitating.

6. Check test samples to find proper etch time ($\sim$ 27 s). This can best be done by examining their transparency in the TEM. It is also possible to examine the transition to transparency in an SEM as the acceleration voltage is increased.

7. Etch samples in 49% HF for time determined by previous step. While etching take care to minimize the handling of the chip to avoid any possible damage to the photoresist layer.

8. Rinse in DI water.

9. Soak in acetone at 80°C for 10 min to remove resist.

10. Rinse in methanol for 1 min.

11. Gently blow dry.

Nitride Holes

1. Spincoat with e-beam resist PMGI SF7 at 2000 RPM.

2. Bake e-beam resist at 185°C for 30 s.

3. Pattern holes in PMGI using NPGS system. Automatic patterning capabilities of NPGS allow all 16 membranes in each array to be quickly patterned once alignment to the array and focus correction have been performed.

4. Develop in SAL-101 for 60 s.

5. Rinse in DI water and blow dry.

6. RIE etch in *ptherm* using SF_6, MFC=100%, 200 W for 75 s. This will overetch through most nitride layers and ensures that the holes penetrate into the oxide layer. Because it is an aggressive etch it will also create holes wider than those patterned.

7. Soak in 1165 remover at 80°C for 5 min. to remove resist.

   To thin nitride membrane further a second RIE etch can be performed in *ptherm* using SF_6, MFC=100%, 200 W for 15 s. If any photoresist remains after soaking in 1165 remover an ashing step in *ptherm* can be performed using O_2, MFC=100%, 300 W for 7 min.

Nanostructure Deposition

There are many ways in which nanostructures may be deposited on a surface. For most devices spin coating a solution at approximately 5000 RPM has been the preferred method. Depositing a few drops of solution on a surface and then rinsing them off with IPA

is used to deposit materials that are in scarce supply. Direct growth of nanotubes should also be possible and is currently being investigated by Gavi Begtrup and Andras Kis.

Electrical Contacts

Standard EBL techniques are used to contact the nanostructures. The steps in this process are as follows:

1. Map the positions of the nanostructures and alignment marks using the SEM and NPGS imaging capabilities. With simple alignment and focus correction NPGS is able to continuously image the entire 4×4 array.

2. Load images into DesignCad templates (windows scripting can be used to do this for the entire array). Align images, correct alignment marks and design the electrode configuration according to the experiment to be performed and nanostructure location.

3. Spincoat e-beam resist. A standard resist recipe used was a bilayer with the first layer consisting of MMA (8.5) MAA EL9 spun at 3000 RPM for 30 s followed by a 3 min bake at 185°C. A second layer of 950k PMMA A2 is then spun on top at 3000 RPM for 30 s followed by a 3 min bake at 185°C.

4. Pattern the entire array using NPGS. Alignment is not as precise as we would like because of distortions introduced in UHR imaging mode.

5. Develop resist in MIBK:IPA 1:3 solution for 2 min.

6. Deposit metal contact layer in our Thermionics e-beam evaporator or *NRC*. Because no adhesion layer is typically needed, pure metals such as Au, Pt, or Pd can be used in hopes of more consistent electrical contact without needing any annealing.

7. Soak in acetone to remove resist and lift off metal film not adhering to the substrate. If care is taken to avoid heating resist very little soak time is needed. For more stubborn resists prolonged soaks (24hrs), hot acetone (80°C), and sonication (for films with an adhesion layer) can be used to remove the metal film.

8. Rinse in IPA and blow dry

These processes are carried out in a variety of sequences depending upon the final resolution needed and the chemical compatibility of the nanostructures. For EDV experiments on MWCNT adequate resolution could be achieved in the TEM membranes without any nitride holes. To fabricate these devices a backside etch was performed, followed by MWCNT deposition and patterning of electrical contacts. Greater resolution in the TEM can be achieved if holes are introduced in the membrane. For these devices the holes were first created, followed by nanostructure deposition and contacting. Finally a backside etch was performed. Backside etches were attempted prior to nanostructure deposition, but it was found that surface tension effects prevented nanostructures from spanning the holes.